REPUBLIQUE ALGERIENNE DEMOCRATIQUE ET POPULAIRE
MINISTERE DE L'ENSEIGNEMENT SUPERIEUR
ET DE LA RECHRCHE SCIENTIFIQUE
Université Djilali Liabes de Sidi Bel Abbes
Faculté de Génie Electrique
Département d'Electronique

THESE EN VUE DE L'OBTENTION DU DIPLOME DE DOCTEUR EN SCIENCES

Spécialité : Electronique

Option : Traitement du Signal

Présentée par : MOHAMED ATTA WADY Sanaa

FUSION OF MULTISPECTRAL AND PANCHROMATIC IMAGES FOR SPACE APPLICATIONS

FUSION D'IMAGES MULTISPECTRALES ET PANCHROMATIQUES POUR LES APPLICATIONS SPATIALES

Soutenu devant le jury composé de :

Président *: CHIKR EL MEZOUAR Miloud*	*Professeur*	*UDL-SBA*
Directeur de thèse *: BENTOUTOU Youcef*	*Directeur de recherche*	*CDS-Oran*
Co-directeur de thèse *: BOUNOUA Abdennacer*	*Professeur*	*UDL-SBA*
Examinateur *: RAHMOUNE Abdellatif*	*Professeur*	*ESI-SBA*
Examinateur *: SOUAR Zeggai*	*Professeur*	*Univ. Saida*
Examinateur *: KAROUI Moussa Sofiane*	*Directeur de recherche*	*CTS-Arzew*
Invité *: TALEB Nasreddine*	*Professeur*	*UDL-SBA*

2021 - 2022

Dédicaces

Je dédie ce travail à mon mari, Amer, pour son support, ses conseils et sa patience durant toutes ces années.

A mes petits, Rayane, Layal, Mirna, Joumana et mon nouveau-né Rozana.

A mes parents, que dieu les garde.

A mes frères et sœurs.

A la famille Wady partout.

A toute personne qui m'a encouragé pour continuer mes études.

Sanaa

Remerciements

Je remercie dieu le tout puissant de m'avoir donné la santé et la volonté de travailler, rédiger et terminer cette thèse.

Je voudrais tout d'abord remercier mon co-encadreur, Mr. ABDENNACER BOUNOUA, pour son acceptation de m'encadrer et de m'avoir donné l'opportunité de continuer mes études.

Mes sincères remerciements et gratitude sont adressés à mon encadreur, Mr. YOUCEF BENTOUTOU, pour ses encouragements, sa patience et ses judicieux conseils qui ont contribué fortement dans la réussite de ce travail.

Je tiens à remercier Mr. AHMED BENGERMIKH pour sa précieuse contribution dans ce travail.

Je dois remercier les membres de jury, Mr. MILOUD CHIKR EL MEZOUAR, Mr. ABDELLATIF RAHMOUNE, Mr. ZEGGAI SOUAR et Mr. MOUSSA SOFIANE KAROUI d'avoir accepté à examiner ce travail.

Je remercie Mr. NASREDDINE TALEB qui m'a honoré de sa présence en jury.

Je remercie encore l'Agence Spatiale Algérienne, Deimos Imaging et DigitalGlobe pour l'acquisition et la production des images utilisées dans cette recherche.

Abstract

In remote sensing applications, state-of-the-art pansharpening methods generally improve the low spatial resolution (LSR) of multispectral (MS) images by injecting into them the spatial details extracted from the panchromatic (PAN) image with high spatial resolution (HSR). Different injection models are considered. Fusion performance is highly dependent on the precision of the modeling and the estimation of model parameters. This thesis presents an optimized pansharpening algorithm based on the combination of the well-known Intensity-Hue-Saturation (IHS) method and multiscale analysis by using the "à trous" wavelets (ATWT). In this new approach, a combination of the energy and correlation coefficients between the MS bands and the PAN image is considered to make a new approximation of the weighting coefficients in the injection model. Then, the intensity component is extracted from the upsampled MS images by IHS transformation. The weighting coefficients of the intensity component are computed by using the average energy ratio between the low-pass version of the PAN image, obtained by ATWT transformation, and the MS bands in order to obtain more detail information. This last is then injected into the MS bands to obtain a pansharpened image with high spectral and spatial information.

The experimental results of the proposed approach, compared with many classical and advanced pansharpening methods, have confirmed that it can inject more spatial information and ensure better color preservation. Therefore, it can achieve a good compromise between spectral and spatial qualities.

Résumé

Dans les applications de télédétection, les méthodes avancées de fusion améliorent généralement la faible résolution spatiale (LSR) des images multispectrales (MS) en y injectant les détails spatiaux extraits de l'image panchromatique (PAN) à haute résolution spatiale (HSR). Différents modèles d'injection sont considérés. Les performances de fusion dépendent fortement de la précision de la modélisation et de l'estimation des paramètres du modèle. Cette thèse présente un algorithme de fusion optimisé basé sur la combinaison de la méthode bien connue Intensité-Teinte-Saturation (IHS) et d'une analyse multi-échelle en utilisant les ondelettes « à trous » (ATWT). Dans cette nouvelle approche, une combinaison des coefficients d'énergie et de corrélation entre les bandes MS et l'image PAN est considérée pour donner une nouvelle approximation des coefficients de pondération dans le modèle d'injection. Ensuite, la composante d'intensité est extraite des images MS sur-échantillonnées par transformation IHS. Les coefficients de pondération de la composante d'intensité sont calculés en utilisant le rapport d'énergie moyen entre la version passe-bas de l'image PAN, obtenue par transformation ATWT, et les bandes MS afin d'obtenir des informations plus détaillées. Ces informations sont ensuite injectées dans les bandes MS pour obtenir une image fusionnée avec une haute information spectrale et spatiale.

Les résultats expérimentaux de l'approche proposée, comparés à de nombreuses méthodes de fusion classiques et avancées, ont confirmé qu'elle peut injecter plus d'informations spatiales et assurer une meilleure préservation des couleurs. Par conséquent, elle peut réaliser un bon compromis entre les qualités spectrales et spatiales.

مــلـخص

في تطبيقات الاستشعار عن بعد، تعمل طرق الاندماج الحديثة بشكل عام على تحسين الدقة المكانية المنخفضة (LSR) للصور متعددة الأطياف (MS) عن طريق حقن التفاصيل المكانية المستخرجة من الصورة الشاملة (PAN) بدقة مكانية عالية (HSR). يتم أخذ نماذج الحقن المختلفة بعين الاعتبار. يعتمد أداء الاندماج بشكل كبير على دقة النمذجة وتقدير معلمات النموذج. تقدم هذه الرسالة خوارزمية محسّنة تعتمد على مزيج من طريقة (IHS) المعروفة والتحليل متعدد النطاقات باستخدام طريقة "ATWT) à trous)". في هذا النهج الجديد ، تم اعتبار توليفة من معاملات الطاقة والارتباط بين نطاقات MS وصورة PAN لإجراء تقريب جديد لمعاملات الترجيح في نموذج الاندماج. بعد ذلك، يتم استخراج عنصر الكثافة من صور MS بواسطة تحويل IHS. يتم حساب معاملات الترجيح لمكون الكثافة باستخدام متوسط نسبة الطاقة بين إصدار التمرير المنخفض لصورة PAN ، التي تم الحصول عليها عن طريق تحويل ATWT ، ونطاقات MS للحصول على مزيد من المعلومات التفصيلية. ثم يتم حقن هذه الأخيرة في نطاقات MS للحصول على صورة مندمجة مع معلومات طيفية ومكانية عالية.

أكدت النتائج التجريبية للنهج المقترح، مقارنة بالعديد من الطرق الكلاسيكية والمتقدمة، أنه يمكن أن يضخ المزيد من المعلومات المكانية ويضمن الحفاظ على اللون بشكل أفضل. لذلك، يمكنه تحقيق حل وسط جيد بين الصفات الطيفية والمكانية.

List of contents

ABSTRACTS

ACRONYMS

LIST OF FIGURES

LIST OF TABLES

GENERAL INTRODUCTION

GI. 1. Context. 1
GI. 2. Problematic. 4
GI. 3. Objectives of the thesis. 8
GI. 4. Followed approach. 8

Chapter 1: An overview of image fusion methods

1.1. Introduction. 10
1.2. Pansharpening of multi-spectral satellite images. 10
1.3. Presentation of the problem. 11
1.4. Categories of fusion methods. 14
1.4.1. Component substitution (CS)-based methods. 15
1.4.1.1. Advantages. 17
1.4.1.2. Some (CS)-based methods. 18
1.4.1.2.1. Intensity Hue Saturation (IHS) pansharpening technique. 18
1.4.1.2.1. A) IHS transform. 18
1.4.1.2.1. B) IHS pansharpening algorithm. 21
1.4.1.2.2. Principal Component Analysis (PCA) pansharpening technique. 22
1.4.1.2.2. A) PCA transform. 23
1.4.1.2.2. B) PCA pansharpening algorithm. 24
1.4.1.2.3. Brovey Transform (BT) pansharpening technique. 25
1.4.1.2.4. Gram Schmidt (GS) pansharpening technique. 25
1.4.1.3. Examples of pansharpening of some (CS)-based methods. 25
1.4.1.4. Visual Analysis. 28
1.4.2. Multiresolution analysis (MRA)-based methods. 28
1.4.2.1. Some MRA-based methods. 31
1.4.2.1.1. Discrete Wavelet Transform (DWT) pansharpening technique. 31
1.4.2.1.1. A) DWT transform. 31
1.4. 2.1.1. B) DWT pansharpening algorithm. 33
1.4.2.1.2. “A Trous” Wavelet Transform (ATWT) pansharpening technique. 34
1.4.2.1.2. A) ATWT transform. 34
1.4. 2.1.2. B) ATWT pansharpening algorithm. 35
1.4.2.1.3. Laplacian Pyramid (LP) pansharpening technique. 35
1.4.2.1.3. A) LP transform. 35
1.4. 2.1.3. B) LP pansharpening algorithm. 36
1.4.2.1.4. Additive Wavelet Luminance (AWL) pansharpening method. 37
1.4.2.1.5. High-Pass Filter (HPF) pansharpening method. 37
1.4.2.1.6. Smoothing Filter-Based Intensity Modulation (SFIM). 37

1.4.2.2. Examples of pansharpening of some (MRA)-based methods. 38
1.4.2.3. Visual Analysis. 41
1.4.3. Variational optimization (VO)-based methods. 41
1.4.3.1. Some VO-based methods. 44
1.4.3.1.1. P+XS pansharpening method. 44
1.4.3.2. Examples of P+XS pansharpening method. 44
1.4.3.3. Visual Analysis. 45
1.5. Conclusion. 45

Chapter 2: Performance evaluation and comparative study of some fusion methods
2.1. Introduction. 47
2.2. Qualitative and quantitative evaluation. 47
2.2.1. Quantitative evaluation with reference image. 48
2.2.2. Quantitative evaluation without reference image. 50
2.3. Experimental study. 51
2.4. Discussions and conclusions. 53

Chapter 3: Pansharpening with some recent methods
3.1. Introduction. 55
3.2. Some recent fusion methods. 55
3.2.1. Generalized IHS (GIHS) pansharpening method. 55
3.2.2. Improved Adaptive IHS (IAIHS) pansharpening method. 55
3.2.3. Additive Wavelet Luminance Proportional (AWLP) pansharpening method. 56
3.2.4. Generalised Laplacian Pyramid with Modulation Transfer Function (MTF-GLP) pansharpening method. 56
3.2.5. Band-Dependent Spatial Detail (BDSD) pansharpening method. 57
3.2.6. Partial Replacement Adaptive CS (PRACS) pansharpening method. 57
3.2.7. Indusion pansharpening method. 58
3.2.8. Optimal Filter (OF) pansharpening method. 58
3.3. Performance evaluation. 59
3.4. Visual analysis. 62
3.5. Quantitative analysis. 62
3.6. Conclusion. 65

Chapter 4: Proposed fusion method
4.1. Introduction. 67
4.2. Proposal of a fusion algorithm based on IHS and ATWT. 67
4.3. Experimental results. 71
4.3.1. Experimental results of the proposed approach. 72
4.3.2. Discussions. 74
4.3.3. Comparison with some state-of-the-art fusion methods. 77
4.3.4. Discussions. 85
4.4. Conclusion. 86

GENERAL CONCLUSION 87

REFERENCES

Acronyms

1D : one Dimensional.

2D : two Dimensional.

ADMM : Alternating Direction Method of Multipliers.

ARSIS : Amélioration de la Résolution Spatiale par Injection de Structures.

ATWT : “A Trous” Wavelet Transform.

AWL : Additive Wavelet Luminance.

AWLP : Additive Wavelet Luminance Proportional.

BDSD : Band Dependent Spatial Detail.

BT : Brovey Transform.

CBD : Context-Based Decision.

CC : Correlation Coefficient.

CORR : Correlation.

CS : Component Substitution.

DWT : Discrete Wavelet Transform.

ERGAS : Relative Dimensionless Global Error in Synthesis.

FIHS : Fast IHS.

GIHS : Generalized IHS.

GLP : Generalized Laplacian Pyramid.

GS : Gram Schmidt.

GSA : Adaptive Gram Schmidt.

HLS : Hue Luminance Saturation.

HPF : High Pass Filter.

HPM : High Pass Modulation.

HSV : Hue Saturation Value.

IAIHS : Improved Adaptive IHS**.**

IEEE : Institute of Electrical and Electronics Engineers.

IHS : Intensity Hue Saturation transform.

LP : Laplacian Pyramid.

MAP : Maximum Posterior Theory.

MBO : Model-Based Optimization.

MTF-GLP : Generalised Laplacian Pyramid with Modulation Transfer Function.

MMSE : Minimum Mean Square Error.

MRA : Multi-Resolution Analysis.

MS : Multi-Spectral image.

MTF : Modulation Transfer Function.

NIR : Near Infra-Red.

OF : Optimal Filter.

PAN : PANchromatic image.

PCA : Principal Component Analysis.

PRACS : Partial Replacement Adaptive Component Substitution.

PSF : Point Spreading Function.

QNR : Quality with No Reference.

RASE : Relative Average Spectral Error.

RGB : Red, Green and Blue space.

RMSE : Root Mean Squared Error.

RSC : Relative Spectral Contribution.

SAM : Spectral Angle Mapper.

SCC : Spatial Correlation Coefficient.

SDM : Spectral Distortion Minimizing.

SFIM : Smoothing Filter-Based Intensity Modulation.

SID : Spectral Information Divergence.

SR : Sparse Reconstruction.

SSIM : Structural Similarity index.

TV : Total Variation.

UDWT : Undecimated Wavelet Transformation.

UIQI : Universal Image Quality Index.

VO : Variational Optimization.

List of figures

Figure GI.1. A scene with different spatial resolutions: from left to right 1Km, 100m, 10m, 1m and 1cm. 1
Figure GI.2. An example of real sizes PAN and MS satellite images. 2
Figure GI.3. An example of upsampled images obtained from different interpolation filters. 3
Figure GI.4. An example of fusion process. 3
Figure 1.1. Ideal normalized spectral responses in terms of wavelength. 12
Figure 1.2. Responses of the different spectral bands as a function of the wavelength in micrometers (Ikonos satellite). Black, brown, red, green and blue curves, respectively, correspond to PAN, NIR, red, green and blue modalities. 12
Figure 1.3. Flowchart of the CS-based pansharpening methods. 17
(a) The traditional scheme of the CS-based methods. 16
(b) The new understanding based on the general formalization of the CS-based methods. 17
Figure 1.4. Smith's HSV color model. 18
Figure 1.5. RGB to HSV transformation. 19
Figure 1.6. An example of transformation from RGB space to IHS space. 20
Figure 1.7. Another example of transformation from RGB space to IHS space. 21
Figure 1.8. Scheme of IHS image fusion. 22
Figure 1.9. Scheme of PCA image fusion. 24
Figure 1.10. Pansharpening urban scene. a) PAN image. b) Real size MS image. c) IHS fused image. d) PCA fused image. e) BT fused image. f) GS fused image. 26
Figure 1.11. Pansharpening a vegetation scene. a) PAN image. b) Real size MS image. c) IHS fused image. d) PCA fused image. e) BT fused image. f) GS fused image. 27
Figure 1.12. Flowchart of the MRA-based pansharpening methods. 30
(a) The traditional scheme of the MRA-based pansharpening methods. 29
(b) The new understanding scheme based on the general formalization of the MRA -based pansharpening methods. 30
Figure 1.13. One decomposition level of 2D image. 32
Figure 1.14. One reconstruction level of 2D image. 33
Figure 1.15. Scheme of the Wavelet image fusion. 34
Figure 1.16. Example of an image pyramid with 5 levels. 36

Figure 1.17. Pansharpening an urban scene. a) DWT fused image. b) ATWT fused image. c) LP fused image. d) HPF fused image. e) SFIM fused image. f) AWL fused image. 39
Figure 1.18. Pansharpening a vegetation scene. a) DWT fused image. b) ATWT fused image. c) LP fused image. d) HPF fused image. e) SFIM fused image. f) AWL fused image. 40
Figure 1.19. Flowchart of the VO-based pansharpening methods. 42
Figure 1.20. Pansharpening urban and vegetation scenes, respectively.
a) P+XS fused image. b) P+XS fused image. 45
Figure 3.1. Pansharpening an urban scene. a) GIHS fused image. b) AIHS fused image. c) AWLP fused image. d) MTF-GLP fused image. e) BDSD fused image. f) PRACS fused image. g) Indusion fused image. h) OF fused image. 60
Figure 3.2. Pansharpening a vegetation scene. a) GIHS fused image. b) AIHS fused image. c) AWLP fused image. d) MTF-GLP fused image. e) BDSD fused image. f) PRACS fused image. g) Indusion fused image. h) OF fused image. 61
Figure 4.1. Flowchart of the proposed algorithm. 67
Figure 4.2. Deimos-2 image (image 1). (a) PAN image. (b) Up-sampled MS image. 71
Figure 4.3. Deimos-2 image (image 2). (a) PAN image. (b) Up-sampled MS image. 72
Figure 4.4. Deimos-2 image (image 3). (a) PAN image. (b) Up-sampled MS image. 72
Figure 4.5. Fused images by applying the proposed approach (image 1).
(a)~(c) Pansharpened images by using 1~3 decomposition levels of the ATWT, respectively. 73
Figure 4.6. Fused images by applying the proposed approach (image 2).
(a)~(c) Pansharpened images by using 1~3 decomposition levels of the ATWT, respectively. 74
Figure 4.7. Fused images by applying the proposed approach (image 3).
(a)~(c) Pansharpened images by using 1~3 decomposition levels of the ATWT, respectively. 74
Figure 4.8. Fusion results of the first Deimos-2 image for different methods. 78
Figure 4.9. Fusion results of the second Deimos-2 image for different methods. 79
Figure 4.10. Fusion results of the third Deimos-2 image for different methods. 80
Figure 4.11. Zoom of fusion results of the first Deimos-2 image for different methods. 81
Figure 4.12. Zoom of fusion results of the second Deimos-2 image for different methods. 82
Figure 4.13. Zoom of fusion results of the third Deimos-2 image for different methods. 83

List of tables

Table GI. Examples of Earth observation systems offering various images to different spatial resolutions. 6

Table 2.1. Performance evaluation metrics when reference image is available. 50

Table 2.2. Performance evaluation metrics when reference image is not available. 50

Table 2.3. Four-band correlation between reference and merged images for different methods. 51

Table 2.4. Quality metrics, when reference image is available, for different pansharpening methods. 52

Table 2.5. Quality metrics, when reference image is not available, for different pansharpening methods. 53

Table 3.1. Four-band correlation between reference and merged images for different methods. 63

Table 3.2. Quality metrics, when reference image is available, for different pansharpening methods. 63

Table 3.3. Quality metrics, when reference image is not available, for different pansharpening methods. 64

Table 3.4. Pansharpening methods in the experiments. 66

Table 4.1. Weighting coefficients of the 4-bands MS image, their sum and ratio average energy for different decomposition levels. 73

Table 4.2. 4-bands correlation between MS and fused images. 73

Table 4.3. Spectral quality assessment, with reference image, of different decomposition levels of the proposed method for different datasets. 75

Table 4.4. Spectral quality assessment, without reference image, of different decomposition levels of the proposed method for different datasets. 76

Table 4.5. Quality metrics with no reference data for different pansharpening methods using different satellite images (mean values). 84

Table 4.6. Quality metrics with reference data for different pansharpening methods using different satellite images (mean values). 84

Table 4.7. Calculation time for different methods. 86

GENERAL INTRODUCTION

GI.1. Context.

GI.2. Problematic.

GI.3. Objectives of the thesis.

GI. 4. Followed approach.

GI.1. Context

It is interesting to visualize remotely sensed images with high spatial and spectral resolutions for better land classification, map updating, soil analysis, feature extraction, etc...

Earth observation satellites provide, generally, two different types of images of a scene; a panchromatic (PAN) image (grayscale) with high spatial and low spectral resolutions and a multispectral (MS) image (color) with high spectral and low spatial resolutions.

The spatial resolution of an image is the smallest distance between two adjacent objects that the sensor can identify. Or, it's the smallest area the satellite can detect on the ground. For example, a resolution of 30 meters detects an area on the ground of 30m x 30m. Hence, a high resolution implies a reduction in the surface area. The following figure represents an example with different spatial resolutions.

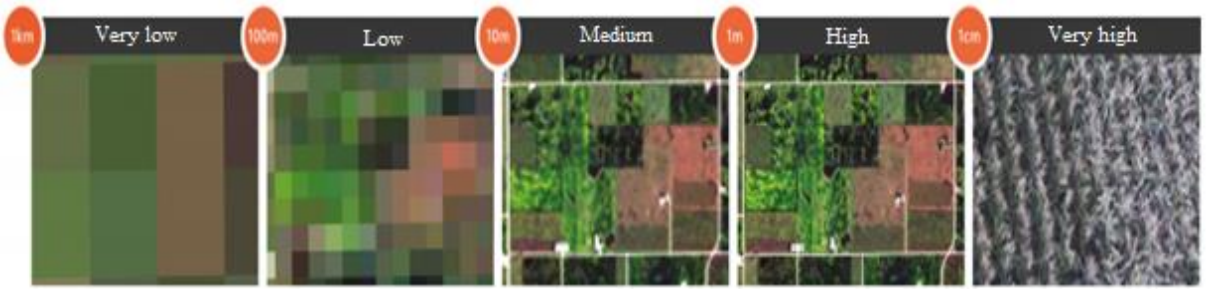

Figure GI.1. A scene with different spatial resolutions: from left to right 1Km, 100m, 10m, 1m and 1cm[1].

The spectral resolution is the separating power of a spectrograph. The spectral resolution of an image is higher, the wavelength interval is narrower.

To compose the low spatial resolution of the MS image, MS must be up-sampled (interpolated) to the same spatial resolution as the PAN image. For example, a PAN image of spatial resolution N x M and MS image of resolution N/2 x M/2 (ratio of 4), the MS image must be interpolated by 2 on the rows and 2 on the columns to have the resolution N x M. The following figure shows an example of PAN (1024x1024 pixels) and MS (256x256 pixels) images of actual sizes (ratio of 4). Figure GI.3 shows an example of an image resampled by different interpolation filters.

[1]https://www.// Geosys.com

PAN image

MS image

Figure GI.2. An example of real sizes PAN and MS satellite images[2].

[2]Matlab images

Original image

Nearest neighbor filter Bilinear filter Bicubic filter

Figure GI.3. An example of upsampled images obtained from different interpolation filters[2].

Due to technological limitations of the satellite sensors, it is very difficult to acquire a high spatial resolution MS image directly. As a post-processing method by fusing the information of the PAN and MS images, it can be employed to produce a new high spatial resolution MS image (see Figure GI.4).

PAN image Resampled MS image Fused image

Figure GI.4. An example of fusion process[3].

[3]https://www.grss-ieee.org

During the few last decades, various fusion methods have been proposed to result the problem of remote sensing image fusion [130]**.** Wald [131] defines image fusion as “a formal framework in which means and tools are expressed for the combination of data coming from different sources whose aim is to obtain better quality information, although the exact definition of "best quality" depends on the application ". According to Piella [132], fusion is "the combination of relevant information in order to synthesize a more informative and more visually perceptual image more suitable for computer processing", where the "relevance" of the information also depends on the task of application [5].

GI.2. Problematic

One of the key elements for the Earth observation and the knowledge of our environment are formed by space systems (satellites). These satellites carry various active (radar) or passive sensors on board. The sensors of interest to us are passive sensors whose bandwidth is located in the visible and infrared. They can have very different characteristics. The images delivered by these sensors allow the distinction of geometric structures according to the spatial resolution which will be considered here as equal to the sampling step corresponding to the size of the pixel. Some sensors are capable of integrating the radiative energy incident at the input of the sensor over a wide wavelength band, and therefore offer little spectral information, but at the same time offer high spatial resolution. Typically, this type of image is a grayscale image and it is called a "panchromatic image", noted as PAN below. On the contrary, other sensors on board these same satellites work on much narrower bands of the spectrum; these are a color images and therefore multispectral, denoted MS, below. Their spectral resolution is much higher, but this comes at the cost of low spatial resolution.

For many applications, the advantage of manipulating multispectral images with very high spatial resolution has already been demonstrated, for example for classification [133], [134] and [135], road mapping [136], the study of the development of urban areas [137] and [138], archaeological prospecting [139] or even in the medical field for diagnostic aid [140]. It is of course possible to distinguish large areas in an MS or PAN images as long as they have very distinct characteristics, such as the surface of the ocean in relation to the coastal zone, or a farm in relation to a region very urbanized. On the other hand, it becomes much more difficult to distinguish very heterogeneous vegetation or mineral spaces, without considering their spectral properties. The "color" information helps to distinguish different regions of the image with shades previously invisible in the initial grayscale PAN image.

Therefore, if we can use these spectral contents while taking advantage of better spatial resolution, the identification of objects in a scene will be enriched and more precise [141].

For this reason, manufacturers have not directly built sensors capable of delivering images at high spatial and spectral resolutions. These concepts are contradictory from a technical point of view because the wider the spectral acquisition bands of a sensor, the greater the luminous flux incident on a pixel of the image. The opening of the entrance pupil can then be reduced, the size of the pixels is smaller and therefore the image has better spatial resolution. On the other hand, a much narrower band of the spectrum limits the number of photons absorbed by the sensor, generally CCD (Charged-Coupled Device) and therefore the energy incident on each cell. The integration time must therefore be greater than before in order to be able to deliver a similar signal-to-noise ratio and a similar dynamic. As the spatial vector moves, this increase in integration time results in an increase in pixel size, explaining the lower spatial resolution.

To reduce this integration time, the solution is to increase the sensitivity of the detectors. But a financial limitation arises because of the expensive cost of building the more sensitive sensors. Besides the budgetary limitation, other constraints are imposed by the satellite platform in terms of space, weight, power, electromagnetic radiation, but also mission objectives (orbit), rocket for launch, etc. Assuming that the sensors are able to deliver MS images of spatial resolution reaching that of the PAN, two other problems will arise; the storage capacity on the platform and the bandwidth of the transmission channel are limited. Take the example of the Ikonos or Quickbird satellite: these satellites have four MS bands. If the spatial resolution of these images were increased by a factor of 4 to match that of the PAN, their size would be multiplied by 16, or 16 times more data to store and transmit to the ground.

Therefore, for the same geographical area, the user is in possession of a set of images; some of which benefit from good spatial resolution, while others provide good spectral resolution. Table GI summarizes various information concerning the imagery of the most commonly used satellites in the environment and in mapping; SPOT4, SPOT5, Ikonos, Quickbird, Demos 2 and Alsat-2.

	Modality MS				Modality PAN	
Satellite	Name of the band	Color	Spectral band (µm)	Ground resolution (m)	Spectral band (µm)	Ground resolution (m)
SPOT 4[4]	B1	Green	0,50-0,69	20	0,61-0,68	10
	B2	Yellow	0,61-0,68	10		
	B3	NIR	0,78-0,89	20		
	B4	MIR	1,58-1,75	20		
SPOT 5[5]	B1	Green	0,50-0,59	10	0,48-0,71	2,5 or 5
	B2	Yellow	0,61-0,68	10		
	B3	NIR	0,78-0,89	10		
	B4	MIR	1,58-1,75	10		
Ikonos[6]	B1	Blue	0,45-0,53	4	0,45-0,90	1
	B2	Green	0,52-0,61	4		
	B3	Red	0,64-0,72	4		
	B4	NIR	0,77-0,88	4		
Quickbird[7]	B1	Blue	0,45-0,52	2,8	0,45-0,90	0,7
	B2	Green	0,52-0,60	2,8		
	B3	Red	0,63-0,69	2,8		
	B4	NIR	0,76-0,90	2,8		
Deimos 2[8]	B1	Blue	0,42-0,51	4	0,45-0,9	1
	B2	Green	0,51-0,58	4		
	B3	Red	0,6-0,72	4		
	B4	NIR	0,76-0,89	4		
Alsat-2[9]	B1	Blue	0,45-0,52	10	0,45-0,745	2,5
	B2	Green	0,53-0,59	10		
	B3	Red	0,62-0,69	10		
	B4	NIR	0,76-0,89	10		

Table GI. Examples of Earth observation systems offering various images to different spatial resolutions.

[4]https://earth.esa.int/web/eoportal/satellite-missions/s/spot-4
[5]https://earth.esa.int/web/eoportal/satellite-missions/s/spot-5
[6]https://www.satimagingcorp.com/satellite-sensors/ikonos/
[7]https://www.satimagingcorp.com/satellite-sensors/quickbird/
[8]https://www.deimos.com
[9]https://www.asal.dz

As the high spectral resolution and the high spatial resolution are contained in different images, the problem becomes one of synthesizing multispectral images with the best spatial resolution available within the dataset. Image fusion is one way to offer joint exploitation of information originally from separate sources.

According to [131], it is a formal framework in which the means and techniques are expressed that allows the alliance of data from various sources. Pansharpening is aimed at obtaining higher quality information, which depends on the application and its user.

The term fusion encompasses several possible definitions. For example, the works of [132], [142], [143] and [144] consider the fusion as a combination of relevant information from the two images placed as input, the so-called "relevant" information depending on the application. For example, some of these authors show examples of images acquired by the same sensor but at different focal lengths. They define fusion as the synthesis of an image that is focused at all points that is, having the highest spatial resolution of the two images for each pixel. This idea of complementarily is also found in medical imaging since radio images, obtained by nuclear magnetic resonance or even by positron emission tomography, provide very different information on the human body [145]. Pansharpening aims to overlay relevant information from different sources for diagnostic aid. This way of defining image fusion has the particularity of not taking into account the characteristics of a particular sensor. The challenge lies in the creation of a hybrid image with specific characteristics selected from the different sets placed at the input.

The framework of this research work, that we have adopted, is the particular case of the synthesis of multimodal images with high spatial resolution: each synthesized image must be as close as possible to that which the corresponding sensor could have observed if it had this spatial resolution. This last statement will be for us the fundamental property of fusion products.

The economic interest of creating images reproducing what a multispectral sensor with better spatial resolution should observe is real in the space field, since an efficient fusion method makes it possible to be satisfied with simpler and therefore less expensive, and lighter sensors, which saves weight and space on the platform.

The existing pansharpening algorithms tend to trade-off between spectral distortion and spatial improvement. The major issues with the pansharpening process are two: spectral distortion and decrease of spatial information in the fused image [45]. Many algorithms are proposed to solve these problems respecting the tradeoff between spectral distortion and spatial enhancement, which can fuse huge volume of satellite data of three, four or more

bands. This thesis deals with the evaluation of image fusion methods in order to solve the spatial resolution limitation of high resolution satellite imagery.

GI.3. Objectives of the thesis

The aim of the thesis is to contribute and develop an optimized method for synthesizing images at high spatial and spectral resolutions more efficient than current methods, as well as for evaluating the quality of the fusion results.

The first step of the work consisted in studying the different fusion methods found in the literature in order to be able to exploit some models and develop a more efficient model. The second step was dedicated to the critical evaluation of existing fusion methods and particularly the most recent methods, looking at the development paths chosen by the various authors. The qualitative and quantitative evaluation of their performance has opened up many perspectives for development, justifying the importance of using multi-scale or multi-resolution analysis.

The development framework for the new method that we have chosen is that of the ARSIS concept (*Amélioration de la Résolution Spatiale par Injection de Structures*), that means in English, Improvement of Spatial Resolution by Injection of Structures, in combination with methods based on the IHS transform. The IHS transform was chosen due to its simplicity of implementation and its good results. The new method that we have developed is an improvement of the hybrid method of the ATWT transform ("*à trous*" Wavelet Transform) and the general IHS transform (GIHS) called AWLP. Finally, a comparative study was made between the existing methods in the literature and our new proposed technique.

GI. 4. Followed approach

Several classifications of fusion methods have been proposed, and we have chosen that of [27]. A presentation of the main locations of these three categories is developed. For the high spatial resolution visual assessment which corresponds to the first step of our study, we considered and applied, for all the methods, two images representing an urban area and a vegetation area, respectively.

The development of new algorithms inevitably involves a stage of estimating the quality of the fused products obtained. The bibliography showed that a normative framework for the evaluation of the quality of fusion products is needed. To know the quality of a fusion product, it must be compared to a reference. Chapter 2 presents a critical study of the

quantitative parameters present in the literature then a comparative study was made between the different fusion methods studied in the previous chapter.

Next in Chapter 3, we look at the most recent fusion methods, studying the solutions that the authors have explored to improve the spatial and / or spectral quality of the fused products.

Chapter 4 presents a critical state of the art of fusion methods. A hybrid method has been proposed based on the combination of the IHS transform with the ATWT transform. The proposed scheme shows an improvement of the well-known fusion method called AWLP. The proposed algorithm has been published in Elsevier's Advances in Space Research journal, indexed in the Thomson Reuter Database. The spatial resolution of images and their geometric quality are intrinsically related to the quality of a satellite image sensor. The fusion product quality assessment process was applied to a new set of images processed by this new algorithm as well as by existing methods. These series are acquired by the satellites Deimos-2, Worldview-2 and Worldview-3. The results confirmed that the proposed algorithm is generally valid. It is applicable whatever the images, the ratio or the landscape concerned. For this, we show that the new fusion method must be able to offer a balance between qualitative and quantitative estimations. Analyzes combined with the results from the application of the proposed algorithm, led to the conclusion that the new method is the best fusion method of all those tested in this thesis.

Finally, a conclusion on all the work carried out throughout this thesis, is presented. Development prospects and numerous recommendations are proposed.

Chapter 1: An overview of image fusion methods

1.1. Introduction.

1.2. Pansharpening of multi-spectral satellite images.

1.3. Presentation of the problem.

1.4. Categories of fusion methods.

1.5. Conclusion.

1.1. Introduction

In recent years, image fusion has become an important technique in the field of image processing. The goal of image fusion is to generate a composite image by inputting additional information from different source images of the same scene [1]. In the image fusion system, the input source images can be acquired from different image sensors or from a single sensor with changeable optical parameters. The output of this system is an image, called merged image, which will be more relevant to human and machine perception than an individual source image. The image fusion technique has been used in several applications such as machine vision, surveillance, medical imaging and remote sensing [2].

We must remember, in fact, than high and very high resolution images available for remote sensing are mostly panchromatic images. Conversely, the multispectral images, able to combine into one colorful composition, present more low resolutions. The fusion of a panchromatic image (PAN), of high spatial resolution and of low spectral resolution, with a multispectral image (MS), of low spatial resolution but high spectral resolution, arguably the most frequent application of fusion. This process is called **PAN-sharpening** [3].

In remote sensing techniques, pan-sharpening or image fusion aims to sharpen low spatial resolution multispectral (MS) image by injecting the details extracted from high spatial resolution panchromatic (PAN) image [4].

The aim of this chapter is to present various image fusion techniques as part of the production of a colored composition using optical satellite images. The main constraints will therefore be linked to obtaining an image easily interpreted by a majority of users. The image must present visual qualities, in particular with respect to the colors returned, and offer maximum readability. Finally, to the extent of possible, obtaining natural colors will be sought [3].

1.2. Pansharpening of multi-spectral satellite images

Spatio-spectral fusion, such as PAN/MS (called pansharpening) [5,6], PAN/Hyper-Spectrale (HS) [7,8], and MS/HS [7,9,10], is an important approach in remote sensing image fusion [5] – [7]. It consists in obtaining a fused image with both high spatial and spectral resolutions.

Pansharpening consists of producing a new image which retains part of the information contained in each of the original images. The objective is to create a synergy, which is to say to obtain an image merged geometrically and / or semantically richer than an initial image. Many methods are capable of performing image fusion. They differ in the way in which they

favor a particular characteristic of the original images. The choice of a method is therefore conditioned by the application.

The implementation of an image fusion requires several preliminary operations which directly interfere with the quality of the fused product. Among these, the geometric correction of the images subjected to the fusion is obviously essential since the images must be strictly super imposable. But the pre-treatments involved in radiometry are also important and diverse [3].

The goal of pansharpening is to combine the high spatial resolution of the panchromatic image (PAN) with the precise spectral information of the multispectral image (MS). The resulting image should have a high visual quality to facilitate detection and classification tasks. However, the merged image must contain the same spectral information (colors) as the original multispectral image.

This becomes especially important as the number of bands increases, because the spectral signature can be used for material identification. Therefore, the pan-sharpened image should possess both high spatial and spectral qualities [11].

1.3. Presentation of the problem

It is interesting to visualize remote sensing images with high spatial and spectral resolutions as it can lead to better land classification, map update, soil analysis, feature extraction, etc. However, constraints, such as the compromise between the high resolutions of the sensor, the bandwidth of the channel, the storage capacity on board a satellite, etc..., limit the acquisition of images with high spectral and spatial resolutions. Because of this, many commercial remote sensing satellites such as Alsat, Quickbird, Ikonos, and Worldview capture the earth's information with two types of images: a single panchromatic (PAN) image and a number of multispectral (MS) images. The PAN image has high spatial resolution with lower spectral resolution, while an MS image has higher spectral resolution with low spatial resolution.

The pansharpening or multiresolution image fusion is an algorithmic approach to increase the spatial resolution of the MS image with the preservation of spectral contents by making use of the high spatial resolution PAN image [12].

The main spectral characteristic of the PAN image is to cover a wide range of the wavelength spectrum; on the contrary, an MS band covers only a narrow spectral range.

Since more energy comes to PAN sensor, time acquisition can be reduced still preserving the same intensity response as MS images in terms of the number of photons [5].

If the spectral responses of all the sensors of a satellite satisfied the ideal theoretical graph of Figure 1.1 [5], the hypothesis of relative spectral contribution would be perfectly true. The black curve represents the ideal spectral response of the PAN modality. The colors correspond to the MS modalities, where the blue, green, red and brown colors correspond respectively to the blue, green, red and NIR bands of the sensor.

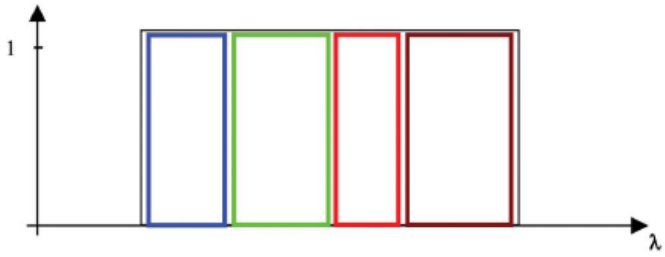

Figure 1.1. Ideal normalized spectral responses in terms of wavelength [5].

This figure is not realistic. It would never equal a linear combination with the MS responses if the panchromatic image was simulated by a combination of actual multispectral acquisition. MS air-borne or space-borne sensors do not offer a constant response over the whole bandwidth. This bandwidth is characterized by a variable response and generates a partial overlap between the spectra.

Figure 1.2 shows the normalized response of the spectral bands of the Ikonos satellite sensors as a function of wavelength in µm. The black curve represents the spectral response of the Ikonos PAN image. The color curves correspond to the MS modalities, where the blue, green, red and brown colors correspond respectively to the blue, green, red and near-infrared bands of the sensor [5].

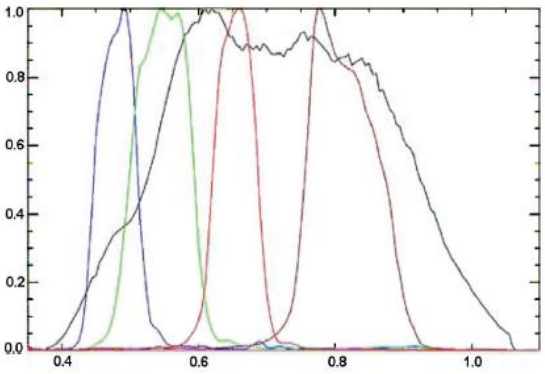

Figure 1.2. Responses of the different spectral bands as a function of the wavelength in micrometers (Ikonos satellite). Black, brown, red, green and blue curves, respectively, correspond to PAN, NIR, red, green and blue modalities[1].

[1]http://www.geoeye.com/products/imagery/ikonos/spectral.htm.

In Figure 1.2, if an object reflects solar incident energy in wavelengths located around 1 μm, it will be impossible to infer the pixel value in the PAN image from other MS sensors since what this pixel will have a grayscale value equal to 0 in all MS images. Moreover, this figure shows that blue and green channels interference creating spectral redundancy between the two images [5].

Even for geometrically recorded PAN and MS images, differences may exist between these modalities. In addition to the changes produced by their different spectral acquisition bands, profound changes can also occur in the same scene for two different acquisition times. Many authors attempt to understand relationships between these remotely sensed images for the development of their fusion method [5].

In general, the MS and PAN modalities often display the same geographic area. It is assumed that the PAN and MS input data sets are *a priori* geometrically registered. The task of registration is a very challenging one [13], particularly when images come from different platforms. Reference [14] has shown that a geometric standard deviation distortion of 0.1 pixels produces a considerable effect on the quality of the merged images resulting from a pixel-to-pixel fusion process.

However, even with perfectly registered images, the sets (PAN, MS) can present a certain local dissimilarity, the origin of which is not always well understood by the fusion community [15,16]. This can have an impact on the quality of the resulting images.

Several types of dissimilarities are illustrated and discussed in [5,17]. The most common dissimilarities are: moving objects, occlusion of objects, inversion of contrast and due to the different spectral bands of the sensors or the different acquisition times. These effects are due to the physics of the environment. If they are not taken into account, the success of the merge process could be compromised by the appearance of artifacts.

The steps prior to the fusion are:

- **The selection of images:**

The criteria for selecting satellite images must be clearly established according to the objectives.

One of the criteria is the choice of the spatial resolutions of the images. The high-resolution image can only be effectively merged within certain limits with images of coarser resolutions [3]. It is desirable to respect a resolution ratio R_{res} when choosing the images to be merged which must verify the following condition:

$$R_{res} = \frac{L_{res}}{H_{res}} \leq 5 \quad (1.1)$$

Where:

L_{res} : Low resolution

H_{res} : High resolution

Another important criterion in the selection of images to be merged is the acquisition date. Similar recording dates are recommended, as in any multi-source manipulation, to avoid deviations of a pheno-logical, climatic, sunshine, humidity, etc. between the images [3].

Finally, when the sensors are not limited to zenith shots, the angle of view constitutes another criterion to be taken into account in the selection of the images. Geometric correction will be more difficult when viewing angles are distinct [3].

- **Geometric corrections:**

The principle consists in first rectifying the image of higher spatial resolution, often panchromatic, which will serve as a reference. The correction method chosen depends on the type of image, relief, viewing angle, etc. Then, the image of lower spatial resolution is brought to the resolution of the reference image by multiplication of pixels. It is then geometrically corrected by matching with the high resolution image already corrected.

For digital satellite images, the geometric correction methods applicable to the high resolution image are those of polynomial transformations resolved by least squares [3]. The geometric correction operation is always accompanied by a procedure for resampling the pixels of the original images. The method used for resampling is the bilinear or cubic interpolation technique to take advantage of the anti-aliasing effect during resampling [3].

Reference [10] proposes an integrated framework for the spatial, temporal and spectral fusion of images in remote sensing. In the framework of the proposed fusion, the maximum posterior theory (MAP) is used to describe the reverse fusion problem. The spatial, temporal and spectral relationships between the desired image and the remote sensing observations, obtained by different sources, are then analyzed in depth to build an integrated relationship model.

1.4. Categories of fusion methods

To date, an oversized range of pansharpening methods are planned [18,19,20] and these methods are classified in many other ways. Reference [21] classified the existing

pansharpening methods into two major categories, i.e., the component substitution (CS)-based methods and the multiresolution analysis (MRA)-based methods. Reference [22] classified the existing pansharpening methods into the CS-based methods, the MRA-based methods, and the regularized-based methods. In addition, [23] classified them into the CS-based methods, the MRA-based methods, and the Bayesian-based methods, and [10] classified them into the CS-based methods, the MRA-based methods, the sparse reconstruction (SR)-based methods, and the model-based optimization (MBO)-based methods. It should be noted that regularization-based methods, Bayesian-based methods, MBO-based methods, and SR-based methods are converted to a variational model optimization, so they can be generalized in variational optimization (VO) -based methods. References [24,25] classified the existing pansharpening methods according to the use or not of the Point Spreading Function (PSF).

However, few papers provided a complete analysis of CS-based methods, MRA-based methods and, in particular, VO-based methods.

Excitingly, [26] first performed a comprehensive review of the VO-based strategies supported super-resolution conception [27].

Reference [27] has presented a review of all categories of the pansharpening methods for remote sensing images based on the idea of meta-analysis.

The three main categories of pansharpening methods, i.e., the CS-based methods, the MRA-based methods, and the VO-based methods, are presented in the next sections, including the process of development from the traditional understanding to the current understanding.

1.4.1. Component substitution (CS)-based methods

The CS-based methods are the simplest to implement and the most widely used in pixel-to-pixel fusion and are part of most professional remote sensing software including ENVI, ERDAS Imagine, PCI Geomatica, etc. The idea of the traditional CS -based methods is that the MS image is first projected into a new spectral space; a component of them which represents the spatial information is replaced by the PAN image and the reverse projection is finally performed to obtain the pansharpened image. Therefore, they are also generally called “projection-substitution” methods [5]. The essential methods include the Intensity-Hue-Saturation (IHS) methods [18,28], the Principal-Component-Analysis (PCA) methods [18,29,30], the Gram-Schmidt (GS) methods [31], etc. Figure 1.3(a) shows the flowchart of the traditional understanding of the CS-based pansharpening methods.

Thereafter, [32] demonstrates that the CS-based methods can be generalized to a new formalization and this was then extended in [33,34]. The new understanding, as shown in Figure 1.3(b), is that this category of methods is based on the simple substitution of a single component by the PAN image, and the component is usually obtained by a linear combination of the spectral bands of the MS images, like the standard GSA (adaptive GS) [35] and BDSD (band-dependent spatial detail) [36] methods, etc. It should be noted that in fact, it is a question of extracting the information of high spatial structure of the PAN image through the difference between the PAN image and the component, and this high information structure is then injected into the MS image by an appropriate injection scheme.

This can be represented as:

$$\widehat{M} = \widetilde{M} + g(P - I_L) \qquad (1.2)$$

Where $\widehat{M}$ is the fused image, $\widetilde{M}$ is the resampled MS image, I_L denotes the component to be substituted, P denotes the PAN image, which is generally normalized (e.g. by histogram matching) with I_L to reduce the spectral distortion and g is the injection weight.

The normalization operation is a common strategy used to reduce the color distortion of the fused image by matching the spectrum of MS to that of PAN [37]. This adjustment consists of making the statistical distribution of pixel values of the panchromatic image as close as possible to that of channel I [3].

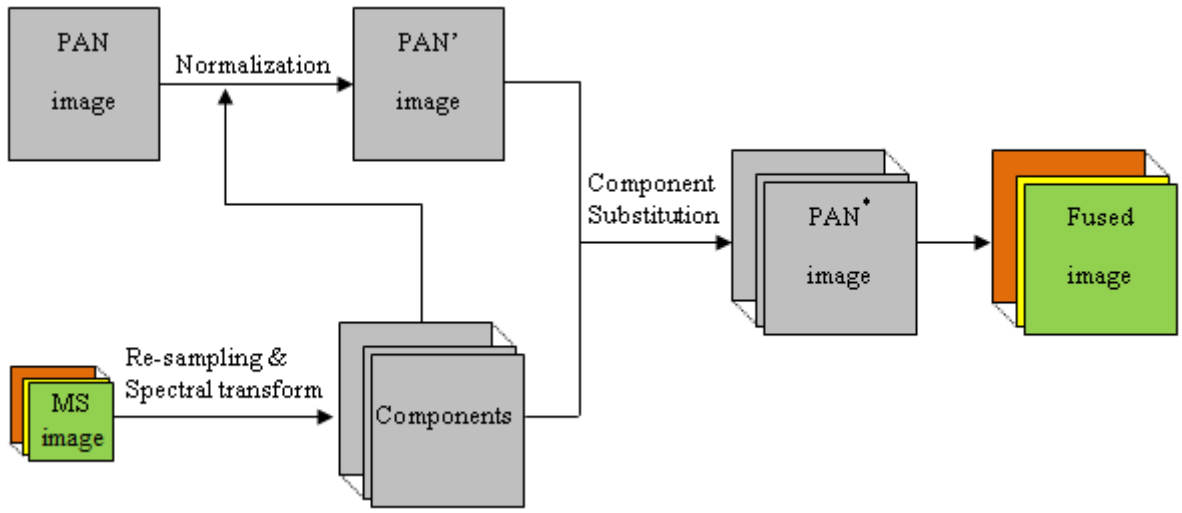

a) Traditional understanding of the CS-based methods.

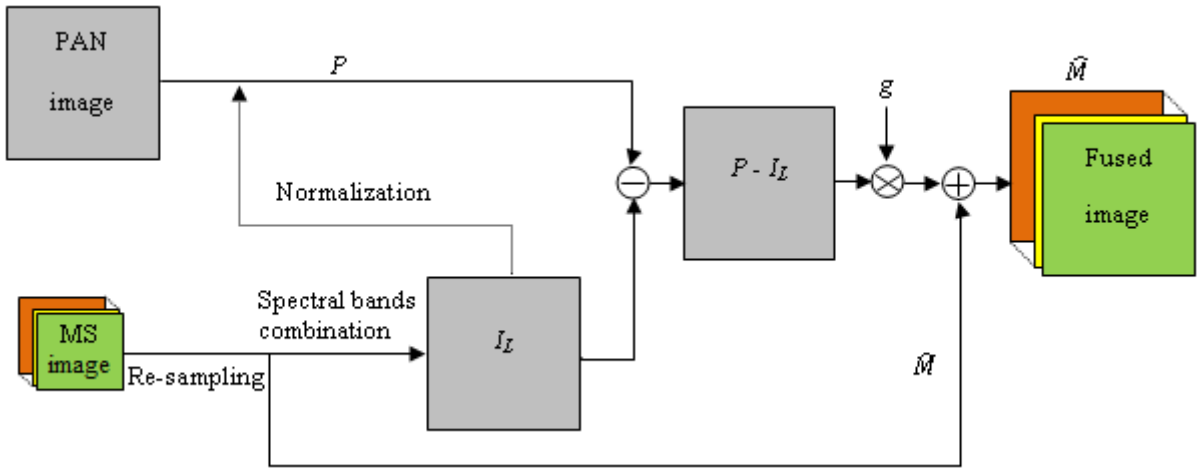

b) New understanding based on the general formalization of the CS-based methods.

Figure 1.3. Flowchart of the CS-based pansharpening methods.
(a) The traditional scheme of the CS-based methods.
(b) The new understanding based on the general formalization of the CS-based methods.

1.4.1.1. Advantages

The general formalization of the CS-based methods has two major advantages:

1) It leads to faster implementation of traditional methods. However, it should be noted that this should satisfy the condition that the component to be substituted is generated linearly from the available spectral bands.
2) It opens up new horizons for the development of this type of method. A number of improved methods have subsequently been proposed. In general, improvements to the CS-based methods have mainly focused on the optimal determination of the I_L component and the injection gain g.

In conclusion, there are several popular solutions. On the one hand, I_L is calculated from the previous simple mean of the spectral bands of the MS image [28,31,38], to the improvement by the spectral response functions of the sensors [34,39], and the optimal calculation by least squares regression [35,40,41]. On the other hand, it is calculated from global solutions [18,29,30,38] to optimal solutions by consideration of the local features [42,43]. For the determination of the injection weight g, a variety of solutions can be applied [6,19,44]. On one hand, in the spatial dimension, the injection weight can be determined by a global model [35] or a local model [45]. On the other hand, in the spectral dimension, the

injection weight may be equal for all the spectral bands [32], or determined by a band-dependent solution [31].

1.4.1.2. Some (CS)-based methods

1.4.1.2.1. Intensity Hue Saturation (IHS) pansharpening technique

The IHS pansharpening method is one of the most used fusion techniques and it is a standard procedure in image analysis for color enhancement, feature enhancement, improvement of spatial resolution and the fusion of data sets [46]. In the IHS space, spectral information is mostly projected on the hue and the saturation. From the visual system, the intensity change has little effect on the spectral information and is easy to deal with. The purpose of fusion is to ensure the spectral information and to add the detail information of high spatial resolution; therefore, the fusion is even more adequate for processing in IHS space [47].

In the literature, many IHS transformation algorithms have been developed. Some are called HSV (hue, saturation, value) or HLS (hue, luminance, saturation) [48].

1.4.1.2.1. A) IHS transform

The IHS transformation, which is defined as a colored combination of three channels, allows color information to be retrieved.

Generally, the most common color representation spaces use the three modalities corresponding to the primary colors of the RGB spectrum "Red (R), Green (G) and Blue (B)".

IHS is a three-dimensional representation of the color space defined by Smith in 1978. Figure 1.4 shows the defining cone of the model.

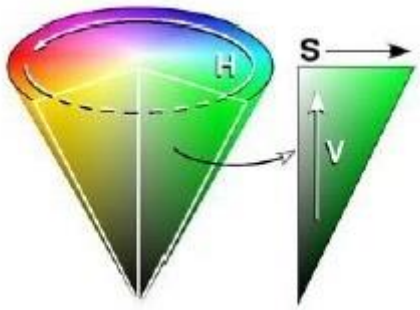

Figure 1.4. Smith's HSV color model.

The transition from RGB space to HSV space can be achieved using the following process (Figure 1.5):

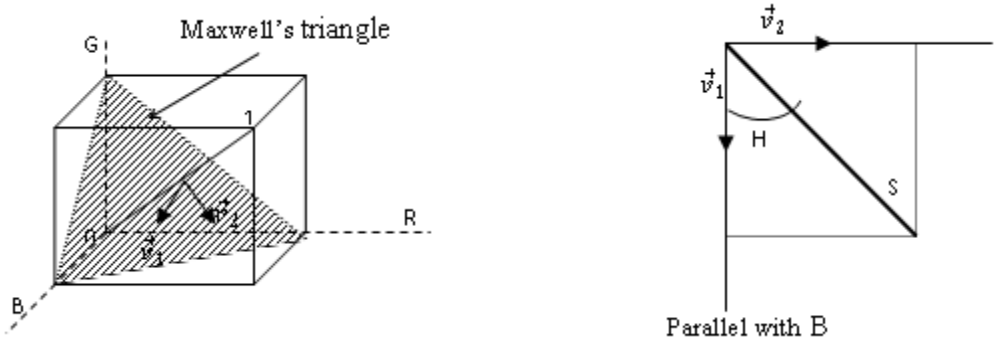

a) Color cube and Maxwell's triangle b) Hue and saturation in the Maxwell plane

Figure 1.5. RGB to HSV transformation.

Any color is represented by a vector in the cube, originating from black and as a norm, the vector sum of its three components R, G and B.

The gray diagonal is considered as the axis of intensities varying from 0 for black to 1 for white. The intensity of a color corresponds to the length of the projection of its vector on the gray diagonal.

The hue and saturation values are calculated in polar coordinates in the Maxwell plane, defined as the plane perpendicular to the gray diagonal and passing through the vertices of the R, G and B axes. The hue is the angle polar between 0 and 360° and whose origin is fixed by the direction of the blue axis of the cube (sometimes the red). Finally, saturation is the length of the polar radius joining the color vector to the gray diagonal.

The relationship allowing the switch from RGB mode to HSV mode, and vice versa, appears in numerous works, such as, [18,28,32,49,50], etc. A comparative study of different models of the IHS transform was made in [48]. Taking the formulation proposed by Marion which guarantees an exact conversion in both directions of the transformation [3]:

$$\begin{pmatrix} I \\ v_1 \\ v_2 \end{pmatrix} = \begin{pmatrix} 1/3 & 1/3 & 1/3 \\ -1/2 & -1/2 & 1 \\ \sqrt{3}/2 & -\sqrt{3}/2 & 0 \end{pmatrix} \begin{pmatrix} R \\ G \\ B \end{pmatrix} \quad (1.3)$$

With:

$$\begin{cases} H = arctan\frac{v_2}{v_1} \\ S = \sqrt{v_1^2 + v_2^2} \end{cases} \quad (1.4)$$

The relation allowing returning to the RGB mode from the IHS mode is obtained by carrying out the following equations:

$$\begin{cases} v_1 = S\cos H \\ v_2 = S\sin H \end{cases} \quad (1.5)$$

And:

$$\begin{pmatrix} R \\ G \\ B \end{pmatrix} = \begin{pmatrix} 1 & -1/3 & 1/\sqrt{3} \\ 1 & -1/3 & -1/\sqrt{3} \\ 1 & 2/3 & 0 \end{pmatrix} \begin{pmatrix} I \\ v_1 \\ v_2 \end{pmatrix} \quad (1.6)$$

To illustrate this passage, we take the example of an RGB image in the following figures:

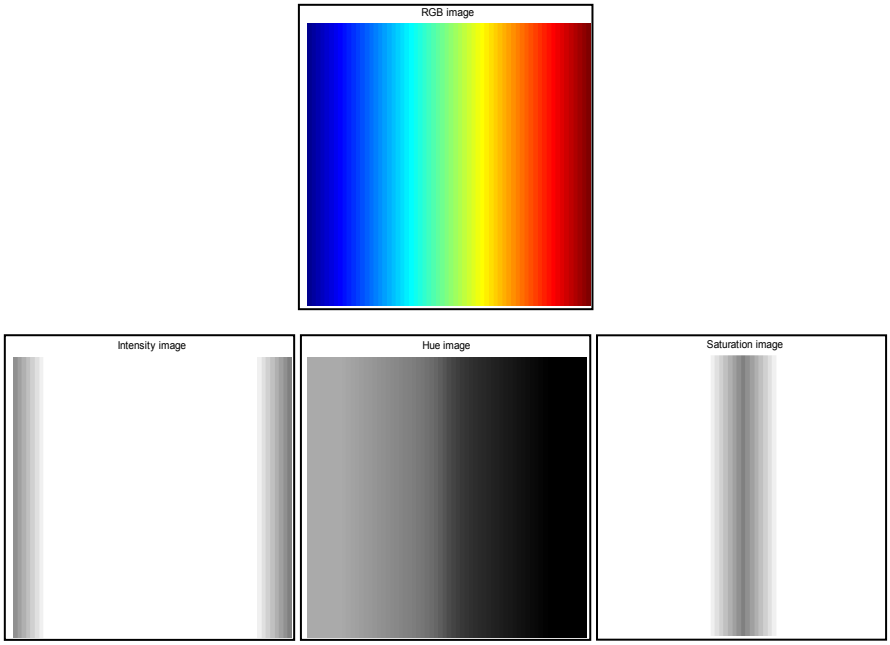

Figure 1.6. An example of transformation from RGB space to IHS space[2].

[2] MATLAB images

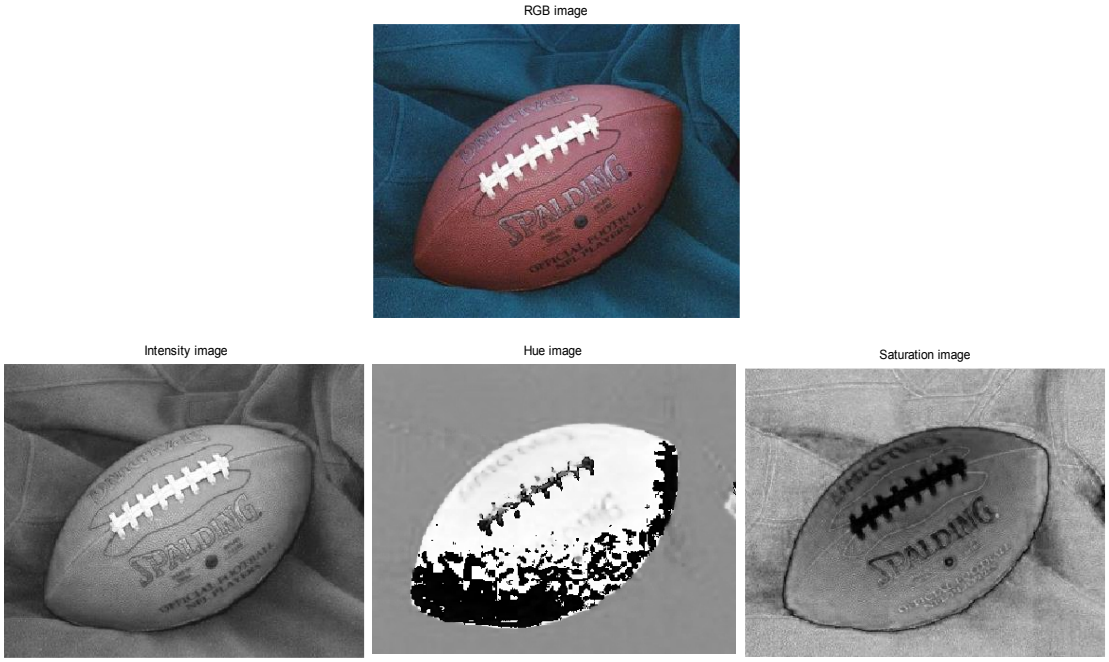

Figure 1.7. Another example of transformation from RGB space to IHS space[2].

The Hue values show a linear transition from top to bottom. If we compare the tinted image and the original image, we can see that the shades of blue have the highest values, and the shades of red have the lowest values.

The saturation can be thought of as the purity of a color. The saturation image shows that the colors with the highest saturation are shown as white. The center of the image, where there are shades of gray, is a mixture of colors.

The intensity image gives the brightness represented by light areas which correspond to the brightest colors in the original image.

1.4.1.2.1. B) IHS pansharpening algorithm

Figure 1.8 represents this process. Color image RGB space is converted to the IHS space. The I (intensity) band is replaced by the panchromatic PAN image and it is calculated using:

$$I = \sum_{i=1}^{N} \alpha_i MS_i \qquad (1.7)$$

Where MS_i the *ith* band of the MS image and α_i = 1/3. Yet, most multispectral images consist of four bands, RGB and an infrared band. Researchers have extended this method for other multispectral images by using α_i=1/N where N is the number of bands [51,52]. For the IKONOS satellite, the coefficients α were experimentally determined [53].

Before fusing the two images, a histogram matching of the panchromatic image P is applied to ensure that the mean and standard deviation of the panchromatic and multispectral images are within the same range, using:

$$P^* = \frac{\sigma_I}{\sigma_P}(P - \mu_P) + \mu_I \quad (1.8)$$

Where μ_P and σ_P are the mean and standard deviation of the PAN image and μ_I and σ_I are the mean and standard deviation of the intensity image, respectively.

Finally, the fused multi-channel image F is obtained by [40]:

$$F_i = MS_i + (P^* - I) \quad (1.9)$$

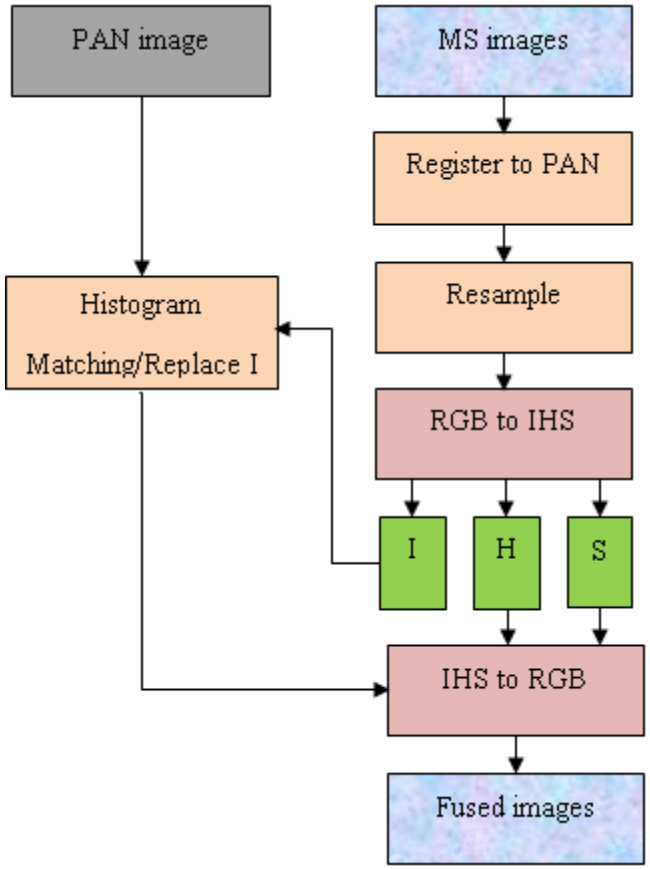

Figure 1.8. Scheme of IHS image fusion.

1.4.1.2.2. Principal Component Analysis (PCA) pansharpening technique

PCA transformation, developed by Pearson in 1901 and Hotelling in 1933, is a technique derived from statistics to simplify a set of data, while the best modern benchmark is Jolliffe in 2002. The goal of this method is to reduce the size of the data while preserving as

much relevant information as possible. By using this method, the redundancy of the image data can be decreased as it converts the correlated data set into an uncorrelated data set [46].

1.4.1.2.2. A) PCA transform

The eigenvalues λ of a matrix A are the scalars verifying the following characteristic equation:

$$\det(A - \lambda I) = 0 \tag{1.10}$$

Where, I is the identity matrix.

The eigenvectors V associated with the eigenvalues λ verify the following equation:

$$AV = \lambda IV \leftrightarrow (A - \lambda I)V = 0 \tag{1.11}$$

Let V be the unit matrix whose columns represent the eigenvectors $V = (v_1, \ldots, v_n)$, with $v_k = \left(v_{1,k}, \ldots, v_{n,k}\right)^t$. The k^{th} component P_k of the PCA transform is given by:

$$\begin{pmatrix} \cdots \\ \cdots \\ P_k \\ \cdots \\ \cdots \end{pmatrix} = \begin{pmatrix} v_{1,1} & \cdots & \cdots & \cdots & v_{1,N} \\ \cdots & \cdots & \cdots & \cdots & \cdots \\ v_{k,1} & \cdots & \cdots & \cdots & v_{k,N} \\ \cdots & \cdots & \cdots & \cdots & \cdots \\ v_{N,1} & \cdots & \cdots & \cdots & v_{N,N} \end{pmatrix} \begin{pmatrix} MS_{1,1} \\ \cdots \\ MS_{k,1} \\ \cdots \\ MS_{N,1} \end{pmatrix} \tag{1.12}$$

So:

$$P_k = \sum_{p=1}^{N} v_{p,k}.MS_{p,1} \tag{1.13}$$

If C corresponds to the covariance matrix (cov) of the set B where $C(i,j) = cov\left(B_i, B_j\right)$, then C is a symmetric matrix, which also implies that this matrix is diagonalizable:

$$V^t\, C\, V = \begin{pmatrix} \delta_1 & 0 & \cdots & 0 \\ \cdots & \cdots & \cdots & \cdots \\ \cdots & \cdots & \cdots & 0 \\ 0 & \cdots & \cdots & \delta_N \end{pmatrix} \tag{1.14}$$

Where $\{\delta_1, \ldots, \delta_n\}$ are the eigenvalues in descending order: $\delta_1 > \cdots > \delta_N$. The total variance is equal to the sum of δ_k with $k = \{1, \ldots, N\}$ [17].

1.4.1.2.2. B) PCA pansharpening algorithm

The multispectral MS image is transformed by PCA transform. The eigenvalues and corresponding eigenvectors of correlation matrix between the images in the individual bands of the multispectral image are calculated to obtain the principle components of each matrix. The matched PAN image replaces the first principle component of the multispectral MS image, and then we get the new first principle component. This later and the other principle components are used in inverse PCA transformation to form the fused image. We replace the first principal component image with PAN image data because the first principle component image has the common information to all the bands [29] (see Figure 1.9).

The role of image registration is to make the pixels in different images coincide precisely [54,55].

As in any substitution, it is recommended to adjust the variance and the mean of the high-resolution channel to those of the first component before replacing [3].

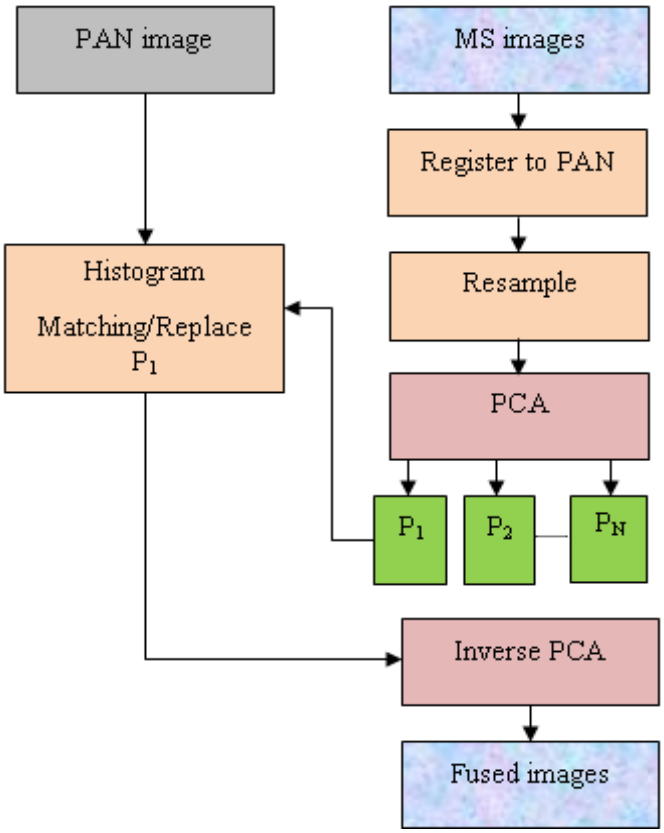

Figure 1.9. Scheme of PCA image fusion.

1.4.1.2.3. Brovey Transform (BT) pansharpening technique

The BT pansharpening method preserves the relative spectral contribution of each pixel and replaces its overall luminance with the panchromatic image [56]. It is calculated by:

$$\begin{bmatrix} R_{BT} \\ G_{BT} \\ B_{BT} \end{bmatrix} = \frac{PAN}{I} . \begin{bmatrix} R \\ G \\ B \end{bmatrix} \quad (1.15)$$

And I, is the intensity of resized MS image calculated as above [57].

The group of methods defined by (1.2), varying with the choice of spectral weights in (1.7), is sometimes referred to as *relative spectral contribution* (RSC) [5,58]. In this thesis, however, following [44], all CS methods are considered as a unique class. According to (1.2), RSC can be seen as a particular case of the CS class since such methods can be formalized and exhibit the same features as all CS methods [21,6].

1.4.1.2.4. Gram Schmidt (GS) pansharpening technique

GS transform was first introduced for image fusion by Laben and Brower in 2000 [42]. The GS method can be calculated as:

$$I = \sum_{i=1}^{N} \alpha_i MS_i \quad (1.16)$$

And:

$$F_i = MS_i + g_i(P - I) \quad (1.17)$$

Where, α_i is the weighting factor; $\alpha_i = 1/N$, $N$is the number of MS image bands and g_i is the injection gain and is calculated as $g_i = cov(I, MS_i)/var(I)$, where $cov(A, B)$ denotes the covariance between images A and B, and $var(A)$ is the variance of image A [59].

1.4.1.3. Examples of pansharpening of some (CS)-based methods

Four-band multispectral data, representing pansharpening an urban and vegetation scenes, was used for the following examples to show the results of different (CS)-based fusion techniques (figures 1.10 and 1.11, respectively). The algorithms were implemented in Matlab.

PAN image is 1024x1024 pixels and the MS is an R, G and B color composition image with 256x256 pixels and with ratio 4.

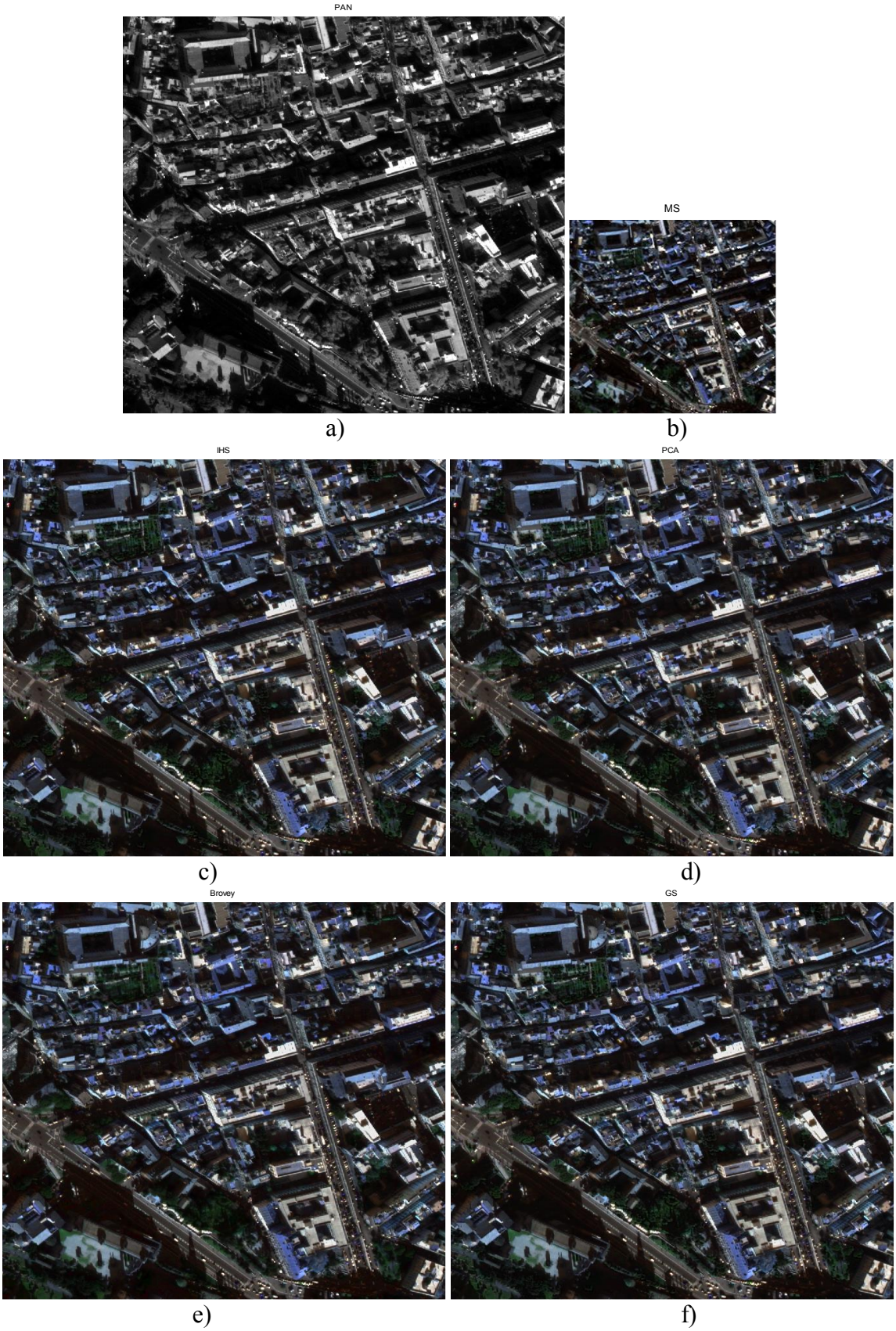

Figure 1.10. Pansharpening urban scene. a) PAN image[2]. b) Real size MS image[2]. c) IHS fused image. d) PCA fused image. e) BT fused image. f) GS fused image.

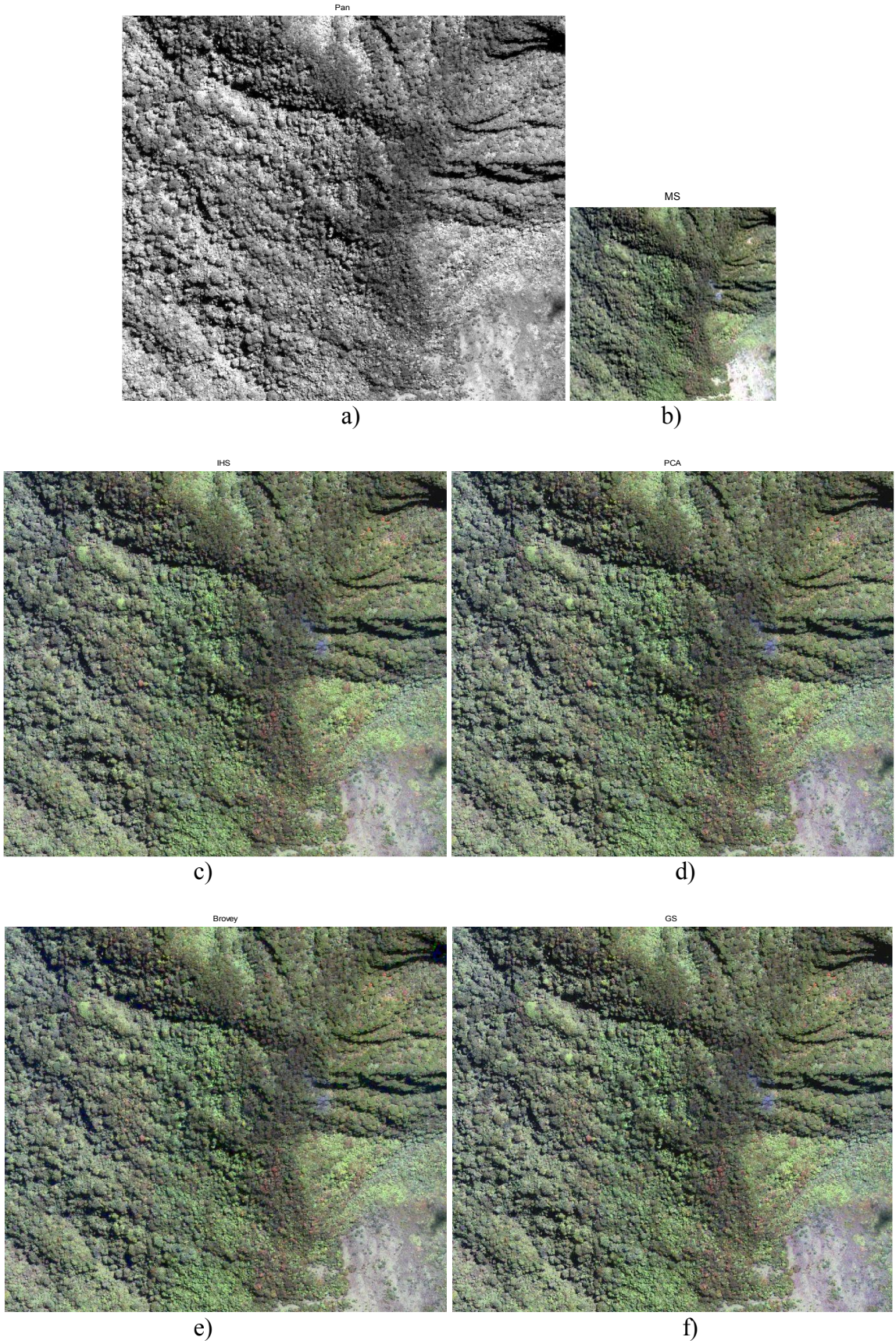

Figure 1.11. Pansharpening a vegetation scene. a) PAN image[2]. b) Real size MS image[2]. c) IHS fused image. d) PCA fused image. e) BT fused image. f) GS fused image.

1.4.1.4. Visual Analysis

The best evaluation of spatial quality of fused images is visual test. In this test, the edges, boundaries, blurring and other details are noticed.

The resampled true color MS image is considered the visual reference for evaluating spectral quality and visual inspection. The MS image is resampled (interpolated) to the size of the PAN image using bilinear interpolation.

Visual inspection can reveal that the classical IHS method produces images with excellent visual quality, but the fused images contain noticeable spectral distortions. It provides more spatial details, while the BT preserves better spectral information. In general, PCA and IHS-based approaches produce results with larger spectral distortion. This is due to overusing the PAN image. The colors look visually very different from those of the original MS image. The GS method has good spatial details but little color distortion.

The boundary of urban area is more distinct and the contrast is clearer. The spatial details are a little blurred because of the significant change of contrast of the fused images. This is due to the replacement of substituted component to the histogram matched PAN image. In vegetation areas of the fused images, we found an obvious spectral distortion.

The obtained results give evidence that the good visual appearance and the spectral content preservation represent the main salient features of the CS-based methods. The attractive visual characteristics of the CS-based methods were highlighted by the absence of aliasing. Their widespread use is supported by such favorable characteristics, as well as the robustness of these methods to errors induced by a possible bad recording between the available MS and PAN Datasets and a relatively low computational load.

1.4.2. Multiresolution analysis (MRA)-based methods

The MRA-based methods originated in the 1980s [60] which are based on extracting the high frequency details from the PAN image and injecting them into the MS image. This fusion idea is generalized using the ARSIS concept [12]. The traditional idea of the MRA-based methods is [62]: “The high-frequency channels coming from the PAN decomposition are inserted into the corresponding MS band channels, decomposed into a series of band-pass channels based on wavelet transform or Laplacian pyramids, etc., before the reconstruction step”. Figure 1.12(a) shows the flowchart of the traditional idea of the MRA-based pansharpening methods.

Reference [32] subsequently extended the MRA methods based on the general formalization, and this general formalization was further extended in [6,33,62] as a unifying framework. Most of the MRA-based methods can be explained by:

$$\widehat{M} = \widetilde{M} + g(P - P_L) \tag{1.18}$$

Where, $\widehat{M}$ is the fused image, $\widetilde{M}$ is the MS image, P is the PAN image, g the injection gain and P_L is the low pass version of the PAN image.

The main difference between CS-based and MRA-based methods is how to extract high spatial details from the source images.

For the MRA-based methods, the difference between the PAN image and its low-pass version P_L is calculated to obtain the high spatial detail information. The scheme of the MRA-based methods based on a general formalization is shown in Figure 1.12(b).

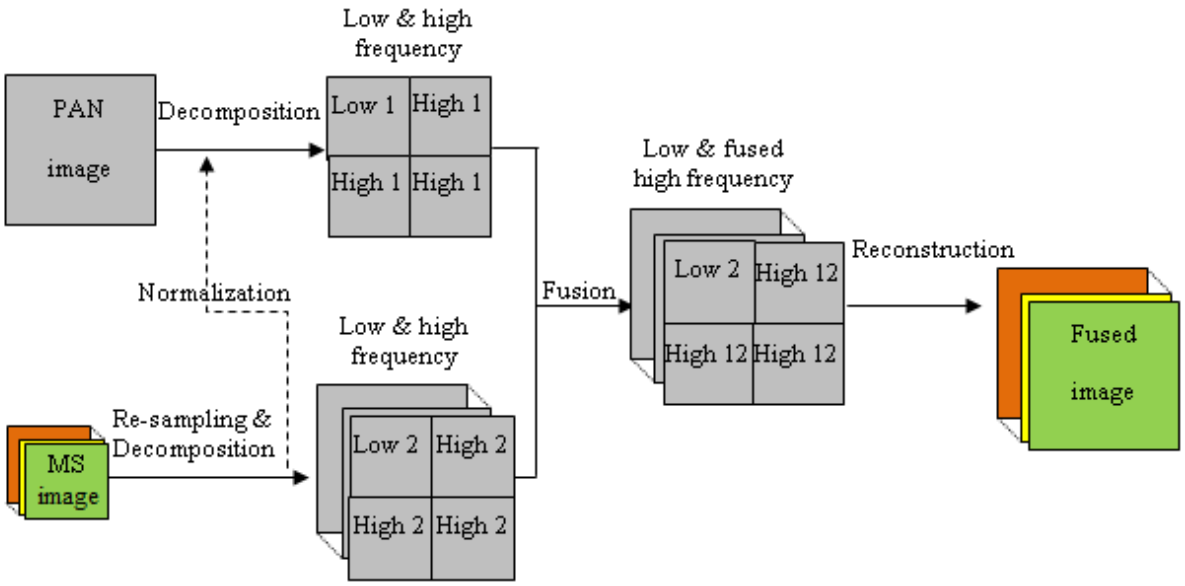

a) Traditional undestanding of the MRA-based methods.

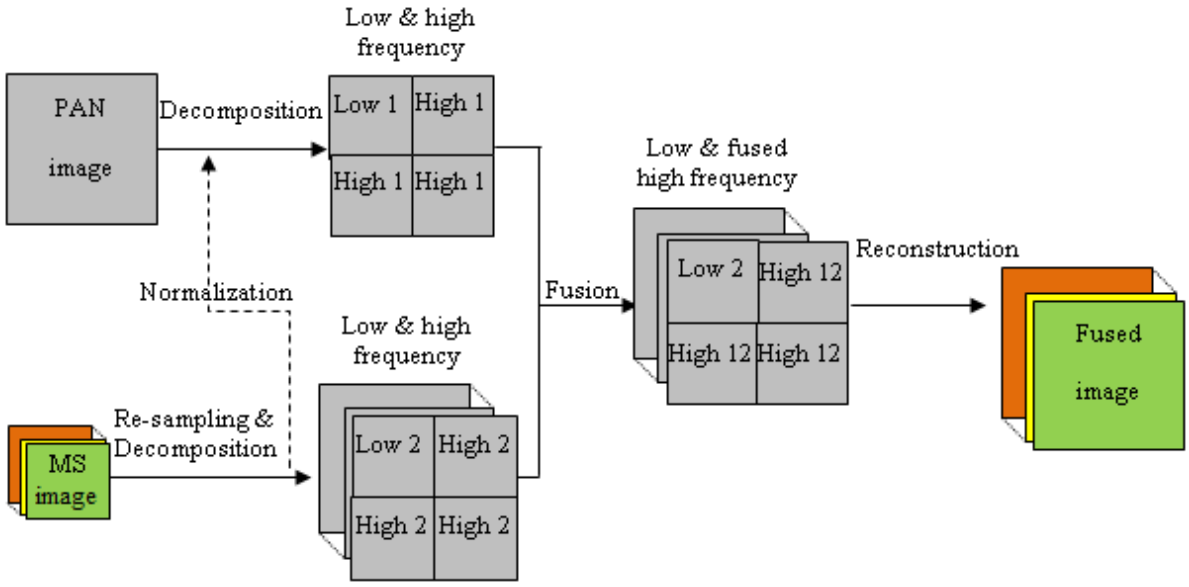

b) New understanding based on the general formalization of the MRA -based methods.

Figure 1.12. Flowchart of the MRA-based pansharpening methods.
(a) The traditional scheme of the MRA-based pansharpening methods.
(b) The new understanding scheme based on the general formalization of the MRA -based pansharpening methods.

The MRA-based methods are characterized by the method of obtaining the image P_L and the injection gain g. For the solution of P_L, there is a number of ways. Among of these methods:

- Methods based on single-level decomposition, such as the High-Pass Filter (HPF) method [18,60].
- Methods based on multiresolution analysis algorithms and methods based on more general MRA framework.

The pansharpening methods based on multiresolution Discrete Wavelet Transform (DWT) [61,63,64] are popular due to their better spectral preservation capacity. However, due to the existence of down-sampling in the wavelet decomposition, artifacts usually appear in spatial structures. Therefore, pansharpening methods based on discrete un-decimated wavelet transformation (UDWT) [65,66], in particular the "à trous" wavelet transformation method [62,67,68,69] have been proposed and attracting more and more attention, such as the popular additive wavelet luminance proportional (AWLP) method [70,67]. In addition, the

Generalized Laplacian Pyramid (GLP) [71,72], the Contourlet Transform [73,74], and the Curvelet Transform [75] are also MRA-based methods and have become popular.

Overall, the calculation of P_L can be divided into two ways, i.e., the calculation based on decimated filters and undecimated filters. For the calculation with the undecimated filters, the low-pass version P_L has the same spatial dimension with P. For processes with decimated filters, such as the DWT filter, the low pass band P_L must go through the operation of downsampling and then interpolation, which usually leads to artifacts. However, it should be noted that MRA-based methods would work best if the filters used are tightly tuned to match the Modulation Transfer Function (MTF) of the sensor [70,71,72], such as the typical MTF-GLP method [72].

The determination of the injection weight g is similar as in the CS-based methods. Among of the most popular injection models are High-Pass Modulation (HPM) [76], the Context-Based Decision (CBD) model [77], the Spectral Distortion Minimizing (SDM) model [77], and the representative methods including the MTF-GLP-HPM and MTF-GLP-CBD [77], etc.

1.4.2.1. Some MRA-based methods

1.4.2.1.1. Discrete Wavelet Transform (DWT) pansharpening technique

1.4.2.1.1.1. A) DWT transform

Wavelets offer good resolution in the time and frequency domains, they have been widely used in image processing which provides multiresolution decomposition of an image in a bi-orthogonal basis and results in a non-redundant image representation. The bases are called wavelets and these are functions generated by translation and dilation of mother wavelet. In wavelet analysis, the signal is broken down into scaled (expanded) and shifted (translated) versions of the chosen mother wavelet or function. A wavelet, as the name suggests, is a small wave that basically grows and decays within a limited amount of time. A wavelet must satisfy two basic properties:

(i) The time integral should be zero:

$$\int_{-\infty}^{+\infty} \Psi(t)dt = 0 \qquad (1.19)$$

(ii) The time-integrated wavelet square is the unit:

$$\int_{-\infty}^{+\infty} \Psi^2(t)dt = 1 \tag{1.20}$$

The wavelet transform of a 1D signal *f (x)* based on wavelet functions is defined as:

$$W_{a,b}\big(f(x)\big) = \int_{x=-\infty}^{+\infty} f(x)\,\Psi_{a,b}(x)dx \tag{1.21}$$

The basis is obtained by translation and expansion of the mother wavelet as:

$$\Psi_{a,b}(x) = \frac{1}{\sqrt{a}}\Psi\left(\frac{x-b}{a}\right) \tag{1.22}$$

The mother wavelet would localize in both spatial and frequency domain and it has to satisfy zero mean constraint. In the Discrete Wavelet Transform (DWT), the expansion factor a is 2^m and the translation factor b is $n2^m$, where m and n are integers.

The information flow in one level of 2D image decomposition is illustrated in Figure 1.13. Wavelet separately filters and down-samples the image in the vertical and horizontal directions (separable filter bank). The input image $I(x,y)$ is filtered horizontally by a pair of filters, low-pass filter (L) and high-pass filter (H), then downsampled by a factor of two to create the coefficients matrixes $I_L(x,y)$ and $I_H(x,y)$. $I_L(x,y)$ and $I_H(x,y)$ are both vertically filtered by L and H and then downsampled by a factor of two to create $I_{LL}(x,y)$, $I_{LH}(x,y)$, $I_{HL}(x,y)$, and $I_{HH}(x,y)$ subbands (sub-images) [78].

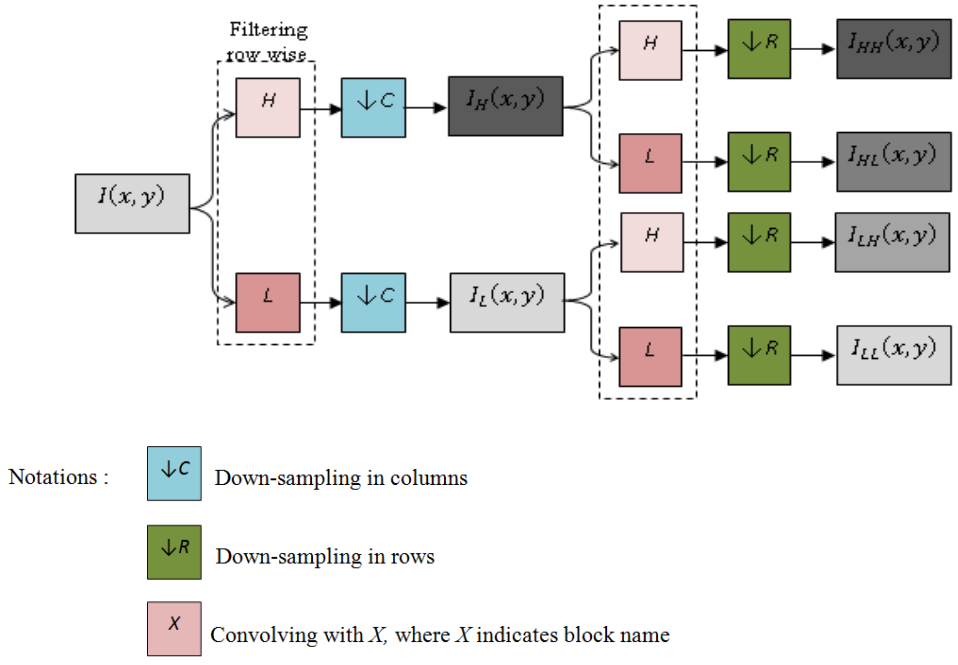

Figure 1.13. One decomposition level of 2D image.

$I_{LL}(x,y)$ contains the low frequency band of the multiscale decomposition. It can be thought of as an approximate smoothed and downsampled version of the source image $I(x,y)$. Horizontal, vertical and diagonal images ($I_{LH}(x,y)$, $I_{HL}(x,y)$ and $I_{HH}(x,y)$) are the detail sub-images of the source image $I(x,y)$. Multiresolution could be obtained by recursively applying the same algorithm to the low-pass coefficients of the previous decomposition [79,80,81].

The reconstruction of the image $I(x,y)$ is obtained from the inverse 2D wavelet transform using the sub-images $I_{LL}(x,y)$, $I_{LH}(x,y)$, $I_{HL}(x,y)$ and $I_{HH}(x,y)$ as shown in Figure 1.14. This involves up-sampling in columns and low-pass ($\tilde{L}$) and high-pass ($\tilde{H}$) filtering for each sub-image, then in rows. The summation of all the resulting matrices would build the image $I(x,y)$ [78].

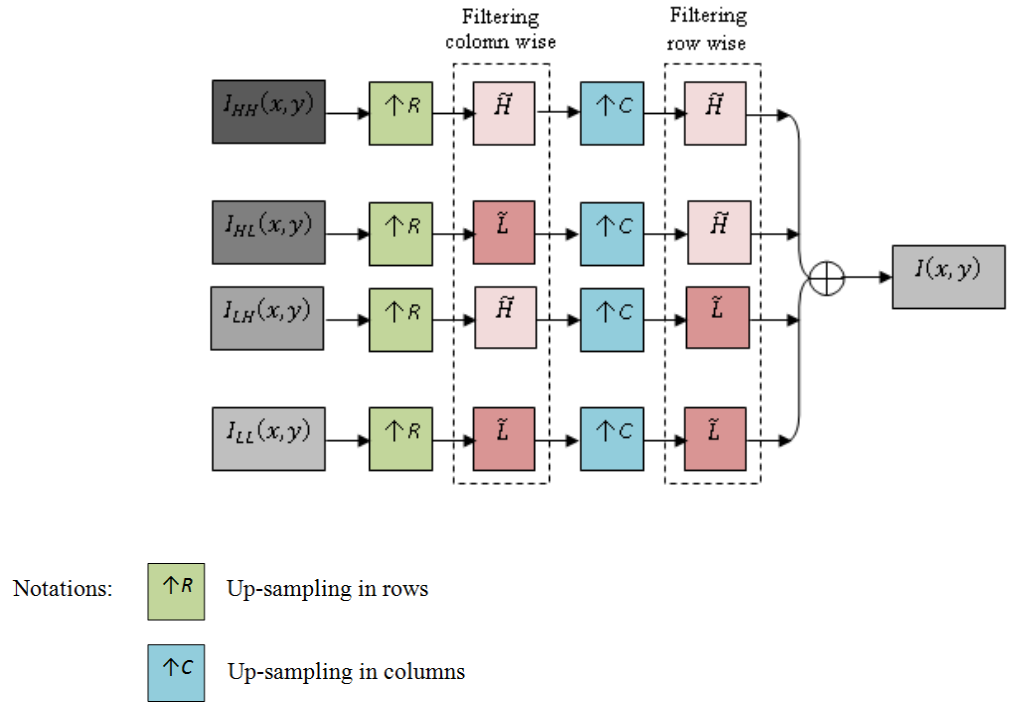

Figure 1.14. One reconstruction level of 2D image.

1.4. 2.1.1. B) DWT pansharpening algorithm

The information flow diagram of wavelet-based image fusion algorithm is shown in Figure 1.15. In wavelet image fusion scheme, the source images are decomposed into approximation and detail coefficients at required level using DWT. The approximation and detail coefficients of both images are combined using a fusion rule. The fused image could be obtained by taking the inverse discrete wavelet transform [78].

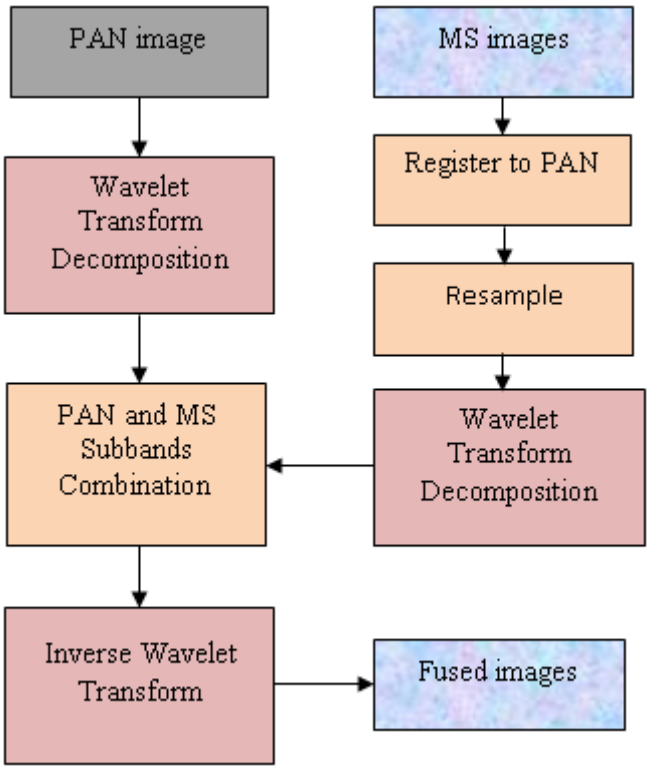

Figure 1.15. Scheme of the Wavelet image fusion.

1.4.2.1.2. "A Trous" Wavelet Transform (ATWT) pansharpening technique

1.4.2.1.2. A) ATWT transform

The "à trous" wavelets are the most flexible than other types of wavelets. Only one non-directional image is produced; this image will have the same dimensions as the original image since no decimation is required. In this type of transform, the approximation image is obtained by filtering the input image by a cubic spline filter "h" [82]. To perform the process of decomposition, the mask "*h*" is filled with zeros and the approximation is filtered by the new mask. The difference between two levels of approximation is called the wavelet plane at that level. This process is represented as follows:

$$p_{j+1} = p_j * h_j \tag{1.23}$$

$$w_{j+1} = p_j - p_{j+1} \tag{1.24}$$

Where initially, p_0 is the original image and w_j and p_j are the wavelet and approximation plane at level j, respectively. "*" is the symbol of convolution.

The reconstructed image can simply be obtained by adding the wavelet planes to the approximation image of the last layer [83].

The mask of "à tous" filter at level j is defined as follow:

$$h_j = \frac{1}{256}\begin{bmatrix} 1 & 4 & 6 & 4 & 1 \\ 4 & 16 & 24 & 16 & 4 \\ 6 & 24 & 36 & 24 & 6 \\ 4 & 16 & 24 & 16 & 4 \\ 1 & 4 & 6 & 4 & 1 \end{bmatrix} \quad (1.25)$$

At each level j, h_j is modified by doubling its size and inserting null values between the original coefficients [4].

1.4. 2.1.2. B) ATWT pansharpening algorithm

In additive ATWT based fusion method, the PAN wavelet planes are added directly to the MS image (equation (1.26)):

$$F = \sum_{j=1}^{n} w_{PANj} + MS \quad (1.26)$$

Where, F is the fused image, n is the number of wavelet planes, w_{PANj} is the wavelet plane of the PAN image at level j, and MS is the multispectral image [83].

1.4.2.1.3. Laplacian Pyramid (LP) pansharpening technique

1.4.2.1.3. A) LP transform

The Laplacian Pyramid was first proposed by [84] for compact image representation. The main steps are as follows:

1. Filtering the original image g_0 with a low pass mask "*w*" (the Gaussian filter, for example) and downsample it by 2 to create a reduced low-pass version g_1.

2. This image is then upsampled and filtered with the same mask "*w*" to create the extended low-pass image g_1'. The detail image L_0 is obtained by calculating the following difference:

$$L_0 = g_0 - g_1' \quad (1.27)$$

The above steps can be performed recursively on the low-pass and subsampled image g_1 a maximum of N times and the image size is 2^Nx2^N. Thus, the end result is a number of

detail images $L_0, L_1, \dots, L_N$ and the lowpass image g_N. Each obtained image recursively is smaller, in size by a factor of 4, than the previous image and its center frequency is reduced by an octave (see Figure 1.16).

The N detail images $L_0, L_1, \dots, L_N$ and the low-pass image g_N are used to obtain the original image g_0 by the inverse transform as follows:

1. g_N is upsampled and filtered with the masque "w" to obtain the image $g_N^{'}$.
2. The approximation image at the next upper level is obtained by adding the image $g_N^{'}$ and the lowest level detail image L_N to obtain:

$$g_{N-1} = L_N - g_N' \tag{1.28}$$

Steps 1 and 2 are repeated on the detail images $L_0, L_1, \dots, L_{N-1}$ to obtain the original image [85].

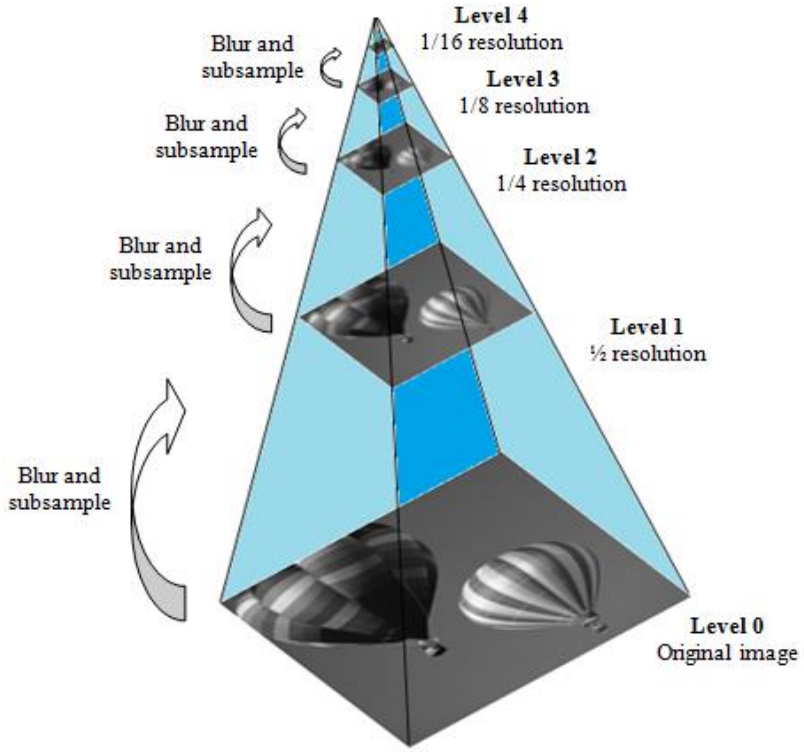

Figure 1.16. Example of an image pyramid with 5 levels.

1.4. 2.1.3. B) LP pansharpening algorithm

The Laplacian Pyramid fusion algorithm consists of calculating Gaussian and Laplacian pyramids of each source image, iteratively, pansharpening the Laplacian images at each pyramid level by selecting the pixel of greatest absolute values, combining the merged

Laplacian pyramid with the extended combined pyramid of the lower level, and extending the combined pyramids at the upper level. The pixel selection step above can also be done using a PCA-based weighted averaging technique [86].

1.4.2.1.4. Additive Wavelet Luminance (AWL) pansharpening method

Many shift-invariant wavelet transform based algorithms have been proposed [82] such as the "à trous" Wavelet transform based additive and substitutive methods. In the additive process, the PAN and MS images are decomposed into wavelet planes and the PAN image planes are directly added to the MS bands. In the substitute method, the MS planes are replaced by PAN image planes. Hybrid methods between IHS/decimated wavelets and IHS/undecimated wavelets have also been introduced to improve fusion performance [67,87].

AWL is an additive and hybrid method between IHS/undecimated wavelet transforms. In the AWL method, firstly, the MS image is transformed into IHS. Then, the histogram of the PAN image is matched with the Intensity (*I*) component of the MS image. The matched PAN image is transformed into wavelet planes. The new *I* is obtained by adding the wavelet planes of the matched PAN image w_{pl} with the original *I* component. Finally, the inverse IHS is applied to the components *H*, *S* and the new *I* [83,87].

$$I_{new} = \sum_{j=1}^{n} w_{pl} + I \qquad (1.29)$$

1.4.2.1.5. High-Pass Filter (HPF) pansharpening method [18]

It should be noted that the various MRA- based methods are only characterized by the way of obtaining the image P_L and the injection weight g. For the P_L, there are several ways; methods which use a single level of decomposition, methods based on multi-level multiresolution analysis algorithms and methods based on a more general MRA framework. Specifically, within the early stage, the HPF methodology is that the representative approach [27]. A high-pass filtering is applied to the PAN image in order to extract the high frequencies, then, these high frequencies are introduced in the MS image by addition, which leads to a synthetic image [88]**.** The mask is a high-pass Laplacian filter of 3 by 3 pixels.

1.4.2.1.6. Smoothing Filter-Based Intensity Modulation (SFIM)

The SFIM fusion method controls the trade-off between spatial and spectral information. Moreover, it suffers more loss in spatial information but it preserves more spectral information. Its effectiveness depends mainly on the design of the filter.

SFIM is a BT-type approach, uses a smooth version of the PAN image P_L, instead of the intensity component of the MS image. This method is defined by:

$$\begin{bmatrix} R_{SFIM} \\ G_{SFIM} \\ B_{SFIM} \end{bmatrix} = \frac{PAN}{P_L} . \begin{bmatrix} R \\ G \\ B \end{bmatrix} \quad (1.30)$$

Where, P_L is often obtained from a 7x7 mean filter. It is known that the spatial resolution can be improved by increasing the mask size of the low-pass filter in the SFIM method [37,57].

1.4.2.2. Examples of pansharpening of some (MRA)-based methods

Figures 1.17 and 1.18 show the application of different pansharpening (MRA)-based methods with the same precedent data of figures 1.10.(a) and (b) and 1.11.(a) and (b), respectively.

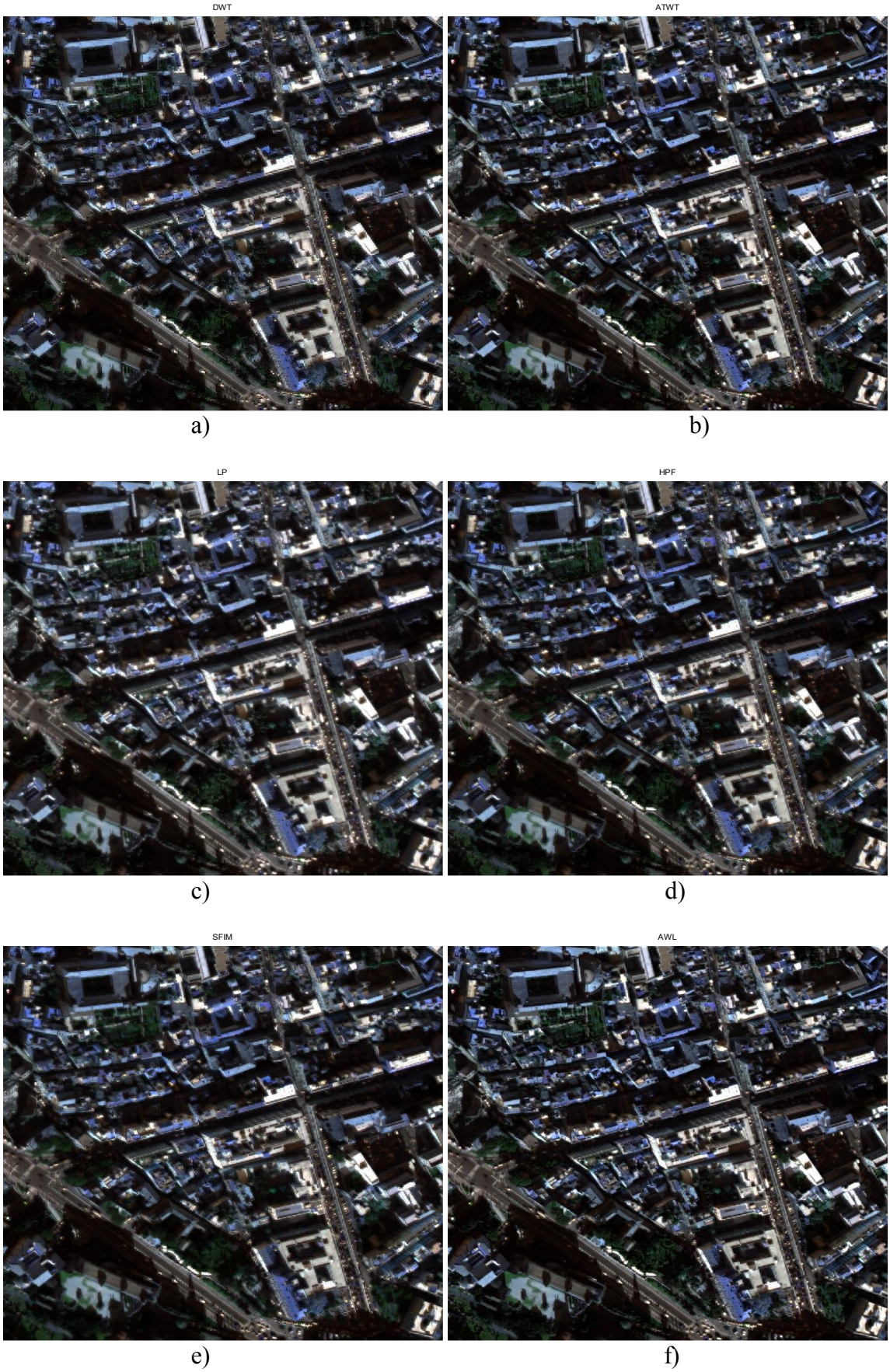

Figure 1.17. Pansharpening an urban scene. a) DWT fused image. b) ATWT fused image. c) LP fused image. d) HPF fused image. e) SFIM fused image. f) AWL fused image.

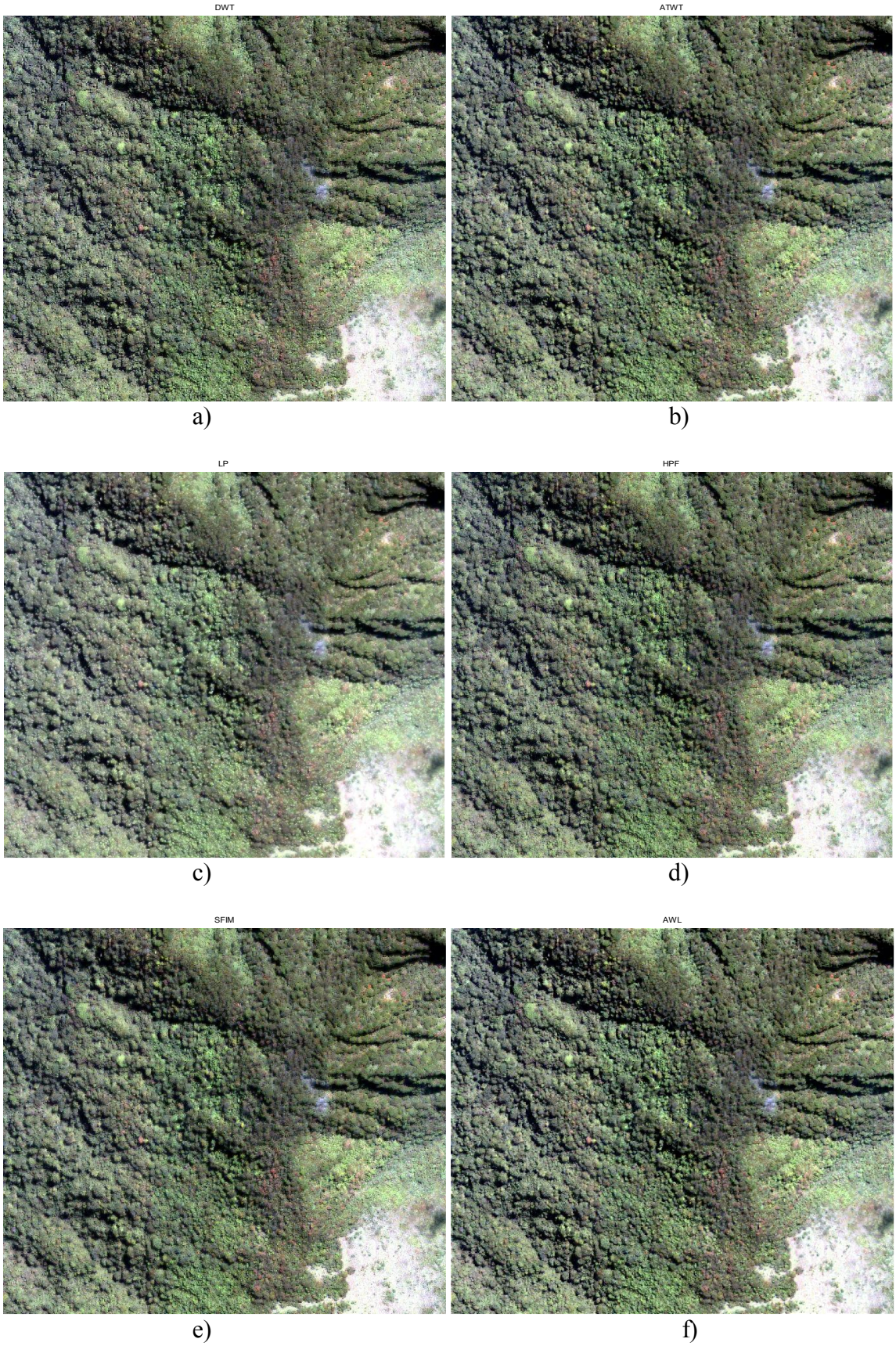

Figure 1.18. Pansharpening a vegetation scene. a) DWT fused image. b) ATWT fused image. c) LP fused image. d) HPF fused image. e) SFIM fused image. f) AWL fused image.

1.4.2.3. Visual Analysis

Considering the techniques belonging to the MRA-based methods, which benefit from proper detail extraction, in particular, the match of the low-pass filter with the sensor MTF which allows significantly reducing the classical blur of the MRA final products.

The best visualization is given by the decimated approaches in the LP method, especially for urban areas, due to greater aliasing robustness compared to the ATWT. The resulted image using the ATWT method has good color information, which leads to good preservation of spectral information. However, the fused image suffers from vital spatial distortions. The DWT method is much slower to compute and the fused image often has lower visual quality than images produced by other methods. It can be seen that the fused image of the HPF gets good spectral quality, but it is a bit too accentuated on the vegetation areas due to poor detail injection. The SFIM method offers the best color preserving but suffers more spatial detail loss in the fused image. The AWL method greatly improves the spatial qualities of the original MS images and is most visible in vegetation areas.

However, the similarity of the frequency response of the filters in the MRA approaches with that of the MS-MTF sensor, explains the good performances. The application of the filter leads to poorer performance. This is mainly due to the spatial artifacts due to the presence of ripples in the pass-band in the representation of this filter in the frequency domain and to its greater dissimilarity with respect to the transfer function of the sensor.

1.4.3. Variational optimization (VO)-based methods

The VO-based methods are an interesting category of the pansharpening family. The major process of this category is generally based on the optimization of a variational model. The VO-based methods consist of two main parts; building functional energy and optimization solution. Figure 1.19 shows the schematic of the VO-based pansharpening strategies.

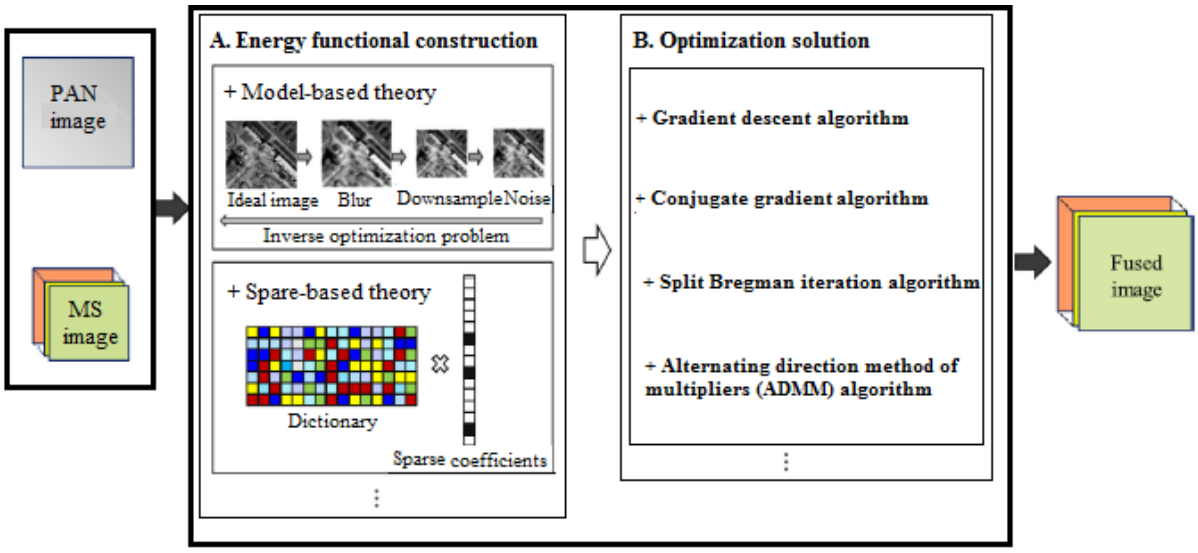

Figure 1.19. Flowchart of the VO-based pansharpening methods.

The methods based on observation model [89] – [95] and the sparse representation [22], [96] – [98] are the most popular for the construction of the functional energy. Functional energy can be represented by three models; the spectral fidelity, the spatial enhancement and the a priori models. Generally, it can be represented by the following expression:

$$E(x) = f_{spectral}(x, MS) + f_{spatial}(x, PAN) + f_{prior}(x) \qquad (1.31)$$

Where, x denotes the ideal fused image which is divided on three terms. The first is the spectral fidelity model, the second is the spatial enhancement model, and the third is the prior model. The spectral fidelity model relates the ideal fused image to the MS image and it is generally constructed on the assumption that the observed MS image can be obtained by blurring, downsampling and noising operations performed on the MS image [10,95,99,100,101]. The spatial enhancement model is generally built on two assumptions; the first is the spectral degradation between the MS image and the PAN image, i.e., the PAN band is assumed to be a linear combination of the MS bands [95,100,102]. The second is the spatial structures of the fused image, which are approximately consistent with the PAN image [11,90,103,104]. This is generally represented by gradient features [90,103,105], wavelet coefficients [11], or other approaches [92,106]. Some VO-based pansharpening methods are based on the Laplacian prior model [107], the Huber-Markov prior model [95], the total variation (TV) prior model [94], the nonlocal prior model [108] and the low-rank prior model

[109], etc. A certain number of fusion energy functions can be generally simplified as the following two basic expressions:

$$E(x) = \lambda_1 \|MS - DSx\| + \|PAN - Cx\| + \lambda_2 prior(x) \quad (1.32)$$

$$E(x) = \lambda_1 \|MS - DSx\| + \sum_{b=1}^{B} \|W^* PAN - W^* x_b\| + \lambda_2 prior(x) \quad (1.33)$$

Where, D and S denote the downsampling and blurring matrix, respectively, the C denotes the spectral combination matrix, and the W represents the operator to extract the high spatial structure information. λ_1 and λ_2 are two parameters of the model to balance the three terms. It can be seen that an obvious characteristic of the two representative energy functions in (1.32) and (1.33) depends on the two classical assumptions of the spatial enhancement models.

Furthermore, the two hypotheses are strongly correlated with the basic idea of extracting the spatial structure of the CS-based methods and the MRA-based methods, respectively.

The sparse-based methods are mainly based on sparse representation theory [110]. This is generally represented as: $x = \Psi\alpha$, where the Ψ denotes the dictionary of signals of the remote sensing images, and the α denotes the sparse coefficients. The sparse-based pansharpening strategies were first projected by [22], and since then, they need got speedy development.

We must note that the dictionary acquisition is relatively important for this kind of pansharpening methods.

The optimization solution of the fusion model is generally based on an iterative optimization algorithm [111,112,114], such as the gradient descent algorithm [95,113], the conjugate gradient algorithm [114], the split Bregman iteration algorithm [90], the alternating direction method of multipliers (ADMM) algorithm [101] and the optimization solution based on the Sylvester equation [101,114] etc. On the full, there are three key points within the VO-based pansharpening strategies. The first is the construction of the optimal fusion functional energy, the second is the adaptive selection of model parameters, and the third is the rapid optimal solution. It should be noted that the application of the VO-based pansharpening methods is hampered due to their low efficiency [27].

1.4.3.1. Some VO-based methods

1.4.3.1.1. P+XS pansharpening method

P+XS image fusion model is proposed in [89] for merging the PAN and the MS image, on the assumption that the geometry structure of the PAN image should be contained in the MS image. An extended variational fusion model is presented in [115] for sharpening the hyper-spectral image while preserving its spectral pattern [116].

The P+XS technique is a variational method, which determines the pansharpened image by minimizing its functional energy. The total functional energy minimized by the P+XS model is [11]:

$$E(u_n) = \sum_{n=1}^{4} \gamma_n \int_{\Omega} (|\nabla u_n| + div(\theta).u_n)\, dx + \lambda \int_{\omega} (\sum_{n=1}^{4} \alpha_n u_n - PAN)^2 dx + \mu \sum_{n=1}^{4} \int_{\Omega} \Pi_S\big((k_n * u_n) - MS_n\big)^2 dx \quad (1.34)$$

Where, u_n are the desired high resolution multispectral bands, Ω and ω are the image domains, k_n is a convolution kernel, Π_S a Dirac comb and γ_n, λ, α_n and μ are parameters to weight the different terms. The level sets of an image can be represented by the vector field θ consisting of all unit normal vectors of those level sets and is implemented as: $\theta(x) = \frac{\nabla PAN(x)}{|\nabla PAN(x)|_\epsilon}$ [27].

The P+XS method is more complex and there are several parameters to tune. However, for most of them, their values were left at default. The most important parameters are the weights for each multispectral band in the merged image and the regularization term λ [94].

The P+XS method obtains the edge information of the PAN image using the gradient. The spectral information is obtained by approximating the PAN image as a linear combination of the MS bands [89].

1.4.3.2. Examples of P+XS pansharpening method

Figure 1.20 shows the application of the P+XS pansharpening method with the same precedent data of figures 1.10.(a) and (b), and 1.11.(a) and (b), respectively.

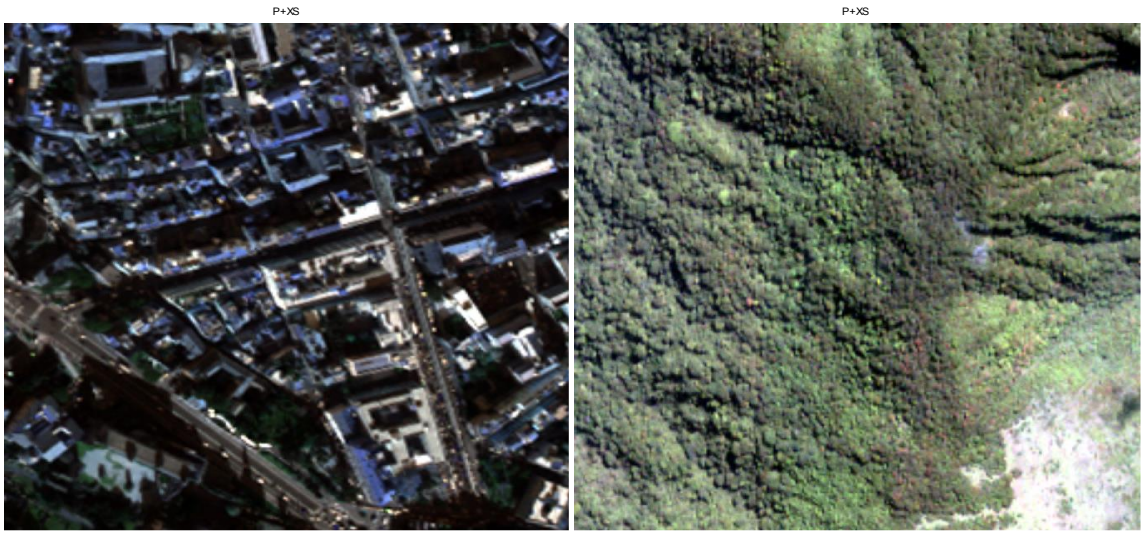

a) b)

Figure 1.20. Pansharpening urban and vegetation scenes, respectively.
a) P+XS fused image. b) P+XS fused image.

1.4.3.3. Visual Analysis

The P+XS pansharpening method is not good, as other methods, in visual spatial quality. Its fusion results look more blurred. It demands more development, mostly, in the injection of spatial details. The P+XS method is more complex and there are several parameters to tune. Because of this, it demands a huge computing time.

1.5. Conclusion

The fusion methods mentioned in this chapter only constitute an inventory not exhaustive of commonly used processes.

This chapter has presented the problem of pansharpening of multi-spectral satellite images and a comprehensive review of the pansharpening methods for remote sensing images based on the three main categories, such as, the CS-based methods, the MRA-based methods, and the VO-based methods.

In any pansharpening technique, the resulting image ought to have high visual quality to help within the detection and classification tasks.

However, the fused image should contain the same colors (spectral information) as the original MS. This becomes especially important as the number of bands increases, because the spectral signature can be used for material identification. Therefore, the pansharpened image should possess both high spatial and spectral qualities.

A visual comparison, using all methods is shown in Figures 1.10, 1.11, 1.17, 1.18 and 1.20, can be made by careful observation of these images and it can be easily found that all of the fused images are visually enhanced over the resampled MS image.

The hybrid result is better than other methods while maintaining color information similar to the original MS image.

In the case of other fusion results, some color distortion has occurred. In addition, in some features, such as building edges and moving cars, some blurring has occurred. These visual results show that hybrid pansharpening can considerably improve the spatial quality while preserving the spectral information of the original MS image.

The spatial quality can be judged visually, but in this way, subtle color changes are harder to notice. Therefore, we look at performance metrics to assess spectral quality. Since high resolution ground truth was not available, we will compare the fusion results with an upsampled version of the original MS data.

Chapter 2: Performance evaluation and comparative study of some fusion methods

2.1. Introduction.

2.2. Qualitative and quantitative evaluation.

2.3. Experimental study.

2.4. Discussions and conclusions.

2.1. Introduction

Each method, discussed in chapter 1, experiences a trade-off between the quality of the spectral and spatial resolutions [4].

For a qualitative evaluation, all these methods gave good results. The spatial quality is enhanced compared to the relative MS images [4].

There are many ways to analyze the results of fused images and compare different pansharpening methods. When comparing methods, we are interested in spectral and spatial quality.

To judge spatial quality, it is much easy to see the acuity of the edges. But when evaluating the spectral quality, it is much more difficult to match the colors of the resulting image to the original multispectral image by visual inspection.

Qualitative evaluation may be used to evaluate the pansharpened images. In addition to the visual analysis, quantitative evaluation must be considered.

There are many image quality metrics that analyze spectral quality. They can be also used to compare pansharpening algorithms [55].

It should be noted that due to the lack of reference images in the real experiments, the quantitative evaluation was comprehensively performed from two aspects. First, the MS image was applied as the reference image for the quantitative evaluation. Second, the fused results were evaluated based on non-reference quality evaluation indices [4,120].

In this chapter, quality assessment is discussed, where qualitative and quantitative evaluations are analyzed in section 2.2. The quantitative indices are classified using a reference image or without a reference image. In section 2.3, experimental results are measured to compare the different pansharpening methods presented in Chapter 1.

2.2. Qualitative and quantitative evaluation

Qualitative or visual analysis is performed by human observers' experiences, which will introduce some uncertainty [55]. In the qualitative evaluation, the resulting images are compared with the colors of the MS images and also to the spatial details of the PAN images.

Most of the pansharpening methods have good spatial details. However, they show visually a little spectral distortion [4].

Since visual analysis can be influenced by personal preferences, quantitative evaluation of pansharpening algorithms is an effective method to assess the quality of the resulting images.

2.2.1. Quantitative evaluation with reference image

When the reference image is available, we can use several different metrics. An evaluation of the performance of the image fusion algorithms can be performed using the metrics presented in Table 2.1.

Name of the Metric	Formula	Features and Properties	Reference value
Correlation Coefficient [122]	$CC = \frac{\sum_{i=1}^{M}\sum_{j=1}^{N}[(F_{i,j}-\mu_F).(R_{i,j}-\mu_R)]}{\sqrt{\sum_{i=1}^{M}\sum_{j=1}^{N}(F_{i,j}-\mu_F)^2.\sum_{i=1}^{M}\sum_{j=1}^{N}(R_{i,j}-\mu_r)^2}}$ Where $F_{i,j}$ and $R_{i,j}$: Value of the pixel (i, j) of the merged image F and of the reference image R, respectively. μ_F and μ_R: Means of the fused image F and the reference image R, respectively. MxN: Reference image size.	The average of the absolute values of the change in correlation coefficients between bands before and after the sharpening process.	0
Correlation [78]	$CORR = \frac{2C_{FR}}{C_F + C_R}$ Where $C_F = \sum_{i=1}^{M}\sum_{j=1}^{N}{F_{i,j}}^2$, $C_R = \sum_{i=1}^{M}\sum_{j=1}^{N}{R_{i,j}}^2$ and $C_{FR} = \sum_{i=1}^{M}\sum_{j=1}^{N}F_{i,j}.R_{i,j}$	Shows the correlation between the reference and fused images.	1
Universal Image Quality Index [123,124]	$UIQI = \frac{\sigma_{FR}}{\sigma_F\sigma_R}.\frac{2\mu_F\mu_R}{{\mu_F}^2+{\mu_R}^2}.\frac{2\sigma_F\sigma_R}{{\sigma_F}^2+{\sigma_R}^2}$ Where σ_F and σ_R: Standard deviations of the merged image F and the reference image R, respectively. σ_{FR} : Covariance between the fused image F and the reference image R.	It models three different distortion factors: luminance distortion, contrast distortion and loss of correlation. So, it measures the structure distortion degree.	1
Root Mean Squared Error [122]	$RMSE = \sqrt{\frac{1}{M.N}\sum_{i=1}^{M}\sum_{j=1}^{N}(F_{i,j}-R_{i,j})^2}$	It is the average squared difference between the original multispectral and fused images.	0

Relative Average Spectral Error [75]	$RASE = \frac{100}{\mu(R)}\sqrt{\frac{1}{n}\sum_{i=1}^{n} RMSE_i^2}$ Where $RMSE_i$: The RMSE value of the ith band. $\mu(R)$: The mean value of the reference image R.	Calculates the mean error of all bands per radiance of the image.	0
Spectral Angle Mapper [125]	$SAM = arccos\left(\frac{\langle u_F, u_R\rangle}{\lvert u_F\rvert . \lvert u_R\rvert}\right)$ Where u_F and u_R: Spectral vectors of the fused image F and the reference image R, respectively.	Calculates the average change in angle of all spectral vectors.	0
Relative Dimensionless Global Error In Synthesis [126]	$ERGAS = 100.\frac{h}{l}\sqrt{\frac{1}{n}\sum_{i=1}^{n}\left(\frac{RMSE_i}{\mu(R_i)}\right)^2}$ Where h/l: The ratio between pixel sizes of the PAN image and the MS image. $\mu(R_i)$: The mean value of the ith band of the reference image R.	Takes the average mean square error normalized by the mean of each band. It measures the spectral distortion.	0
Spectral Information Divergence [127]	$SID(x,y) = D(x\|\|y) + D(y\|\|x)$ Where $D(x\|\|y)$: Relative entropy defined by: $D(x\|\|y) = \sum_{i=1}^{L} p_i log\left({}^{p_i}/_{q_i}\right)$, $p_j = \frac{x_j}{\sum_{i=1}^{n} x_i}$ and $q_j = \frac{y_j}{\sum_{i=1}^{n} y_i}$. $X = (x_1, \dots, x_n)^T$ and $Y = (y_1, \dots, y_n)^T$: Vectors be taken from the MS image and the fused image, respectively.	Visualizes each pixel spectrum as a random variable and thus measure the probability difference between two spectra vectors.	0
Spatial Correlation Coefficient [121]	To extract the high frequency data of a band, it is convoluted with the following high-pass mask: SCC $mask = \begin{bmatrix} -1 & -1 & -1 \\ -1 & 8 & -1 \\ -1 & -1 & -1 \end{bmatrix}$ The SCC value is the average of the CCs for each band of the MS image.	Compares the high frequency data obtained from the panchromatic image with the one extracted from each band of the fused image.	1

Structural Similarity index [78]	$SSIM = \frac{(2\mu_F\mu_R + C_1).(2\sigma_{FR} + C_2)}{(\mu_F{}^2 + \mu_R{}^2 + C_1).(\sigma_F{}^2 + \sigma_R{}^2 + C_2)}$ Where C_1 : A constant that is included to avoid the instability when $\mu_F{}^2 + \mu_R{}^2$ is close to zero. C_2 : A constant that is included to avoid the instability when $\sigma_F{}^2 + \sigma_R{}^2$ is close to zero.	The natural signals of the image would be highly structured and their pixels show strong dependencies. These dependencies would carry vital information about the structures of the objects.	1

Table 2.1. Performance evaluation metrics when reference image is available.

2.2.2. Quantitative evaluation without reference image

When the reference image is not available, the performance metrics shown in Table 2.2 could be used.

Name of the metric	Formula	Features and Properties	Reference value
Spectral distortion [128]	$D_\lambda = \sqrt{\frac{1}{n(n-1)}\sum_{i=1}^{n}\sum_{j=1,j\neq i}^{n}\left\|Q(MS_i, MS_j) - Q(F_i, F_j)\right\|}$ Where $Q(A,B)$: The UIQI value between the image A and image B.	Assesses the spectral distortion.	0
Spatial distortion [128]	$D_s = \sqrt{\frac{1}{n}\sum_{i=1}^{n}\left\|Q(F_i, PAN) - Q(MS_i, P_{LP})\right\|}$ Where P_{LP}: A spatially degraded version of *PAN*.	Assesses the spatial distortion.	0
Quality with No Reference [128]	$QNR = (1 - D_\lambda).(1 - D_s)$	Measures the overall fusion quality without requiring a reference MS image by merging the measurements of the spectral and spatial distortions based on the UIQI index at the full scale of PAN [129].	1

Table 2.2. Performance evaluation metrics when reference image is not available.

2.3. Experimental study

After representing the different metrics in Tables 2.1 and 2.2, we calculated them for all the pansharpening methods presented in Chapter 1 to show the effectiveness of each method. Except the IHS method that can't be used because it contains only 3 bands and the P+XS method because of its modest visual result. Table 2.3 shows the calculation of the correlation between the spectral bands of the reference image and the corresponding bands of the fused image for all pansharpening methods presented in Chapter 1.

The two images are those used in Chapter 1 representing two areas, the first one is an urban image and the second one is a vegetation image.

Test Images	Correlation / Methods	C1	C2	C3	C4
Image 1 (Urban)	PCA	0.9353	0.9421	0.9305	0.9150
	BT	0.9382	0.9457	0.9496	0.9487
	GS	0.9467	0.9437	0.9454	0.9545
	DWT	0.9529	0.9590	0.9658	0.9645
	ATWT	0.9681	0.9684	0.9684	0.9679
	LP	**0.9773**	**0.9807**	**0.9833**	**0.9815**
	HPF	0.9770	0.9771	0.9771	0.9769
	SFIM	0.9725	0.9739	0.9750	0.9772
	AWL	0.9590	0.9629	0.9682	0.9685
Image 2 (Vegetation)	PCA	0.8135	0.7996	0.8283	0.8121
	BT	0.8117	0.7968	0.7880	0.8256
	GS	0.7829	0.7834	0.7908	0.8617
	DWT	0.8532	0.8605	0.8295	0.8665
	ATWT	0.9074	0.9081	0.9057	0.9135
	LP	**0.9304**	**0.9351**	**0.9164**	**0.9431**
	HPF	0.9134	0.9139	0.9126	0.9167
	SFIM	0.9185	0.9175	**0.9164**	0.9138
	AWL	0.9082	0.9131	0.8928	0.9194

Table 2.3. Four-band correlation between reference and merged images for different methods.

The quality assessment metrics, when reference image is available or not, are shown in Tables 2.4 and 2.5, respectively, for different pansharpening methods.

Test Images	Metrics / Methods	CC	ERGAS	RASE	RMSE	SAM	SID	SCC	UIQI	SSIM
		0	0	0	0	0	0	1	1	1
Image 1 (Urban)	PCA	0.2408	11.6578	46.4863	26.2995	6.3342	0.1173	0.9652	0.8030	0.7329
	BT	0.0104	7.5234	30.0312	16.9901	**1.8174 e-007**	**0**	0.9759	0.9453	0.9329
	GS	**0.0023**	7.3762	29.4087	16.6379	3.4284	0.1145	**0.9945**	0.9475	0.9261
	DWT	0.0160	6.6265	26.3275	14.8947	3.8348	0.1373	0.7434	0.9595	0.9682
	ATWT	0.0237	6.3785	25.5305	14.4438	2.6950	0.0928	0.9783	0.9642	0.9606
	LP	0.0350	5.3688	23.8552	13.4960	2.3560	0.0204	0.8366	0.9701	0.9582
	HPF	0.0151	**5.1828**	**20.7446**	**11.7362**	2.0340	0.0866	0.9635	**0.9755**	0.9805
	SFIM	0.0107	5.4640	21.5671	12.2015	0.5083	0.0003	0.9390	0.9732	**0.9814**
	AWL	0.0265	6.8408	27.2759	15.4313	2.8780	0.0893	0.9704	0.9593	0.9522
Image 2 (Vegetation)	PCA	0.1945	7.0812	28.0228	31.4376	2.5419	0.0320	0.9807	0.6935	0.7695
	BT	0.0461	6.9688	27.8603	31.2553	**1.7614 e-007**	**0**	0.9892	0.7995	0.8350
	GS	0.0357	6.9267	27.4166	30.7575	2.6499	0.0297	**0.9973**	0.8020	0.8315
	DWT	0.0552	6.9181	27.2210	30.5381	5.5415	0.0393	0.9255	0.8400	0.8837
	ATWT	0.0493	5.4615	21.7219	24.3688	3.8697	0.0318	0.9933	0.8974	0.9150
	LP	0.0463	**4.9629**	22.3844	25.1120	2.1727	0.0152	0.8282	**0.9201**	0.9069
	HPF	0.0403	5.1100	20.3239	22.8004	2.7765	0.0318	0.9869	0.9069	**0.9497**
	SFIM	**0.0356**	5.0333	**19.9960**	**22.4326**	1.1499	0.0021	0.9661	0.9096	0.9493
	AWL	0.0532	5.5610	22.0400	24.7257	4.4207	0.0323	0.9860	0.8951	0.9019

Table 2.4. Quality metrics, when reference image is available, for different pansharpening methods.

Test Images	Metrics / Methods	d_λ	d_s	QNR
		0	0	1
Image 1 (Urban)	PCA	0.1116	0.2670	0.6511
	BT	**0.0058**	0.0058	**0.9885**
	GS	0.0267	0.0205	0.9533
	DWT	0.0292	0.0057	0.9653
	ATWT	0.0311	0.0274	0.9424
	LP	0.0513	0.0112	0.9380
	HPF	0.0226	0.0106	0.9671
	SFIM	0.0141	**0.0045**	0.9815
	AWL	0.0359	0.0298	0.9354
Image 2 (Vegetation)	PCA	**0.0746**	0.1583	0.7789
	BT	0.0790	0.1127	0.8173
	GS	0.1006	0.1224	0.7894
	DWT	0.1273	0.0771	0.8054
	ATWT	0.1081	0.0962	0.8061
	LP	0.1199	**0.0450**	0.8404
	HPF	0.0984	0.0690	0.8394
	SFIM	0.0937	0.0629	**0.8492**
	AWL	0.1142	0.0960	0.8008

Table 2.5. Quality metrics, when reference image is not available, for different pansharpening methods.

2.4. Discussions and conclusions

All these methods have good results. Since there are many different quality metrics, it is not easy to class the different pansharpening methods by performance.

In Table 2.3, the LP method has the best correlation in urban and vegetation areas although the fused image is visually degraded. The HPF method comes in second place.

In Table 2.4, in urban area, the HPF method has the best results (ERGAS, RASE, RMSE and UIQI), respectively, and the SFIM is the best in vegetation area (CC, RASE and RMSE). It is necessary to note that the BT method has the best SAM and SID and the GS method has the best SCC.

In Table 2.5, the BT and PCA methods have the best quality metric for spectral distortion and the SFIM and LP methods have the best indices for spatial distortion. Best QNR is for BT and SFIM methods.

It is also interesting to note that PCA and DWT methods perform slightly worse in these experiments.

From these results, it can be concluded that all the methods, whether CS-based methods or MRA-based methods, contribute to preserving the edges and improving the performance of the pansharpened images. Each method has advantages and drawbacks.

From a visual, quantitative and computation time comparison, it can be concluded that there are some methods that behave very well with the fusion process, such us the GS, BT, LP, ATWT and SFIM, because of their spectral and spatial qualities.

According to the previous results, it is necessary to seek preferment methods which enable a good compromise between the spatial and spectral qualities. More recent improved methods are presented in Chapter 3.

Chapter 3: Pansharpening with some recent methods

3.1. Introduction.

3.2. Some recent fusion methods.

3.3. Performance evaluation.

3.4. Visual analysis.

3.5. Quantitative analysis.

3.6. Conclusion.

3.1. Introduction

Pansharpening algorithms are improved and a variety of state-of-the-art methods are planned in recent years [27].

Also, there is an interesting phenomenon that CS-based pansharpening methods and MRA-based pansharpening methods show similar statistical results, which is different from the general understanding that CS-based methods tend to bring serious consequences. This is because of the application of the traditional pansharpening scheme of CS-based methods or a particular part of the popular pansharpening algorithms.

3.2. Some recent fusion methods

It should be noted that the CS-based methods have been improved and a number of advanced methods have been proposed. Especially since 2000, CS-based methods have been simplified and generalized in the unifying framework, and various advanced strategies can be applied to improve their performance.

Therefore, the approaching performance of the advanced CS-based methods to the MRA-based methods is intelligible and inspiring [27].

3.2.1. Generalized IHS (GIHS) pansharpening method

GIHS or Fast IHS (FIHS) is a CS-based method, which is a unifying image fusion method in which the inverse transform to the original RGB space is obtained by [32] as follows:

$$\begin{pmatrix} R \\ G \\ B \end{pmatrix} = \begin{pmatrix} 1 & -1/\sqrt{2} & 1/\sqrt{2} \\ 1 & -1/\sqrt{2} & -1/\sqrt{2} \\ 1 & \sqrt{2} & 0 \end{pmatrix} \begin{pmatrix} I \\ v_1 \\ v_2 \end{pmatrix} \tag{3.1}$$

3.2.2. Improved Adaptive IHS (IAIHS) pansharpening method

It is a CS-based method proposed by [40], in which the *I* component is estimated as closely as possible through approximation of the PAN image by resolution the subsequent optimization problem:

$$\min_{\alpha_1,\dots,\alpha_N} \left\| P - \sum_{i=1}^{N} \alpha_i MS_i \right\|^2 \tag{3.2}$$

With, $\alpha_1 \geq 0, \dots, \alpha_N \geq 0$

In addition, in the IAIHS pansharpening method, a new gain is introduced in the injecting procedure, which is structured according to the PAN image and each band of the MS image. The injection gain is calculated as:

$$g_i = \frac{MS_i}{(1/N)\sum_{i=1}^{N} MS_i}\left(\beta w_P + (1-\beta) w_{MS_i}\right) \tag{3.3}$$

Where β is a tradeoff parameter, w_A denotes the edge detecting weighting matrix on image *A:*

$$w_A = exp\left(-\frac{\lambda}{|\nabla A|^4+\varepsilon}\right) \tag{3.4}$$

Where, ∇A is the gradient of the image *A*, λ and ε are the tuning parameters [59].

3.2.3. Additive Wavelet Luminance Proportional (AWLP) pansharpening method

It is a MRA-based method. The method was reported to be the joint winner in the 2006 IEEE Data Fusion Contest [42]. It is a hybrid method which combines the ATWT and IHS transforms. It aims to inject high frequency information in proportion to their original values. This is one way to better preserve the radiometric signature between the bands of the MS image.

It was first proposed (AWL) in [87], and then later extended to images with more than three bands (AWLP) in [67].

The AWLP weight factor is the ratio of the MS bands to the mean value of all MS bands, in the experiments. AWLP method is given using a weighted injection scheme such as [67]:

$$F_i = MS_i + \frac{MS_i}{(1/N)\sum_{i=1}^{N} MS_i}\sum_{j=1}^{n} w_{pl} \tag{3.5}$$

Where, the injection of details to the original MS bands is done proportionally because of the weighting coefficient. The denominator of the weight factor can be interpreted as the intensity component given by the IHS transform [83] and w_{pl} is the wavelet planes of matched PAN image.

3.2.4. Generalised Laplacian Pyramid with Modulation Transfer Function (MTF-GLP) pansharpening method

The downsampling and interpolation operations in MRA-based methods with decimated filters (DWT filter, for example) generally cause spatial aliasing artifacts. However, for

proper operation of MRA-based methods, the filters used are tightly tuned to match the Modulation Transfer Function (MTF) of the sensor [70] – [72], like the MTF-GLP method [27,72].

3.2.5. Band-Dependent Spatial Detail (BDSD) pansharpening method

The BDSD algorithm [36] starts from an extended version of the generic formulation (1.2) of the CS methods class as follows:

$$\widehat{MS}_i = \widetilde{MS}_i + g_i\left(P - \sum_{k=1}^{N} \omega_{i,k}\, \widetilde{MS}_k\right), \quad i = 1, \dots, N \tag{3.6}$$

By defining the coefficients:

$$\gamma_{i,k} = \begin{cases} g_i & \text{if } k = N+1 \\ -g_i.\omega_{i,k} & otherwise \end{cases} \tag{3.7}$$

Equation (1.2) can be rewritten in compact matrix form as:

$$\widehat{MS}_i = \widetilde{MS}_i + H\gamma_i \tag{3.8}$$

In which $H = \left[\widetilde{MS}_1, \dots, \widetilde{MS}_N, P\right]$ and $\gamma_i = \left[\gamma_{i,1}, \dots, \gamma_{i,N+1}\right]^T$ (all the images are organized by columns). The optimal *minimum mean square error* (MMSE) joint estimation of the weights-and-gains vector γ would encompass the use of the unknown target image $\widehat{MS}_i$ and is thus performed at a reduced resolution. Consequently, the solution is found as:

$$\hat{\gamma}_i = (H_d^T H_d)^{-1} H_d^T \left(\widetilde{MS}_i - \widetilde{MS}_i^{\,LP}\right) \tag{3.9}$$

In which H_d is the reduced-resolution version of H, and $\widetilde{MS}_i^{\,LP}$ is a version of $\widetilde{MS}_i$ obtained through a low-pass filter, whose spatial frequency response matches the average *modulation transfer function* (MTF) of the MS sensor [6].

3.2.6. Partial Replacement Adaptive CS (PRACS) pansharpening method

In [45], the concept of *partial replacement* of the intensity component is introduced. In the PRACS method, the PAN image is not directly used instead of the component substitution. The algorithm utilizes a weighted sum of PAN and of the ith MS band ($P^{(i)}$) to calculate the ith sharpened band in (1.2). For this reason, this methodology is spoken as

Partial Replacement Adaptive CS (PRACS). For $i = 1, \dots, N$, the band-dependent high resolution sharpened image is calculated as:

$$P^{(i)} = CC\left(I_L, \widetilde{MS}_i\right).P + \left(1 - CC\left(I_L, \widetilde{MS}_i\right).\widetilde{MS}_i{}'\right) \quad (3.10)$$

In which, $\widetilde{MS}_i{}'$ is the ith MS band histogram-matched to PAN, $CC(X,Y)$ is the correlation coefficient between X and Y, and I_L is given by (1.7), where the weights α_i are obtained through the linear regression of $\widetilde{MS}_i{}'$, $i = 1, \dots, N$, on P_L, i.e., the PAN image spatially degraded to the MS resolution.

The injection gains $\{g_i\}$ are obtained according to:

$$g_i = \beta.CC\left(P_L{}^{(i)}, \widetilde{MS}_i\right)\frac{std(\widetilde{MS}_i)}{\frac{1}{N}\sum_{k=1}^{N} std(\widetilde{MS}_k)}L_i \quad (3.11)$$

According to [45], (3.11) is given by the product of:

1) An empirically tuned parameter β that normalizes the high frequencies, so that they lie in the correct dynamic range.

2) A correlation calculated to minimize the global dissimilarity between each band of the MS image and the low-resolution image $P_L{}^{(i)}$, calculated by low-pass filtering of $P^{(i)}$.

3) A coefficient calculated by standard deviations among the MS bands.

4) An adaptive factor L_i, defined by equation (3.12), aimed at removing the local spectral instability error [6].

$$L_i = 1 - \left|1 - CC\left(I_L, \widetilde{MS}_i\right)\frac{\widetilde{MS}_i}{P_L{}^{(i)}}\right| \quad (3.12)$$

3.2.7. Indusion pansharpening method

It is a MRA-based method. Indusion is a Decimated Wavelet Transform using an *additive* injection model [117,6], based on the induction scaling technique, which profits from multiple equalization steps to improve the performance [118].

3.2.8. Optimal Filter (OF) pansharpening method [119]

It is a MRA-based method. Designing an optimal filter, that is able to extract relevant and non-redundant information from the PAN image, is presented in this method. Statistical

properties of the images are used to obtain the optimal filter coefficients. These coefficients are more consistent with type of remotely sensed images compared with other masques [119].

3.3. Performance evaluation

Figures 3.1 and 3.2 show the results of the application of some recent pansharpening methods using the same set of figures 1.10.(a) and (b) and 1.11.(a) and (b), respectively.

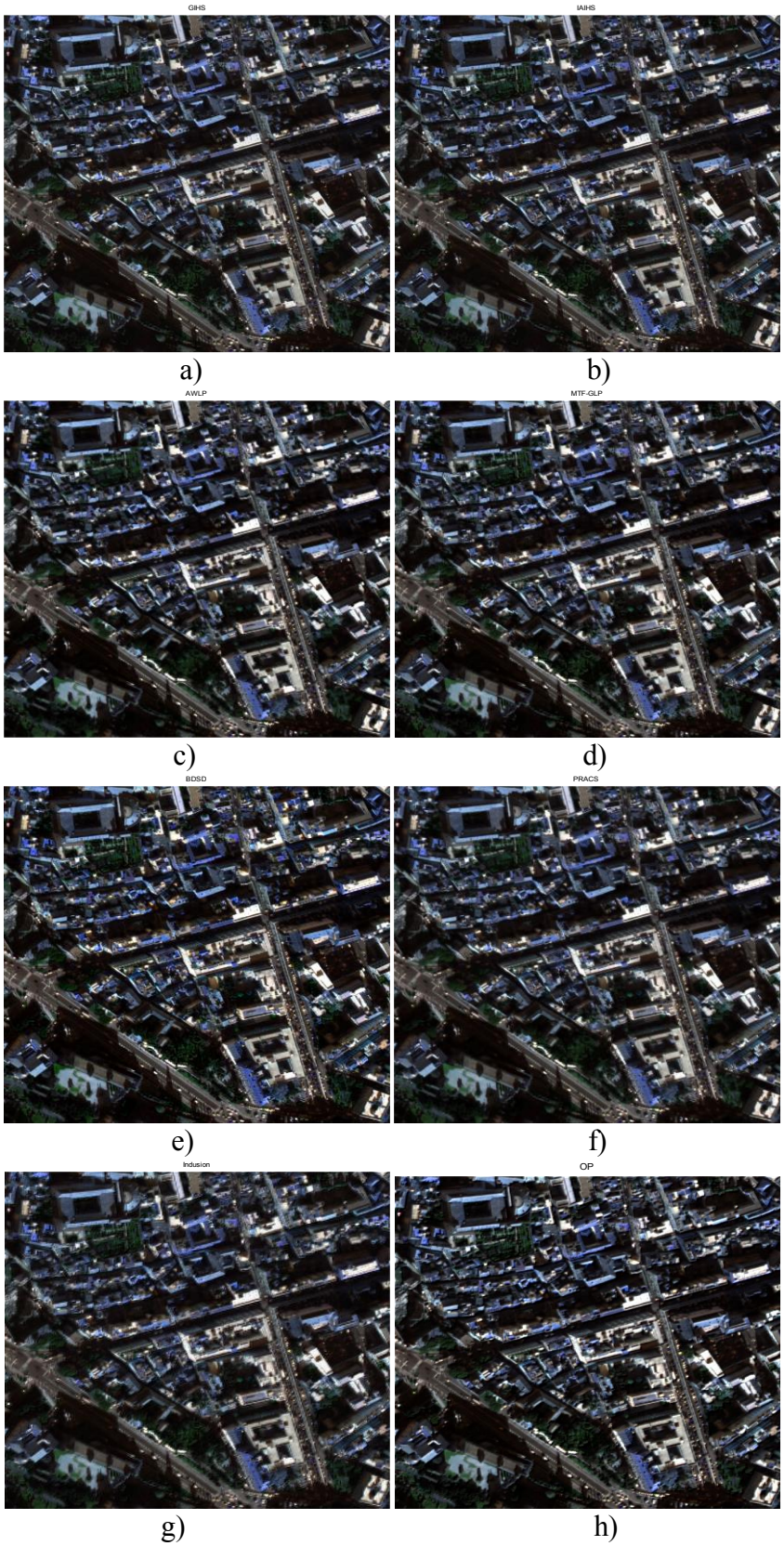

Figure 3.1. Pansharpening an urban scene. a) GIHS fused image. b) AIHS fused image. c) AWLP fused image. d) MTF-GLP fused image. e) BDSD fused image. f) PRACS fused image. g) Indusion fused image. h) OF fused image.

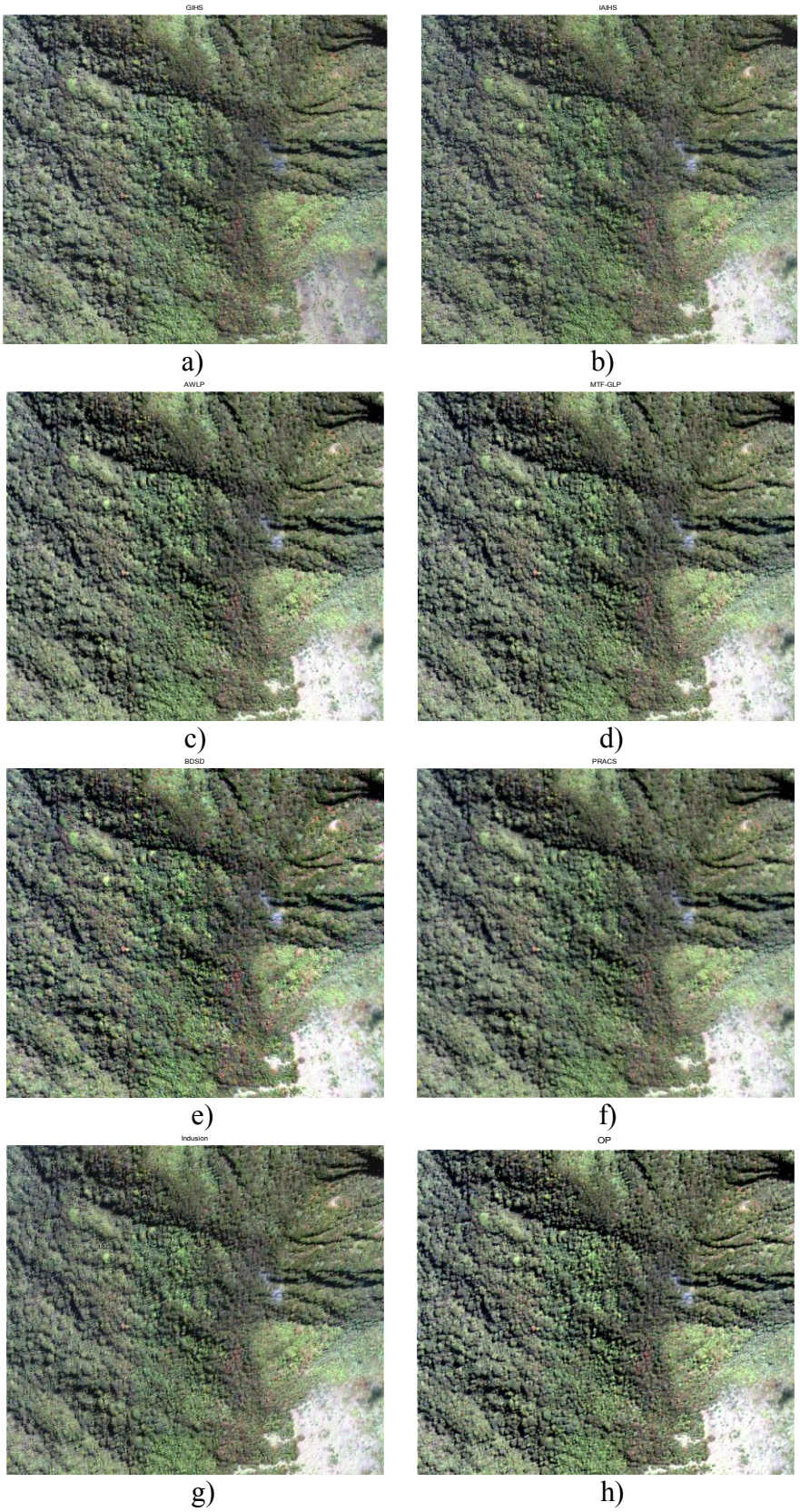

Figure 3.2. Pansharpening a vegetation scene. a) GIHS fused image. b) AIHS fused image. c) AWLP fused image. d) MTF-GLP fused image. e) BDSD fused image. f) PRACS fused image. g) Indusion fused image. h) OF fused image.

3.4. Visual analysis

It is shown that all the state-of-the-art methods present excellent performances relied to detail enhancement. However, OF, AWLP and MTF-GLP methods clearly show a slight spectral distortion. In the AWLP method, colors have been pretty well distributed and the fused image has high spectral quality but the image has been blurred and there are many artifacts perceptible on the trees in the fused images.

The results of the AWLP and IAIHS methods seem slightly too precise, and the spectral distortion is more visible in areas covered with vegetation.

In addition, the IAIHS method can produce an image whose colors are similar to the original and whose objects are clearer than those of the original. The IAIHS fused image suffers from over-injection of details from the PAN image. The spectral distortion caused by IAIHS method is most visible in the areas covered by vegetation and forest.

Severe artifacts are introduced in the case of applying the Indusion method because of the decimation.

The BDSD and PRACS, achieve the best visual appearance of the fused images and a reduced spectral distortion. Indeed, very interesting performances are attained by adaptive CS approaches, namely the BDSD, PRACS and IAIHS, with the reduction of the spectral distortion.

GIHS and AWLP are more adequate than the original ones (IHS and AWL), in particular, on four-band data sets.

By visually comparing them with the original ones, all this methods can greatly improve the spatial qualities of the original MS images.

3.5. Quantitative analysis

After representing a visual comparison, we calculated the different metrics, cited in Chapter 2, for all the pansharpening methods presented in this chapter to show the effectiveness of each method.

Table 3.1 shows the calculation of the correlation between the spectral bands of the reference image and the corresponding bands of the fused image.

The two images are those used in the precedent chapters. The quality assessment metrics, when reference image is available or not, are shown in Tables 3.2 and 3.3, respectively, for different recent pansharpening methods presented in this Chapter.

Test Images	Correlation / Methods	C1	C2	C3	C4
Image 1 Urban	GIHS	0.9372	0.9433	0.9530	0.9548
	IAIHS	0.9371	0.9426	0.9516	0.9533
	AWLP	0.9696	**0.9696**	**0.9660**	0.9633
	MTF-GLP	0.9634	0.9638	0.9637	0.9633
	BDSD	0.9336	0.9346	0.9372	0.9372
	PRACS	**0.9718**	0.9624	0.9588	**0.9726**
	INDUSION	0.9418	0.9422	0.9421	0.9423
	OF	0.9510	0.9521	0.9647	0.9707
Image 2 Vegetation	GIHS	0.7978	0.8111	0.7590	0.8515
	IAIHS	0.8483	0.8548	0.8276	0.8554
	AWLP	0.9187	0.9046	0.9259	0.8817
	MTF-GLP	0.9001	0.9009	0.8982	**0.9067**
	BDSD	0.9164	0.8830	0.8958	0.8707
	PRACS	**0.9494**	**0.9299**	**0.9654**	0.8659
	INDUSION	0.8549	0.8540	0.8556	0.8517
	OF	0.8859	0.8892	0.8795	0.8758

Table 3.1. Four-band correlation between reference and merged images for different methods.

Test Images	Metrics / Methods	CC	ERGAS	RASE	RMSE	SAM	SID	SCC	UIQI	SSIM
		0	0	0	0	0	0	1	1	1
Image 1 Urban	GIHS	0.0027	7.3905	29.3621	16.6115	3.2880	0.1138	**0.9945**	0.9470	0.9259
	IAIHS	**0.0012**	7.4723	29.6872	16.7954	3.4756	0.1136	0.9944	0.9461	0.9224
	AWLP	0.0164	6.5025	26.1780	14.8101	**0.7981**	**0.0860**	0.9614	0.9629	**0.9633**
	MTF-GLP	0.0253	6.8483	27.4548	15.5325	2.9951	0.1269	0.9729	0.9589	0.9513
	BDSD	0.0490	9.4060	37.7759	21.3716	8.1558	0.1326	0.9726	0.9260	0.8998
	PRACS	0.0112	**6.2131**	**24.7444**	**13.9991**	2.7698	0.1029	0.9745	**0.9651**	0.9611
	INDUSION	0.0065	7.8430	31.3922	17.7601	4.0464	0.1425	0.9206	0.9419	0.9312
	OF	0.0190	7.0064	27.6845	15.6624	3.0941	0.1305	0.8345	0.9564	0.9419
Image 2 Vegetation	GIHS	0.0338	6.9361	27.3687	30.7037	**2.5784**	0.0298	**0.9974**	0.8019	0.8315
	IAIHS	**0.0046**	6.2461	24.6406	27.6432	2.8345	0.0334	0.9958	0.8461	0.8427
	AWLP	0.0415	5.4701	22.2863	25.0020	2.6146	0.0384	0.9858	0.8955	0.9172
	MTF-GLP	0.0519	5.7130	22.7481	25.5201	4.1433	0.0358	0.9929	0.8888	0.8940
	BDSD	0.1187	11.0602	44.1266	50.8497	7.9421	0.1462	0.6931	0.8634	0.8138
	PRACS	0.0171	**4.4989**	**18.8940**	**21.1964**	2.7098	**0.0105**	0.9781	**0.9225**	**0.9266**
	INDUSION	0.0159	6.1595	24.4983	27.4835	3.1009	0.0381	0.9789	0.8530	0.8806
	OF	0.0514	6.1420	24.5657	27.5592	3.9843	0.0373	0.8897	0.8703	0.8954

Table 3.2. Quality metrics, when reference image is available, for different pansharpening methods.

Test Images	Metrics / Methods	d_λ	d_s	QNR
		0	0	1
Image 1 Urban	GIHS	0.0285	0.0215	0.9506
	IAIHS	0.0307	0.0160	0.9538
	AWLP	0.0202	0.0181	0.9622
	MTF-GLP	0.0339	0.0269	0.9402
	BDSD	0.0368	**0.0145**	0.9492
	PRACS	**0.0154**	0.0175	**0.9673**
	INDUSION	0.0272	0.0528	0.9215
	OF	0.0279	0.0152	0.9574
Image 2 Vegetation	GIHS	0.1021	0.1226	0.7878
	IAIHS	0.0908	0.0580	0.8565
	AWLP	0.0880	0.0868	0.8329
	MTF-GLP	0.1113	0.1021	0.7980
	BDSD	0.1012	0.0829	0.8242
	PRACS	**0.0457**	0.0486	**0.9079**
	INDUSION	0.0950	0.0287	0.8790
	OF	0.1136	**0.0254**	0.8639

Table 3.3. Quality metrics, when reference image is not available, for different pansharpening methods.

All these methods have good results. In Table 3.1, the AWLP and PRACS methods have the best correlation in urban area. The PRACS and MTF-GLP methods have the best correlation in vegetation area.

In Table 3.2, in urban and vegetation areas, the PRACS method has the best results (ERGAS, RASE, RMSE and UIQI) followed by the AWLP method. The GIHS method has the best SCC and the IAIHS method has the best CC.

In Table 3.3, the PRACS method has the best quality metric for spectral distortion and QNR. The BDSD and OF methods have the best indices for spatial distortion. The BDSD, INDUSION and OF methods perform slightly worse in these experiments. Each method has advantages and disadvantages.

From a visual, quantitative and computation time comparison, it can be concluded that there are some methods that behave very well, compared to others, with the fusion process, such us the AWLP, GIHS, IAIHS and PRACS methods, because of their spectral and spatial qualities.

The PRACS method presents a little spatial distortion despite its good quantitative results. The IHS-based methods (GIHS, IAIHS and AWLP) show excellent visual results despite their modest quantitative results. For this reason, we have to develop a hybrid method

like the AWLP based on the IHS transform which gives a good compromise between the spatial and spectral qualities.

3.6. Conclusion

In this chapter, some state-of-the-art of pansharpening methods has been presented based on articles ever published between 2000 and 2014. We have presented the formulas and properties based on CS and MRA-based algorithms. Eight pansharpening algorithms were applied. Each method contributes on either side to improve the fusion products. Quantitative and qualitative comparison was necessary made to show the effectiveness of each method.

The visual comparison showed that all of the fused images are visually enhanced over the resampled MS image. A quantitative comparison showed that all these methods have good results.

The PRACS method, IHS-based and MRA-based methods were presented the best results but they all lack the right compromise between quantitative and qualitative qualities.

Wavelet transformation may be a representative technique to extract high-frequency information from panchromatic images. For this reason, its application is preferred in the field of fusion. An effective pansharpening algorithm should be selected for optimal utilization of satellite imagery.

In the next chapter, we will propose a new fusion scheme based on a hybrid method of fusion between the IHS and wavelet transforms to take advantage of the good characteristics of the two transforms which aims to improve the visual and quantitative qualities of high resolution satellite imagery.

Table 3.4 resumes the pansharpening methods used in the precedent experiments with some basic meaning and parameter settings.

Methods and years	Basic meaning and parameter settings
GIHS [32] (2004)	A generalization of the traditional IHS pansharpening method [50] – [52] (2001) for fusion of more than three MS bands.
Brovey [56] (2000)	A CS-based method under the general understanding. It has been marketed in professional software, such as ENVI.
PCA [29] (2004)	A typical CS-based method based on the PCA transformation. It has been marketed in professional software, such as ENVI.
BDSD [36] (2008)	A data-dependent self-adaptive CS-based approach, featured by two advantages: 1) optimal solution of the spatial detail extraction and injection based on minimum mean-square-error; 2) parameter estimation based on local regions.
GS [42] (2000)	A typical CS-based method based on the Gram-Schmidt transformation. It has been marketed in professional software, such as ENVI.
PRACS [45] (2011)	A CS-based method based on partial replacement of the intensity component. The PAN image is simulated by the weighted average of the MS and PAN bands, in the place of using the original PAN image to replace the intensity component directly.
IAIHS [40] (2010)	An improved adaptive IHS. A new injection gain, the injection procedure is structured according to the PAN image and the bands of the MS image.
DWT [61] (1995)	A typical MRA-based method. In the experiments, the default level of decomposition is 2 and the wavelet used was that of Haar.
LP [86] (2000)	A typical MRA-based method. In the experiments, the default level of decomposition is 2, the coefficient selection high-pass is 4 and the coefficient selection base image is 1.
AWL [87] (1999)	A typical MRA-based method. In the experiments, the number of wavelet planes is 2.
HPF [18] (1991)	A typical MRA-based method. In the experiments, the default parameter with 5×5 box filter was used.
SFIM [37, 57] (2000)	An improvement of the HPF method based on a High-Pass-Modulation (HPM) spatial detail injection scheme, which is calculated by the ratio of the resampled MS image and the low pass version of the PAN image.
Indusion [117] (2008)	The “Indusion” = “Induction” + “Fusion”. It is a pansharpening method consists of the induction scaling technique, which improves the performance by several equalization steps.
MTF-GLP [72] (2006)	A popular MRA-based method based on GLP with MTF filter, the unitary detail injection model is applied.
ATWT [82] (1999)	A MRA-based method based on the additive “à trous” wavelet transform with unit injection model.
AWLP [67] (2005)	A generalization of the AWL pansharpening method [85] in terms of a proportional spatial detail injection weight, relying on the original MS band radiance proportionality.
OF [119] (2014)	A typical MRA-based method. The coefficients of the optimal filter are calculated using the statistical properties of the images.
P+XS [89] (2006)	A typical VO-based method. In the experiments, the default parameters are: magnitude=4; alpha(1)=0.3/3; alpha(2)=0.75/3; alpha(3)=0.25/3; alpha(4)=1.7/3; gamma(i)=1; lambda=0.5; mue=3 ; iterations=80 ; deltat=0.01; epsilon=0.0005 and deviation=5.

Table 3.4. Pansharpening methods in the experiments.

Chapter 4: Proposed fusion method

4.1. Introduction.

4.2. Proposal of a fusion algorithm based on IHS and ATWT.

4.3. Experimental results.

4.4. Conclusion.

4.1. Introduction

This chapter is devoted to the proposal of a combination between the IHS and the ATWT methods by introducing a new approximation of the coefficients of the multispectral bands MS. In the first section of this chapter, we present our algorithm including definitions and mathematical formulas. In the second section, we present the results of applying the proposed algorithm. A comparative study between the proposed method and some recent image fusion methods was carried out, followed by an interpretation of the results. The evaluation was made qualitatively and quantitatively. We finished this chapter by some discussions and conclusions.

4.2. Proposal of a fusion algorithm based on IHS and ATWT

The main objective of the combination of classical IHS and ATWT methods is to improve spatial resolution by injecting more spatial information while ensuring better color preservation.

The proposed fusion algorithm is illustrated in Figure 4.1. It can be executed by performing the following steps:

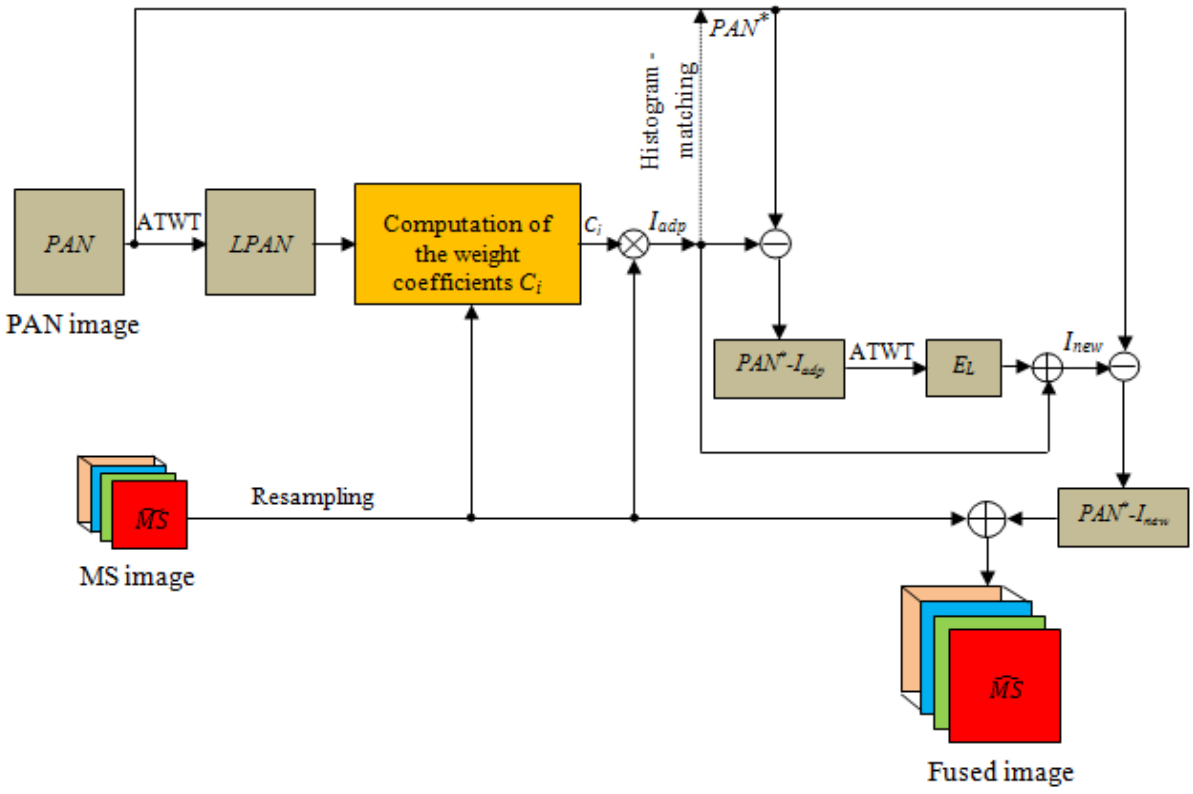

Figure 4.1. Flowchart of the proposed algorithm [4].

Step 1: Low resolution PAN image extraction (LPAN)

To get the best approximation, MS and LPAN should have the same spatial resolution. By using the multiresolution analysis associated with the ATWT, we can estimate the acquisition of the low resolution panchromatic sensor, which does not exist on the satellite.

The LPAN image at level j is obtained by the following equation, using equations (1.23) and (1.25):

$$\mathrm{LPAN}_j = \mathrm{LPAN}_{j-1} * h_j \tag{4.1}$$

Where, initially, LPAN_0 is the PAN image.

Step 2: Determination of the adapted intensity image (I_{adp})

In fact, in most cases the similarity between each MS and LPAN image is rarely too low or zero, so we conclude that the intensity image is equal to the LPAN image.

The intensity image can be calculated by using the following equation:

$$LPAN \cong I = \sum_{i=1}^{n} C_i . MS_i \tag{4.2}$$

Where C_i is the weight coefficient of the *ith* band of the MS image with:

$$\sum_i C_i \leq 1 \tag{4.3}$$

In this work, C_i is based on the energy coefficient and the similarity coefficient between MS and LPAN images.

The PAN image sensor spectrum covers the majority of the MS sensor spectra. Therefore, the radiation detected by the MS sensors is the same as that detected by the PAN sensor, so that the MS image which contains high energy contributes significantly to the construction of the PAN image, and that is the opposite which is true.

The ratio of the average energies (ratio of the average energy MS_i to the average energy LPAN) is given by:

$$RE_i = \frac{EMS_i}{ELPAN} \tag{4.4}$$

Where EMS_i and $ELPAN$ are the mean energies of the images MS_i and $LPAN$, respectively.

The energy coefficient CE_i of the band MS_i is calculated by:

$$CE_i = \frac{RE_i}{\sum_{i=1}^{n} RE_i} \quad (4.5)$$

These coefficients are effective in forming the intensity image in the case where the MS_i images are individually correlated to the LPAN image.

In this case, the intensity image I is given by the following equation:

$$I = \sum_{i=1}^{n} CE_i . MS_i \quad (4.6)$$

To calculate the new MS band coefficients, we propose to also use the similarity coefficient between the *ith* band of the MS image and the LPAN image CS_i as follows:

$$CS_i = \begin{cases} CC(LPAN, \mathrm{MS_i}) & if \quad CC(LPAN, \mathrm{MS_i}) > 0 \\ 0 & if \quad CC(LPAN, \mathrm{MS_i}) \leq 0 \end{cases} \quad (4.7)$$

Where $CC(LPAN, \mathrm{MS_i})$ is the correlation coefficient between LPAN and MS_i images and it is defined by the following equation:

$$CC(LPAN, \mathrm{MS_i}) = \frac{\sum (LPAN - mean(LPAN))(\mathrm{MS_i} - mean(\mathrm{MS_i}))}{\sqrt{\sum (LPAN - mean(LPAN))^2 \sum (\mathrm{MS_i} - mean(\mathrm{MS_i}))^2}} \quad (4.8)$$

The new proposed coefficients of the MS bands are calculated as follows:

$$C_i = CE_i . CS_i \quad (4.9)$$

Where CE_i is the energy coefficient of the MS_i band and CS_i is the correlation coefficient between the *ith* band of the MS image and the LPAN image.

This brings us to a new adapted intensity component I_{adp}:

$$I_{adp} = \sum_{i=1}^{n} C_i . MS_i \quad (4.10)$$

If there is a similarity between the images MS_i and LPAN, the correlation coefficient will be 1. In this case, the image MS_i multiplied by the energy coefficient CE_i is fully injected for the creation of the intensity component I_{adp}.

For lower values of the correlation coefficients, the value of the coefficient C_i of the MS bands will decrease in order to minimize the influence of the diversity which produces spectral distortions in the fused images.

Step 3: Calculation of the error image (E_L)

In the third step, we make a correction to improve the quality of the fused images. The use of multiresolution analysis in the extraction of LPAN image and the proposed MS band coefficients do not give ideal fusion results, as the fusion process is based on the special case of equation (4.2) with an intensity adaptation given by equation (4.10). For this reason, we propose a simple solution, in order to reduce the error between the PAN and the I_{adp} images, given by the following equations:

$$E = PAN^* - I_{adp} \tag{4.11}$$

$$E_L = E * h_j \tag{4.12}$$

Where, E is the error image that contains low and high resolution details, PAN^* is the histogram-matched PAN image, I_{adp} is the adapted intensity image, E_L is the low resolution error image and h_j is the mask of the "à tous" filter at level j.

Step 4: Calculation of the new intensity image (I_{new})

In this step, the new intensity image is obtained by using the following equation:

$$I_{new} = I_{adp} + E_L \tag{4.13}$$

Step 5: Obtaining of the fused image

Finally, the pansharpened image of our algorithm is given by:

$$\widehat{MS} = \widetilde{MS} + (PAN^* - I_{new}) \tag{4.14}$$

Where, $\widehat{MS}$ is the fused image and $\widetilde{MS}$ is the resampled MS image.

The resampled MS image can be obtained by bilinear or bi-cubic filters.

Equation (4.14) is equivalent to the equation used for the computation of the fused image in the Additive Wavelet Luminance method (AWL) [87] except that the high frequency detail image is different. Thus, our main contribution in this step is an improvement of the AWL method with a new intensity image I_{new}.

4.3. Experimental results

In this part, the parameter settings of the proposed method are analyzed and compared with a state-of-the-art of some pansharpening methods. In the fusion experiments, a number of different remote sensing satellites including the Deimos-2, Worldview-2 and Worldview-3 images were employed experimentally.

The satellite Deimos-2 provides PAN images of 1 meter spatial resolution and 4 bands (Near-Infra-Red, Red, Green and Blue) at a spatial resolution of 4 meters.

The resolution of the PAN and MS images of WorldView-2 satellite has 0.5m and 2m, respectively. That of WorldView-3 satellite has 31cm and 1.24m, respectively.

A set of data, acquired on May 30, 2015 by the Deimos-2 satellite which covers different areas of British Columbia (Canada), is used to evaluate the proposed approach. PAN images are 1312 x 864 pixels in size and MS images are 1/4 (328 x 216 pixels). Figures 4.2, 4.3 and 4.4 represent these data sets.

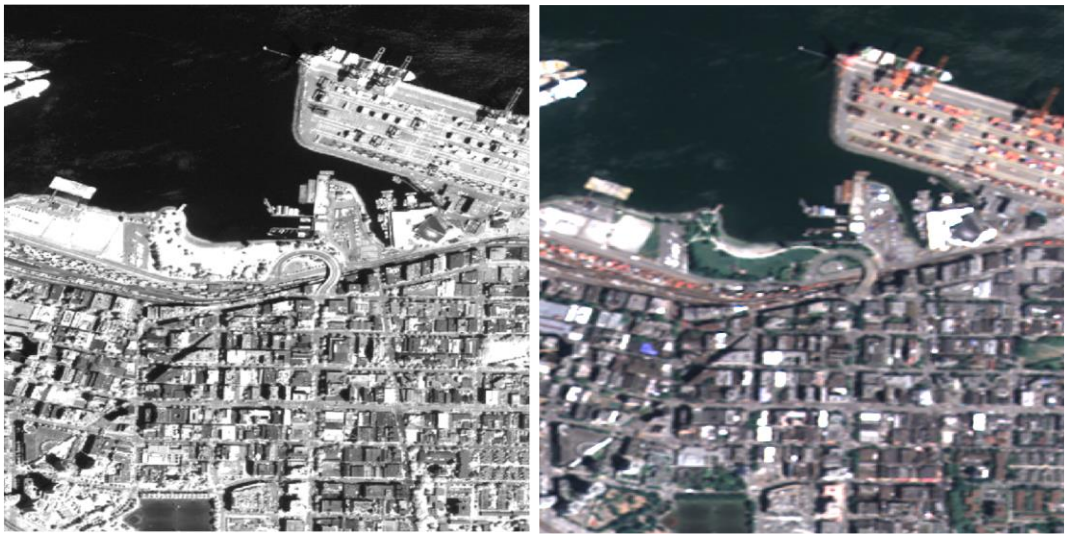

(a) PAN image. (b) Up-sampled MS image.

Figure 4.2. Deimos-2 image (image 1). (a) PAN image. (b) Up-sampled MS image.

(a) PAN image. (b) Up-sampled MS image.

Figure 4.3. Deimos-2 image (image 2). (a) PAN image. (b) Up-sampled MS image.

(a) PAN image. (b) Up-sampled MS image.

Figure 4.4. Deimos-2 image (image 3). (a) PAN image. (b) Up-sampled MS image.

4.3.1. Experimental results of the proposed approach

The up-sampled MS images are obtained by bilinear interpolation at the spatial scale of the PAN images.

The results of the application of the proposed method for the fusion of the Deimos-2 datasets using different decomposition levels of the ATWT are shown in Tables 4.1 and 4.2. In Table 4.1, the injection gains of the MS image of equation (4.9) and the ratio average energy of equation (4.4) are calculated. Table 4.2 shows the 4-bands correlation of the MS image with the resulting image.

Test Images	Level	C_{NIR}	C_R	C_G	C_B	$\sum C_i$	RE
Image 1	1	0.2582	0.2085	0.2109	0.2173	0.8949	0.7623
	2	**0.2640**	**0.2128**	**0.2156**	**0.2224**	**0.9147**	0.7811
	3	0.2616	0.2088	0.2116	0.2189	0.9009	0.7730
Image 2	1	0.3969	0.1070	0.1352	0.1358	0.7750	0.7299
	2	**0.4084**	**0.1090**	**0.1380**	**0.1381**	**0.7935**	0.7505
	3	0.4059	0.1041	0.1324	0.1321	0.7745	1.0062
Image 3	1	0.2497	0.2011	0.2025	0.2077	0.8610	0.8700
	2	**0.2552**	**0.2071**	**0.2090**	**0.2148**	**0.8861**	0.8969
	3	0.2483	0.2040	0.2065	0.2132	0.8721	0.8859

Table 4.1. Weighting coefficients of the 4-bands MS image, their sum and ratio average energy for different decomposition levels.

Test Images	Correlation / Level	$Corr_{NIR}$	$Corr_R$	$Corr_G$	$Corr_B$
Image 1	1	**0.9968**	**0.9948**	**0.9930**	**0.9935**
	2	0.9869	0.9790	0.9717	0.9737
	3	0.9801	0.9677	0.9569	0.9595
Image 2	1	**0.9981**	**0.9900**	**0.9875**	**0.9890**
	2	0.9921	0.9598	0.9502	0.9561
	3	0.9881	0.9422	0.9291	0.9375
Image 3	1	**0.9870**	**0.9868**	**0.9849**	**0.9840**
	2	0.9534	0.9534	0.9468	0.9434
	3	0.9162	0.9169	0.9060	0.8992

Table 4.2. 4-bands correlation between MS and fused images.

Figures 4.5, 4.6 and 4.7 present the application of the proposed approach of the Deimos-2 datasets using one, two and three decomposition levels of the ATWT.

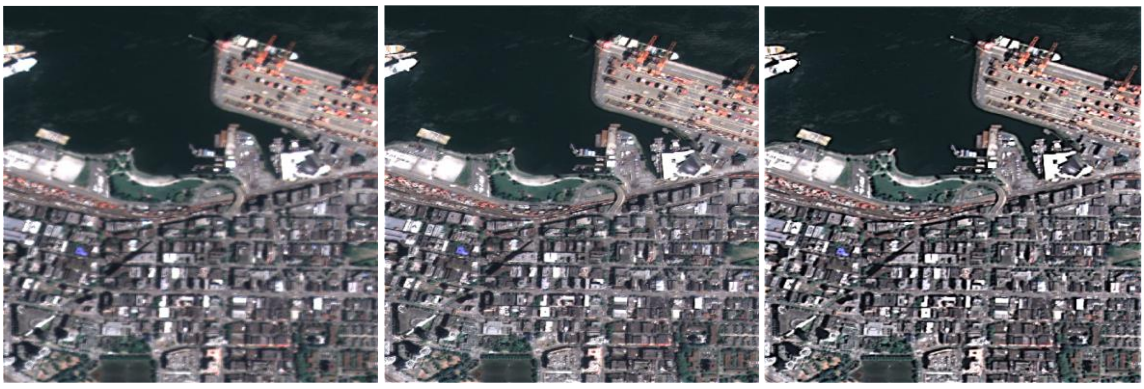

(a) One Level. (b) Two levels. (c) Three levels.

Figure 4.5. Fused images by applying the proposed approach (image 1).
(a) ~(c) Pansharpened images by using 1 ~3 decomposition levels of the ATWT, respectively.

(a) One Level. (b) Two levels. (c) Three levels.

Figure 4.6. Fused images by applying the proposed approach (image 2).
(a) ~(c) Pansharpened images by using 1 ~3 decomposition levels of the ATWT, respectively.

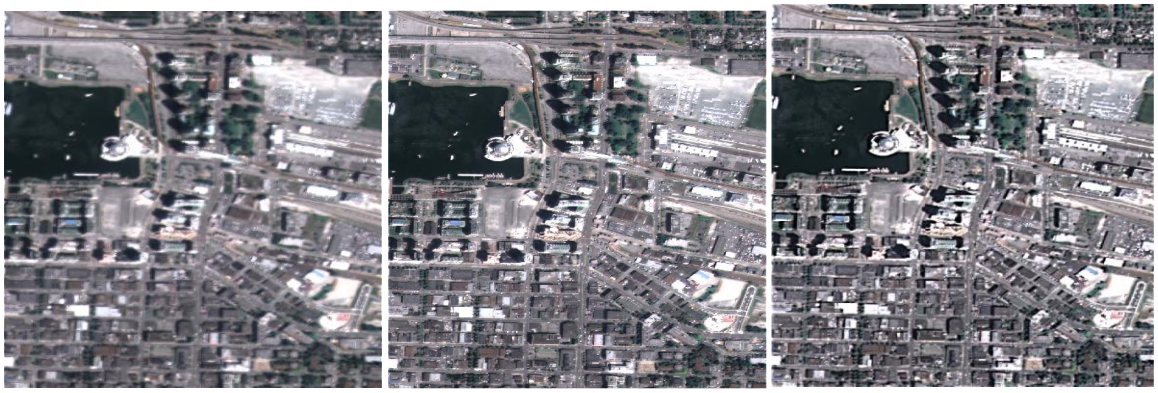

(a) One Level. (b) Two levels. (c) Three levels.

Figure 4.7. Fused images by applying the proposed approach (image 3).
(a) ~(c) Pansharpened images by using 1 ~3 decomposition levels of the ATWT, respectively.

4.3.2. Discussions

Visual analysis of Figures 4.5, 4.6 and 4.7 shows an apparent improvement in spatial quality in the merged images. In these figures, the colors of the resulting images are comparable to those of the input MS images with an obvious increase in spatial resolution. It is clear from these figures that the spatial resolution of pansharpened images increases with increasing level of ATWT decomposition.

Quantitative analysis in Table 4.1 shows the values of the energy ratio between the MS and the LPAN images, as well as the values of the weighting coefficients used for the calculation of the adapted intensity component (I_{adp}) for three levels of decomposition of the ATWT. By correspondence of the equation (4.3), one notices that for the entire test images, the level 2 gave a sum which approaches the unit.

Table 4.2 shows the correlation values between the four spectral bands of the MS and merged images, for three levels of ATWT decomposition. We notice that as we increase the level of decomposition, the values decrease. So the results for one level are the best although visually the most degraded for all the test images. Level two gives good values by comparison with level three. These values are logical because the comparison is made with the up-sampled MS image and not with a reference image.

Two additional data sets acquired by the WorldView-2 and WorldView-3 satellites were also used to evaluate and test the performance of the proposed algorithm, as shown in Table 4.3 [4]. The datasets used in this experiment cover different areas with different sizes. The image of Stockholm (Sweden) was acquired on August 27, 2016 and the images of Rio de Janeiro (Brazil) were acquired on February 5, 2016 and the images of Sidney were acquired in 2009 [4].

In Table 4.3, the quality assessment is evaluated by the different metrics described in Chapter 2 with different decomposition levels and for nine images.

Test Images	Metrics	CC	ERGAS	RASE	RMSE	SAM	SID	SCC	UIQI	SSIM
	Ref. values	0	0	0	0	0	0	1	1	1
Image 1 of Fig. 4.2 (Deimos-2)	Level 1	**0.0023**	**1.8992**	**7.5223**	**8.6684**	**0.4352**	0.0235	0.9183	**0.9945**	**0.9973**
	Level 2	0.0093	3.8857	15.3905	17.7354	0.8187	**0.0157**	0.9839	0.9776	0.9766
	Level 3	0.0160	4.8702	19.2901	22.2291	1.0469	0.0439	**0.9885**	0.9653	0.9463
Image 2 of Fig. 4.3 (Deimos-2)	Level 1	**0.0046**	**2.6052**	**8.5294**	**9.2596**	**0.7905**	**0.0014**	0.9026	**0.9911**	**0.9948**
	Level 2	0.0189	5.3979	17.6745	19.1879	1.6613	0.0256	0.9715	0.9634	0.9562
	Level 3	0.0304	6.6751	21.8602	23.7319	2.1598	0.0395	**0.9769**	0.9461	0.9106
Image 3 of Fig. 4.4 (Deimos-2)	Level 1	**0.0044**	**1.4907**	**5.8887**	**9.2864**	**0.2987**	**0.0003**	0.9207	**0.9930**	**0.9973**
	Level 2	0.0171	2.9556	11.6761	18.4129	0.6417	0.0008	0.9826	0.9733	0.9760
	Level 3	0.0276	3.6077	14.2527	22.4762	0.8434	0.0026	**0.9863**	0.9609	0.9454
Image 4 (WV-2) (500x500) Stokholm – Sweden	Level 1	0.0071	**2.5536**	**8.3703**	**25.7584**	**0.8324**	0.0200	0.9250	**0.9833**	**0.9245**
	Level 2	**0.0053**	3.5505	11.6365	35.8096	1.1753	0.0157	**0.9575**	0.9648	0.8313
	Level 3	**0.0053**	3.5079	11.4968	35.3797	1.1612	0.0134	0.9476	0.9685	0.8327
Image 5 (WV-2) (500x500) Sidney – Australia	Level 1	**0.0018**	**2.1529**	**8.0656**	**21.8824**	**0.4568**	**0.0041**	0.9375	**0.9898**	**0.9508**
	Level 2	0.0054	3.9863	14.9339	40.5162	0.8932	0.0186	0.9884	0.9664	0.8538
	Level 3	0.0061	4.3689	16.3681	44.4072	1.0179	0.0174	**0.9896**	0.9602	0.8313
Image 6 (WV-2) (500x600) Sidney – Australia	Level 1	**0.0016**	**1.8149**	**6.9347**	**22.0814**	**0.4149**	**0.0021**	0.9332	**0.9933**	**0.9554**
	Level 2	0.0056	3.4203	13.0687	41.6133	0.8199	0.0035	0.9865	0.9769	0.8619
	Level 3	0.0075	3.8395	14.6721	46.7190	0.9502	0.0025	**0.9883**	0.9713	0.8366
mage 7 (WV-3) (768x672) Rio de Janeiro - Brazil	Level 1	**0.0044**	**2.0289**	**6.4988**	**20.9553**	**0.7955**	0.0127	0.9230	**0.9879**	**0.9345**
	Level 2	0.0069	3.1368	10.0482	32.4004	1.2561	0.0287	**0.9634**	0.9715	0.7869
	Level 3	0.0067	3.4104	10.9260	35.2308	1.3950	**0.0121**	0.9604	0.9662	0.7032
Image 8 (WV-3) (500x500) Rio de Janeiro - Brazil	Level 1	**0.0020**	**2.4753**	**8.1312**	**25.1762**	**0.9220**	0.0296	0.9373	**0.9915**	**0.8098**
	Level 2	0.0034	3.8586	12.6760	39.2481	1.4338	0.0488	0.9730	0.9795	0.6378
	Level 3	0.0042	4.4325	14.5632	45.0912	1.6683	**0.0267**	**0.9735**	0.9730	0.5546
Image 9 (WV-3) (512x512) Rio de Janeiro - Brazil	Level 1	0.0094	**2.3997**	**7.7146**	**25.8465**	**0.8057**	0.0388	0.9312	**0.9831**	**0.8803**
	Level 2	0.0145	3.4223	11.0018	36.8599	1.1107	0.0306	**0.9622**	0.9662	0.7655
	Level 3	**0.0064**	3.4726	11.1636	37.4019	1.1250	**0.0121**	0.9560	0.9649	0.7459

Table 4.3. Spectral quality assessment, with reference image, of different decomposition levels of the proposed method for different datasets.

Test Images	Metrics	d_λ	d_s	QNR
	Ref. values	0	0	1
Image 1 of Fig. 4.2 (Deimos-2)	Level 1	**0.0496**	**0.0342**	**0.9178**
	Level 2	0.0812	0.0589	0.8646
	Level 3	0.0974	0.1003	0.8120
Image 2 of Fig. 4.3 (Deimos-2)	Level 1	0.0369	**0.0157**	**0.9480**
	Level 2	**0.0158**	0.0843	0.9012
	Level 3	0.0599	0.0583	0.8852
Image 3 of Fig. 4.4 (Deimos-2)	Level 1	**0.0158**	0.0843	0.9012
	Level 2	0.0450	**0.0107**	**0.9447**
	Level 3	0.0634	0.0518	0.8881
Image 4 (WV-2) (500x500) Stokholm – Sweden	Level 1	0.0081	0.0402	**0.9520**
	Level 2	0.0143	**0.0378**	0.9485
	Level 3	**0.0062**	0.0420	**0.9520**
Image 5 (WV-2) (500x500) Sidney – Australia	Level 1	**0.0062**	0.0580	0.9362
	Level 2	0.0204	**0.0372**	**0.9431**
	Level 3	0.0192	0.0394	0.9422
Image 6 (WV-2) (500x600) Sidney – Australia	Level 1	**0.0030**	0.0381	0.9590
	Level 2	0.0100	0.0148	0.9753
	Level 3	0.0133	**0.0099**	**0.9769**
mage 7 (WV-3) (768x672) Rio de Janeiro - Brazil	Level 1	**0.0410**	**0.0446**	**0.9163**
	Level 2	0.0624	0.0787	0.8637
	Level 3	0.0553	0.0721	0.8765
Image 8 (WV-3) (500x500) Rio de Janeiro - Brazil	Level 1	**0.0273**	**0.0324**	**0.9412**
	Level 2	0.0430	0.0656	0.8942
	Level 3	0.0384	0.0591	0.9048
Image 9 (WV-3) (512x512) Rio de Janeiro - Brazil	Level 1	**0.0538**	**0.0380**	**0.9102**
	Level 2	0.0683	0.0677	0.8687
	Level 3	0.0616	0.0626	0.8797

Table 4.4. Spectral quality assessment, without reference image, of different decomposition levels of the proposed method for different datasets.

From Tables 4.3 and 4.4, it is clear that the merged images resulting from the application of the proposed approach with a single level of decomposition show almost the highest spectral quality, although they are visually degraded.

The results of the quantitative assessment are based on the metrics from Chapter 2, as shown in Tables 4.3 and 4.4, show better fusion quality from which we can conclude that the proposed approach offers more spatial information and reasonable spectral quality for high levels of decomposition (2 and 3 levels). In the case of the application of ATWT with three levels of decomposition, the merged images show the best quality of spatial resolution and this is also confirmed by the values obtained from SCC as shown in Table 4.3. For one level of decomposition, the proposed method retains more spectral information, while retaining

good spatial quality. In addition, it can be clearly seen that when the ATWT decomposition level is two, the fusion results reach the optimum quality, hence a good compromise between spatial and spectral quality.

The influence of the E_L error image, from equation (4.12), on the spectral and spatial qualities of the combined images is obvious and this is due to the presence of the high resolution details in E_L which vary depending on the image error.

4.3.3. Comparison with some state-of-the-art fusion methods

In this section, the performance evaluation of the suggested pansharpening approach is compared with various state-of-the-art fusion methods. Several methods have been used for comparison with the proposed approach such as Generalized IHS (GIHS) [32], PCA-based image fusion [29], Improved Adaptive IHS (IAIHS) [40], the Proportional AWL (AWLP) [67], the Partial Replacement Adaptive Component Substitution (PRACS) [45] and the fusion of MS and PAN images preserving spectral quality by Optimal Filter (OF) [119]. Each method is subject to a compromise between the quality of the spectral and spatial resolutions.

The experimental results obtained after the application of different pansharpening methods of three Deimos-2 images (image 1, image 2 and image 3) are presented in Figures 4.8, 4.9 and 4.10. Tables 4.5 and 4.6 illustrate the performance of our pansharpening algorithm compared to the previous methods. We applied 2 levels of decomposition for the multiresolution methods.

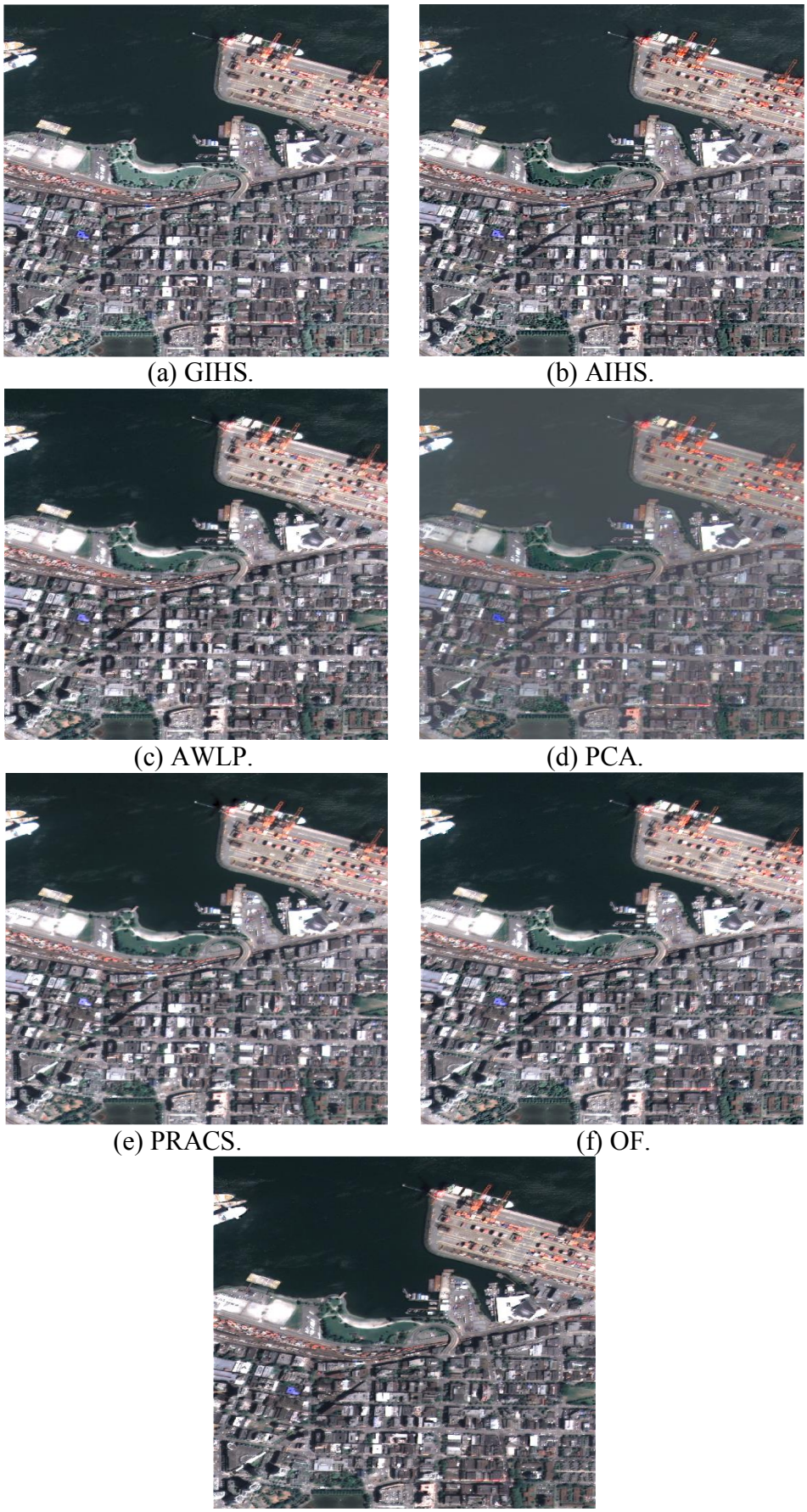

(a) GIHS. (b) AIHS.

(c) AWLP. (d) PCA.

(e) PRACS. (f) OF.

(g) Proposed method.

Figure 4.8. Fusion results of the first Deimos-2 image for different methods.

(a) GIHS.

(b) AIHS.

(c) AWLP.

(d) PCA.

(e) PRACS.

(f) OF.

(g) Proposed method.

Figure 4.9. Fusion results of the second Deimos-2 image for different methods.

(a) GIHS.

(b) AIHS.

(c) AWLP.

(d) PCA.

(e) PRACS.

(f) OF.

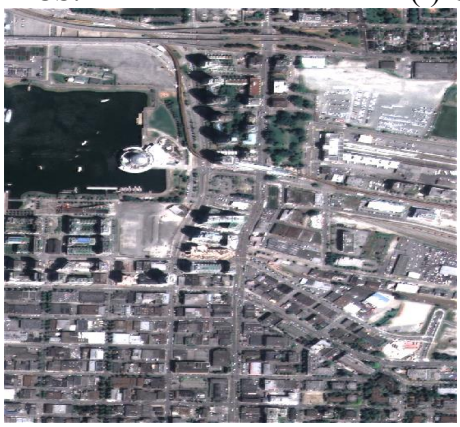

(g) Proposed method.

Figure 4.10. Fusion results of the third Deimos-2 image for different methods.

For better visualization of fusion results, we have zoomed in the same part of each image. Figures 4.11, 4.12 and 4.13 represent this zoom.

(a) GIHS. (b) AIHS. (c) AWLP.

(d) PCA. (e) PRACS. (f) OF.

(g) Proposed method.

Figure 4.11. Zoom of fusion results of the first Deimos-2 image for different methods.

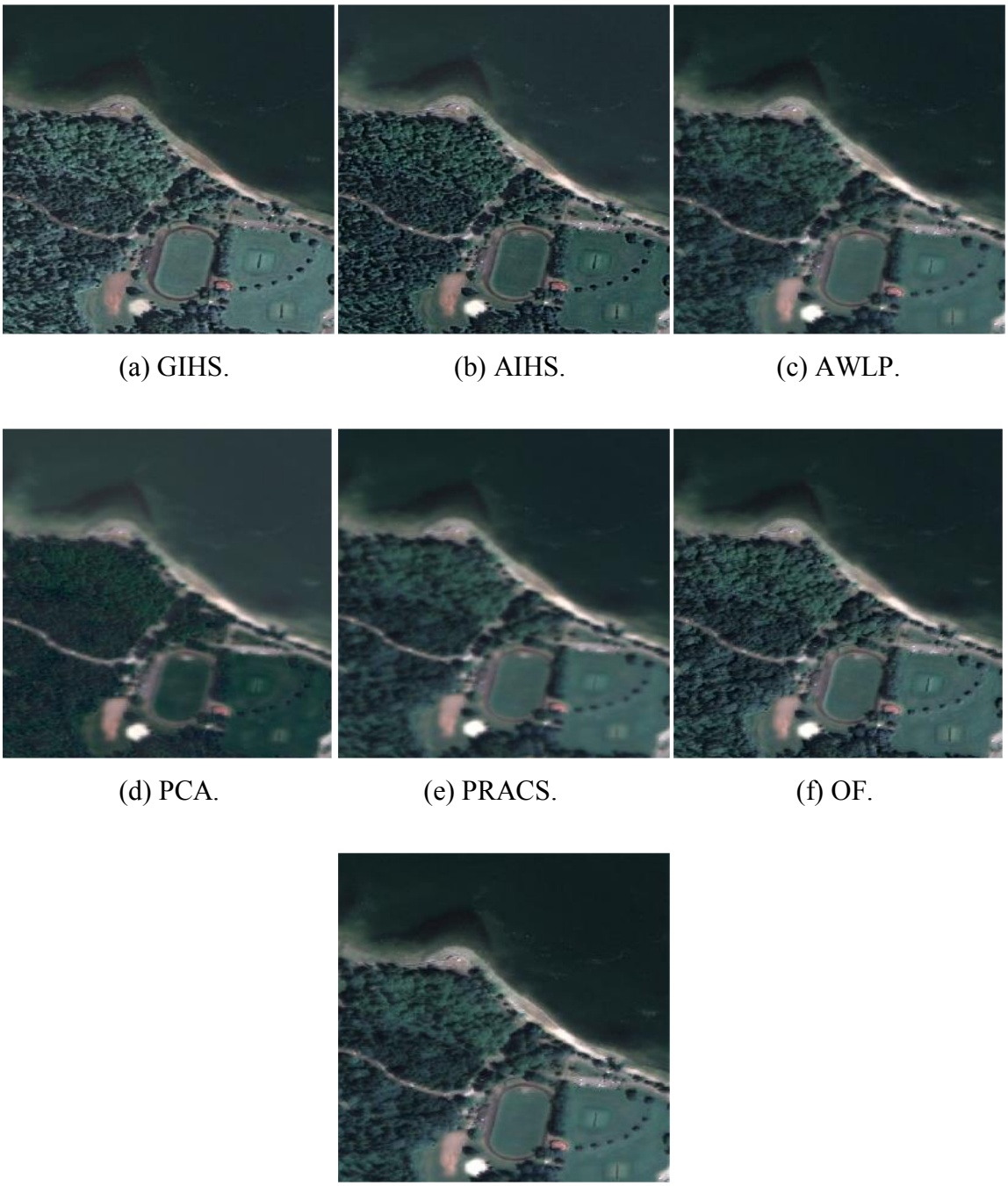

(a) GIHS. (b) AIHS. (c) AWLP.

(d) PCA. (e) PRACS. (f) OF.

(g) Proposed method.

Figure 4.12. Zoom of fusion results of the second Deimos-2 image for different methods.

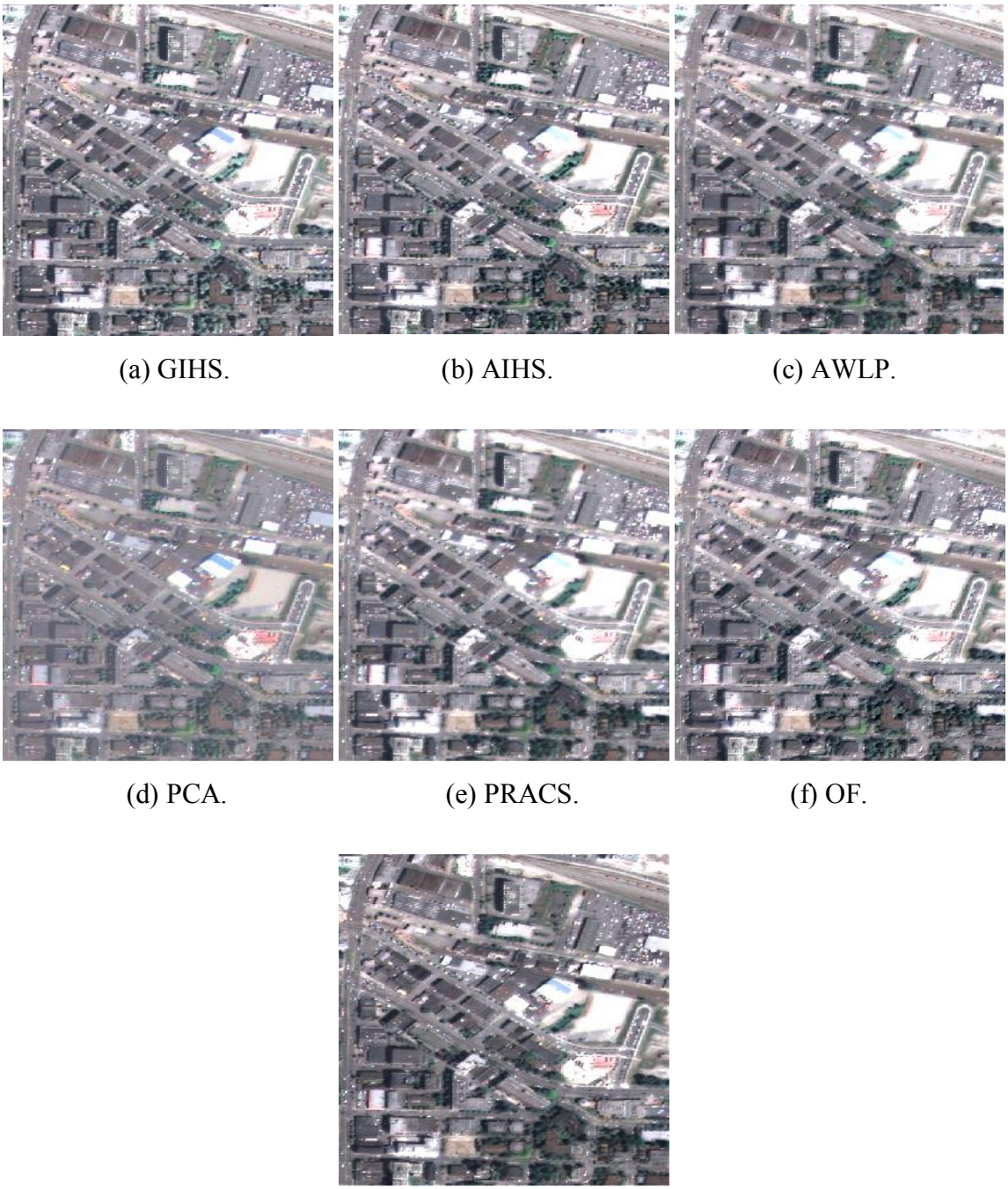

(a) GIHS. (b) AIHS. (c) AWLP.

(d) PCA. (e) PRACS. (f) OF.

(g) Proposed method.

Figure 4.13. Zoom of fusion results of the third Deimos-2 image for different methods.

Test Images	Metrics / Methods	CC	ERGAS	RASE	RMSE	SAM	SID	SCC	UIQI	SSIM
		0	0	0	0	0	0	1	1	1
Deimos-2 images	GIHS	0.0285	5.6985	22.5444	30.1408	1.7161	0.0311	**0.9916**	0.9280	0.8886
	AIHS	**0.0043**	5.7104	22.4819	29.7967	2.1875	0.0443	0.9903	0.9315	0.8961
	AWLP	0.0213	4.3249	17.4812	23.4077	**2.3309E-7**	**0.0013**	0.9509	0.9627	0.9581
	PCA	0.2683	7.7880	31.1688	41.2881	4.0265	0.0515	0.9471	0.8141	0.8007
	PRACS	0.0204	4.2847	17.4401	23.1224	1.2166	0.0677	0.9688	0.9643	0.9483
	OF	0.0317	4.7057	18.9366	25.3195	1.1819	0.0620	0.8451	0.9560	0.9428
	Proposed	0.0132	**3.4207**	**13.5333**	**18.0741**	0.7302	0.0082	0.9832	**0.9755**	**0.9763**
WV-2 images	GIHS	0.0089	4.5698	17.2795	50.7240	1.4450	0.0076	**0.9910**	0.9555	0.8103
	AIHS	**0.0010**	4.3303	16.7635	49.1225	1.2774	0.0133	0.9896	0.9635	0.8301
	AWLP	0.0086	4.5449	18.2989	53.7066	**2.4291 E-7**	**0.0004**	0.9481	0.9579	0.8338
	PCA	0.1783	8.6275	32.9548	97.1180	4.6856	0.0329	0.9168	0.7952	0.7236
	PRACS	0.0056	4.4537	18.1805	53.2766	1.0780	0.0032	0.9820	0.9638	0.8391
	OF	0.0119	5.5075	21.1254	61.9830	1.4337	0.0692	0.8298	0.9495	0.7992
	Proposed	0.0055	**3.7033**	**14.0013**	**41.0648**	0.8565	0.0110	0.9874	**0.9717**	**0.8579**
WV-3 images	GIHS	0.0406	5.7943	18.8313	60.6717	2.2267	0.0512	0.9818	0.9309	0.5300
	AIHS	0.0111	6.0724	19.7170	63.4380	2.0189	0.0478	**0.9849**	0.9246	0.5421
	AWLP	0.0514	4.4063	17.0148	54.9083	**0.0306**	0.0721	0.9373	0.9534	0.7377
	PCA	0.3438	7.4928	26.6934	85.4653	3.4903	0.0487	0.9416	0.8712	0.4411
	PRACS	0.0171	3.7532	12.8878	41.4724	1.3918	**0.0016**	0.9293	0.9721	**0.7387**
	OF	0.0151	5.1888	15.1875	48.9939	2.3728	0.1263	0.8228	0.9531	0.6688
	Proposed	**0.0089**	**3.6405**	**11.8389**	**38.0540**	1.2723	0.0397	0.9676	**0.9728**	0.7017

Table 4.5. Quality metrics with no reference data for different pansharpening methods using different satellite images (mean values).

Test Images	Metrics / Methods	d_λ	d_s	QNR
		0	0	1
Deimos-2 images	GIHS	0.0873	0.0941	0.8269
	AIHS	0.0668	0.0571	0.8800
	AWLP	0.0665	0.0423	0.8940
	PCA	0.0539	0.1921	0.7644
	PRACS	0.0548	0.0358	0.9113
	OF	0.0730	**0.0069**	0.9206
	Proposed	**0.0450**	0.0107	**0.9447**
WV-2 images	GIHS	0.0283	0.0644	0.9092
	AIHS	0.0201	0.0426	0.9382
	AWLP	0.0614	0.0660	0.8766
	PCA	0.1792	0.2754	0.5948
	PRACS	0.0192	0.0490	0.9327
	OF	0.0379	**0.0270**	0.9361
	Proposed	**0.0190**	0.0375	**0.9442**
WV-3 images	GIHS	0.0894	**0.0608**	0.8552
	AIHS	0.1035	0.1328	0.7774
	AWLP	0.0970	0.0979	0.8146
	PCA	0.1662	0.2714	0.6075
	PRACS	**0.0453**	0.0792	**0.8791**
	OF	0.0884	0.0743	0.8439
	Proposed	0.0683	0.0677	0.8687

Table 4.6. Quality metrics with reference data for different pansharpening methods using different satellite images (mean values).

4.3.4. Discussions

For a qualitative assessment, all of these methods are good. Spatial quality is improved compared to MS images and the edges are more representative. Obviously, the results obtained depend on the specific input image, but images fused by applying the PCA method have a clear spectral distortion especially on the regions containing green vegetation. After applying the proposed fusion scheme, the spectral and spatial qualities of the pansharpened images obtained are close to the spectral quality of the original MS image and the spatial quality of the original PAN image, respectively. The results of the visual comparison agree with the quality assessment presented in Tables 4.5 and 4.6. In Table 4.5, the SCC values are closer to the optimal values when using IHS-based methods. The adaptive IHS image method (IAIHS) works better than the original IHS.

The majority of the used methods have good spatial detail. However, they visually show a small spectral distortion especially the AWLP, PCA, PRACS and OF methods. The resulting image of our proposed algorithm gives the best visual and quantitative quality.

It should be noted that due to the lack of reference images in real experiments, the quantitative evaluation was carried out exhaustively in two aspects. First, the dimension of the merged image was changed to spatial dimension of the MS image, and the MS image was taken as a reference image. Second, the fusion results were assessed on the basis of unreferenced quality assessment indices [120]. Since there is no reference image here, the QNR index is used to assess spectral and spatial distortions between the merged image and the original PAN image and the MS image, as shown in the Table 4.6.

It is clear from Tables 4.5 and 4.6 that the proposed algorithm surpasses the other techniques in terms of spatial quality and in most of spectral quality indices. It should be noted that the proposed scheme gives the best results for the following quality indices: ERGAS, RASE, RSME UIQI, SSIM and QNR. The main advantage of the proposed scheme is the adaptive gain injection, in which spatial details are inserted into each upsampled MS band while retaining its spectral information.

The computation time of an algorithm is an important comparative element. The following table represents the execution time of the methods studied in this chapter and for the same image.

We can see the difference in time between the different methods. A direct method requires less time than a method that uses multiple resolutions or more complicated.

Test Image	Methods	Calculation time in seconds
Image 1 of Fig. 4.2 (Deimos-2) PAN : 1312 x 864 pixels MS : 328 x 216 pixels	GIHS	**0.2358**
	AIHS	1.3374
	AWLP	0.3945
	PCA	0.4880
	PRACS	3.4999
	OF	30.4684
	Proposed	0.7337

Table 4.7. Calculation time for different methods.

Some information about the computer that performed these calculations:

- Processor: Intel(R) Core(TM) i5 CPU M 460 @ 2.53GHz, 2534 MHz, 2 core(s), 4 logical processor(s).
- Physical memory (RAM) installed 4.00 GB.
- x64-based PC type.
- 64-bit operating system.

4.4. Conclusion

In this chapter, a new combination between multi-resolution analysis (MRA-based method) and component substitution method (CS-based method) is proposed to design a new pansharpening scheme. The proposed pansharpening algorithm is based on the IHS injection model, in which the spatial details are first selected and extracted from the PAN image, then injected into the MS bands by applying the ATWT transform. In addition, weighting coefficients are introduced to improve the spatial details of the resulting image while preserving its spectral information. The weighting coefficients of the intensity component (I) are calculated using the average energy ratio and the correlation coefficients between the MS bands and the wavelet decomposed version of the PAN image. The detail information is then injected into the high spectral resolution MS bands to obtain a merged image with high spatial information.

Experimental results and performance evaluation measures demonstrated the ability of the proposed fusion algorithm to increase the spatial resolution of the resulting fused images while preserving their spectral information.

GENERAL CONCLUSION

Image fusion has multiple applications, and choosing to synthesize MS spectral bands with high spatial resolution creates constraints that are not always understood by the community. Developers of new fusion methods need to take more account of the local dissimilarities between the MS image to be fused and the high spatial resolution PAN image that contains the structures to be injected. We generally note an absence of physical considerations in establishing and evaluating methods.

It was essential to consider quality assessment before developing new fusion methods. However, some efforts had attempted to provide a framework for the evaluation with success. We have provided an algorithm capable of being used regardless of the ratio, the spatial resolution, the type of landscape considered and the number of spectral bands.

After giving an introduction representing the notion of pansharpening and the objective of this work with the constraints that can be encountered in practice and literature during the fusion process, we have first of all, studied the already published methods by identifying their advantages and disadvantages (Chapter 1). Three categories of fusion methods were considered. We have presented and studied some of the most used and popular methods of each category. Then, a fitness check was presented in Chapter 2 to make a comparative study between the different fusion methods considered in the first chapter in order to be able to extract the qualitative and quantitative properties. In the third chapter, recent methods of each category have been studied and presented in order to make a comparative qualitative and quantitative study. In the fourth chapter, we have contributed to the enhancement of the well-known AWLP method by improving its quality, visually and quantitatively, by proposing a new scheme for injection gains, using the IHS transform, which takes into account the energy ratio between the MS and PAN images, transformed by ATWT, and which is based on the contours contained in the satellite images. This algorithm has been validated for Deimos-2, World view-2 and World view-3 satellite imagery. The results obtained with this method agree with the qualitative and quantitative analyzes obtained by fusion methods of which we knew a priori their impact on the edges. The proposed scheme can inject more spatial information and provide better color preservation. The new proposed fusion method has the advantage of not reproducing the artifacts identified for the previous methods. It also shows very good results for quantitative quality analysis.

The important conclusion is that the improvement of the AWLP fusion method corresponds to a compromise between visual and parametric constraints. Hybrid methods make it possible to take advantage of the better properties obtained for each method.

We have therefore satisfied our objective, namely to offer a more efficient method.

It is necessary to clearly define the framework of fusion applications in which the developer places himself in order to understand all the constraints. Next, the fusion methods should be evaluated by applying quality evaluation parameters.

For visual evaluation, fused products in color or grayscale should be compared to their references. In addition, the conclusions of the visual evaluation depend on the areas of work of the developers, and are not necessarily generalizable to other applications. With regard to quantitative analysis, care should be taken to use parameters that cover different aspects of the quality of the fusion products.

We wish in the near future to adapt and apply the proposed approach for the fusion of multimodal medical images and to further improve our algorithm by using the adaptive IHS transform (IAIHS) instead of the classical IHS transform.

REFERENCES

[1]: A. Goshtasby, S. Nikolov, “Image fusion: advances in the state of the art,” Information Fusion 8 (2), pp. 114-118, (2007).

[2]: Y. Liu, S. Liu and Z. Wang, “A general framework for image fusion based on multi-scale transform and sparse representation,” Information Fusion, Elsevier, (2014). http://dx.doi.org/10.1016/j.inffus.2014.09.004.

[3]: F. Muller and s. de Béthune, “La fusion d'images,” Bulletin de la Société Géographique de Liège, 38, pp. 79-94, (2000).

[4]: S.M.A. Wady, Y. Bentoutou, A. Bengermikh, N. Bounoua and N. Taleb, “A New IHS and Wavelet based Pansharpening Algorithm for High Spatial Resolution Satellite Imagery,” Advances in Space Research, Elsevier, Vol. 66, Issue7, pp. 1507-1521, (2020).

[5]: C. Thomas, T. Ranchin, L. Wald, and J. Chanussot, “Synthesis of multispectral images to high spatial resolution: A critical review of fusion methods based on remote sensing physics,” IEEE Transactions on Geoscience and Remote Sensing, Vol. 46, No. 5, pp. 1301-1312, (2008).

[6]: G. Vivone, L. Alparone, J. Chanussot, M. Dalla Mura, A. Garzelli, G.A. Licciardi, R. Restaino and L. Wald, “A critical comparison among pansharpening algorithms,” IEEE Transactions on Geoscience and Remote Sensing, Vol. 53, pp.2565-2586, (2015).

[7]: L. Loncan, L.B. de Almeida, J.M. Bioucas-Dias, X. Briottet, J. Chanussot, N. Dobigeon, S. Fabre, W. Liao, G.A. Licciardi and M. Simoes, “Hyperspectral pansharpening: A review,” IEEE Transactions on Geoscience and Remote Sensing, Vol. 3, No. 3, pp. 27-46, (2015).

[8]: M. Cetin and N. Musaoglu, “Merging hyperspectral and panchromatic image data: Qualitative and quantitative analysis,” Int. J. Remote Sensing, Vol. 30, No. 7, pp. 1779-1804, (2009).

[9]: N. Yokoya, T. Yairi, and A. Iwasaki, “Coupled nonnegative matrix factorization unmixing for hyperspectral and multispectral data fusion,” IEEE Transactions on Geoscience and Remote Sensing, Vol. 50, No. 2, pp. 528-537, (2012).

[10]: H. Shen, X. Meng and L. Zhang, “An Integrated Framework for the Spatio-Temporal-Spectral Fusion of Remote Sensing Images,” IEEE Transactions on Geoscience and Remote Sensing, Vol. 54, No. 12, pp. 7135-7148, (December 2016).

[11]: M. Moeller, T. Wittman and A. L. Bertozzi, “Variational Wavelet Pan-Sharpening,” IEEE Transactions on Geoscience and Remote Sensing, Submitted (December 2008).

[12]: K. P. Upla, S. Joshi, M. V. Joshi and P.P. Gajjar, “Multiresolution image fusion using edge-preserving filters,” Journal of Applied Remote Sensing, Vol. 9, (2015).

[13]: J. Inglada, V. Muron, D. Pichard, and T. Feuvrier, “Analysis of artifacts in subpixel remote sensing image registration,” IEEE Transactions on Geoscience and Remote Sensing, Vol. 45, No. 1, pp. 254-264, (2007).

[14]: P. Blanc, L. Wald, and T. Ranchin, “Importance and effect of coregistration quality in an example of ‘pixel to pixel’ fusion process,” in Proc. 2nd Conf. Fusion Earth Data: Merging Point Meas., Raster Maps Remotely Sensed Images, Nice, France: SEE/URISCA, Jan. 28-30, pp. 67-73, (1998).

[15]: J. Zhou, D. L. Civco, and J. A. Silvander, “A wavelet transform method to merge Landsat TM and SPOT panchromatic data,” Int. J. Remote Sens., Vol. 19, No. 4, pp. 743-757, (1998).

[16]: Y. Zhang, “A new merging method and its spectral and spatial effects,” Int. J. Remote Sens., Vol. 20, No. 10, pp. 2003-2014, (1999).

[17]: C. Thomas, “Fusion d'images de résolutions spatiales différentes,” doctorat thesis, l’Ecole des Mines de Paris, (December 2006).

[18]: P.S. Chavez, S.C. Sides and J.A. Anderson, “Comparison of three different methods to merge multiresolution and multispectral data: Landsat TM and SPOT panchromatic,” Photogramm. Eng. Remote Sens. Vol. 57, pp. 295-303, (1991).

[19]: L. Alparone, B. Aiazzi, S. Baronti and A. Garzelli, “Remote Sensing Image Fusion,” Crc Press, Boca Raton, FL, USA, (2015).

[20]: J. Vrabel, “Multispectral imagery band sharpening study,” Photogramm. Eng. Remote Sens., Vol. 62, pp. 1075-1084, (1996).

[21]: S. Baronti, B. Aiazzi, M. Selva, A. Garzelli and L. Alparone, “A theoretical analysis of the effects of aliasing and misregistration on pansharpened imagery,” IEEE J. Selected Topics Signal Process., Vol. 5, pp. 446-453, (2011).

[22]: S. Li and B. Yang, “A new pan-sharpening method using a compressed sensing technique,” IEEE Transactions on Geoscience and Remote Sensing, Vol. 49, pp. 738-746, (2011).

[23]: H. Zhang and B. Huang, “A new look at image fusion methods from a bayesian perspective,” Remote Sens. Vol. 7, pp. 6828-6861, (2015).

[24]: C. Kwan, J.H. Choi, S. Chan, J. Zhou and B. Budavari, “Resolution enhancement for hyperspectral images: a super-resolution and fusion approach,” Proceedings of the IEEE International Conference on Acoustics, Speech and Signal Processing, New Orleans, USA, pp. 6180-6184, (2017).

[25]: J. Zhou, C. Kwan and B. Budavari, “Hyperspectral image super-resolution: a hybrid color mapping approach,” J. Appl. Remote Sens. Vol. 10, pp. 035024:1-035024:20, (2016).

[26]: A. Garzelli, “A Review of Image Fusion Algorithms Based on the super-resolution paradigm,” Remote Sens. Vol. 8, pp. 797:1-797:20, (2016).

[27]: M. Xiangchaoa, S. Huanfengb, L. Huifangb, Z. Liangpeic and F. Randia, “Review of the pansharpening methods for remote sensing images based on the idea of meta-analysis:

Practical discussion and challenges," Information Fusion, Elsevier, Vol. 46, pp. 102-113, (2019). https://doi.org/10.1016/j.inffus.2018.05.006

[28]: W. Carper, T. Lillesand and R. Kiefer, "The use of Intensity-Hue-Saturation transformations for merging spot panchromatic and multispectral image data," Photogramm. Eng. Remote Sens. Vol. 56, pp. 459-467, (1990).

[29]: P.S. Chavez Jr and A.Y. Kwarteng, "Extracting spectral contrast in Landsat Thematic Mapper image data using selective principal component analysis," Photogramm. Eng. Remote Sens. Vol. 55, pp. 339-348, (1989).

[30]: V.K. Shettigara, "A generalized component substitution technique for spatial enhancement of multispectral images using a higher resolution data set," Photogramm. Eng. Remote Sens. Vol. 58, pp. 561-567, (1992).

[31]: C.A. Laben and B.V. Brower, "Process for enhancing the spatial resolution of multispectral imagery using pan-sharpening," Eastman Kodak Company, Rochester, N.Y., United States, (2000).

[32]: T.M. Tu, S.C. Su, H.C. Shyu and P.S. Huang, "A new look at IHS-like image fusion methods," Inform. Fusion, Vol. 2, pp. 177-186, (2001).

[33]: Z. Wang, D. Ziou, C. Armenakis, D. Li and Q. Li, "A comparative analysis of image fusion methods," IEEE Tran. Geosci. Remote Sens. Vol. 43, pp. 1391-1402, (2005).

[34]: W. Dou, Y. Chen, X. Li and D.Z. Sui, "A general framework for component substitution image fusion: an implementation using the fast image fusion method," Comput. Geosci. Vol. 33, pp. 219-228, (2007).

[35]: B. Aiazzi, S. Baronti and M. Selva, "Improving component substitution pansharpening through multivariate regression of MS +Pan Data," IEEE Tran. Geosci. Remote Sens. Vol. 45, pp. 3230-3239, (2007).

[36]: A. Garzelli, F. Nencini and L. Capobianco, "Optimal MMSE pansharpening of very high resolution multispectral images," IEEE Tran. Geosci. Remote Sens. Vol. 46, No. 1, pp. 228-236, (2008).

[37]: T.M. Tu, C.L. Hsu, P.Y. Tu and C.H. Lee, "An adjustable pan-sharpening approach for IKONOS/QuickBird/GeoEye-1/WorldView-2 imagery," IEEE Journal of Selected Topics in Applied Earth Observations and Remote Sensing, Vol. 5, No. 1, pp. 125-134, (2012).

[38]: A.R. Gillespie, A.B. Kahle and R.E. Walker, "Color enhancement of highly correlated images-channel ratio and 'chromaticity' transformation techniques," Remote Sens. Environ. Vol. 22, pp. 343-365, (1987).

[39]: T.M. Tu, P.S. Huang, C.L. Hung and C.P. Chang, "A fast intensity-hue-saturation fusion technique with spectral adjustment for IKONOS imagery," IEEE Geosci. Remote Sens. Lett. Vol. 1, pp. 309-312, (2004).

[40]: S. Rahmani, M. Strait, D. Merkurjev, M. Moeller and T. Wittman, "An adaptive IHS pansharpening method," IEEE Geosci. Remote Sens. Lett. Vol. 7, pp. 746-750, (2010).

[41]: Y. Zhang, "System and Method for Image Fusion", University of New Brunswick, United States, Patent 20040141659, (2004).

[42]: Q. Xu, B. Li, Y. Zhang and L. Ding, "High-fidelity component substitution pansharpening by the fitting of substitution data," IEEE Tran. Geosci. Remote Sens. Vol. 52, pp. 7380-7392, (2014).

[43]: H.R. Shahdoosti and N. Javaheri, "Pansharpening of clustered MS and pan images considering mixed pixels," IEEE Geosci. Remote Sens. Lett. Vol. 14, pp. 826-830, (2017).

[44]: B. Aiazzi, L. Alparone, S. Baronti, A. Garzelli and M. Selva, "Twenty-five years of pansharpening: A critical review and new developments," in: C.-H. Chen (Ed.), Signal and Image Processing for Remote Sensing, 2nd Edition, CRC Press, pp. 533-548, (2012).

[45]: J. Choi, K. Yu and Y. Kim, "A new adaptive component-substitution-based satellite image fusion by using partial replacement," IEEE Tran. Geosci. Remote Sens. Vol. 49, pp. 295-309, (2011).

[46]: C. Pohl and J.L. Van Genderen, "Multisensor image fusion in remote sensing: concepts, methods and applications," (review article), International Journal of Remote Sensing, Vol. 19, No.5, pp. 823-854, (1998).

[47]: Y. X. Hui and J. L. Cheng, "Fusion algorithm for remote sensing images based on nonsubsampled contourlet transform," ACTA Automatica Sinica, Vol. 34, No. 3, pp. 274-281, (2008).

[48]: F. A. Al-Wassai1, N.V. Kalyankar and A. Al-Zuky, "The IHS transformations based image fusion," Computer Vision and Pattern Recognition (cs.CV), (2011).
http://arxiv.org/abs/1107.3348

[49]: R. Haydn, G.W. Dalke, J. Henkel and J.E. Bare, "Application of the IHS color transform to the processing of multisensor data and image enhancement," Proceedings of International Symposium Remote Sensing of Arid and Semi-Arid Lands, Cairo, Egypt, pp. 599-616, (1982).

[50]: M. Ehlers, "Multisensor image fusion techniques in remote sensing," ISPRS Journal of Photogrammetry and Remote Sensing, No. 46, pp. 19-30, (1991).

[51]: Zhang, "Understanding image fusion," PCI Geomatics, (2008).

[52]: M. Choi, "A new intensity-hue-saturation fusion approach to image fusion with a tradeoff parameter," IEEE Transactions of Geoscience and Remote Sensing, Vol. 44, pp. 1672-1682, (2006).

[53]: M. Choi, H. Kim, N.I. Cho and H.O. Kim, "An improved intensity-hue-saturation method for IKONOS image fusion," International Journal of Remote Sensing, (2008).

[54]: R. Schowengerdt, “Remote sensing: models and methods for image processing,” 3rd ed., Academic Press, Elsevier, NY, (2007).

[55]: M. Chikr El-Mezouar, “Fusion d'images en télédétection satellitaire,” Doctorat thesis, INSA (Rennes, France) and l’université de Djillali Liabes (Sidi Bel-Abbes, Algeria), (2012).

[56]: T. Tu, Y. Lee, Ch. Chang and P. Huang, “Adjustable intensity-hue-saturation and Brovey transform fusion technique for IKONOS/Quickbird imagery,” In: Optical Engineering, (2005).

[57]: S. Dehnavi and A. Mohammadzadeh, “A new developed GIHS-BT-SFIM fusion method based on edge and class data,” International Archives of the Photogrammetry, Remote Sensing and Spatial Information Sciences, Vol. XL-1/W3, SMPR 2013, pp. 5-8, Tehran, Iran, (2013).

[58]: I. Amro, J. Mateos, M. Vega, R.Molina and A. K. Katsaggelos, “A survey of classical methods and new trends in pansharpening of multispectral images,” EURASIP J. Adv. Signal Process., No. 1, pp. 79:1-79:22, (2011).

[59]: Y. Yang, W. Wan, S. Huang, F. Yuan, S. Yang and Y. Que, “Remote sensing image fusion based on adaptive IHS and multiscale guided filter,” IEEE access, Received July 15, 2016, accepted August 4, 2016, date of publication August 10, 2016, date of current version September 16, (2016).

[60]: R.A. Schowengerdt, “Reconstruction of multispatial, multispectral image data using spatial frequency content,” Photogramm. Eng. Remote Sens., Vol. 46, pp. 1325-1334, (1980).

[61]: H. Li, B.S. Manjunath and S.K. Mitra, “Multisensor image fusion using the wavelet transform,” Graphical Models Image Process., Vol. 57, pp. 235-245, (1995).

[62]: B. Aiazzi, S. Baronti, F. Lotti, M. Selva, “A Comparison between global and context adaptive pansharpening of multispectral images,” IEEE Geosci. Remote Sens. Lett., Vol. 6, pp. 302-306, (2009).

[63]: B.G. Duport, J. Girel, J.M. Chassery and G. Pautou, “The use of multiresolution analysis and wavelets transform for merging SPOT panchromatic and multispectral image data,” Photogramm. Eng. Remote Sens., Vol. 62, pp. 1057-1066, (1996).

[64]: J. Zhou, D.L. Civco, J.A. Silander, “A wavelet transform method to merge Landsat TM and SPOT panchromatic data,” Int. J. Remote Sens., Vol. 19, pp. 743-757, (1998).

[65]: A. Garzelli and F. Nencini, “Panchromatic sharpening of remote sensing images using a multiscale Kalman filter,” Pattern Recognit., Vol. 40, pp. 3568-3577, (2007).

[66]: G.P. Nason and B.W. Silverman, “The stationary wavelet transform and some statistical applications,” Wavelets and Statistics, Springer, NY, USA, pp. 281-299, (1995).

[67]: X. Otazu, M.G. Audicana, O. Fors and J. Nunez, “Introduction of sensor spectral response into image fusion methods. Application to wavelet-based methods,” IEEE Tran. Geosci. Remote Sens., Vol. 43, pp. 2376-2385, (2005).

[68]: B. Aiazzi, L. Alparone, S. Baronti, A. Garzelli, "Context-driven fusion of high spatial and spectral resolution data based on oversampled multiresolution analysis," IEEE Tran. Geosci. Remote Sens., Vol. 40, pp. 2300-2312, (2002).

[69]: G. Vivone, R. Restaino, M. Dalla Mura, G. Licciardi and J. Chanussot," Contrast and error-based fusion schemes for multispectral image pansharpening," IEEE Geosci. Remote Sens. Lett., Vol. 11, pp. 930-934, (2014).

[70]: L. Alparone, S. Baronti, B. Aiazzi and A. Garzelli, "Spatial methods for multispectral pansharpening: Multiresolution analysis demystified," IEEE Tran. Geosci. Remote Sens., Vol. 54, pp. 2563-2576, (2016).

[71]: L. Alparone, B. Aiazzi, S. Baronti and A. Garzelli, "Sharpening of very high resolution images with spectral distortion minimization," Proceedings of the IEEE International Geoscience and Remote Sensing Symposium, IEEE, Toulouse, France, pp. 458-460, (2003).

[72]: B. Aiazzi, L. Alparone, S. Baronti, A. Garzelli and M. Selva, "MTF-tailored multiscale fusion of high-resolution MS and PAN imagery," Photogramm. Eng. Remote Sens., Vol. 72, pp. 591-596, (2006).

[73]: I. Amro and J. Mateos, "Multispectral image pansharpening based on the contourlet transform," Inform. Opt. Photon., Vol. 206, pp. 247-261, (2010).

[74]: V.P. Shah, N.H. Younan and R. King, "Pan-sharpening via the contourlet transform," Proceedings of the IEEE International Geoscience and Remote Sensing Symposium, IEEE, Barcelona, pp. 310-313, (2007).

[75]: M. Choi, R.Y. Kim, M.R. Nam and H.O. Kim, "Fusion of multispectral and panchromatic satellite images using the curvelet transform," IEEE Geosci. Remote Sens. Lett., Vol. 2, pp. 136-140, (2005).

[76]: J. Liu, "Smoothing filter-based intensity modulation: A spectral preserve image fusion technique for improving spatial details," Int. J. Remote Sens., Vol. 21, pp. 3461-3472, (2000).

[77]: A. Garzelli and F. Nencini, "Interband structure modeling for Pan-sharpening of very high-resolution multispectral images," Inform. Fusion, Vol. 6, pp. 213-224, (2005).

[78]: V.P.S. Naidu and J.R. Raol, "Pixel-level Image Fusion using Wavelets and Principal Component Analysis," Defence Science Journal, Vol. 58, No. 3, pp. 338-352, (2008).

[79]: G. Pajares and J.M. de la Cruz. "A wavelet-based image fusion tutorial," Pattern Recognition, Vol. 37, pp.1855-872, (2004).

[80]: M.J. Moghaddam, "Real-time multi-focus image fusion using discrete wavelet transform and Laplacian pyramid transform," Chalmess University of Technology, Goteborg, Sweden. Masters thesis, (2005).

[81]: I. Daubechies, "Ten lectures on wavelets," In Regular Conference Series in Applied Maths, Vol. 91, SIAM, Philadelphia, (1992).

[82]: J. Nunez, X. Otazu, O. Fors, A. Prades, V. Pala and R. Arbio, "Multiresolution based image fusion with additive wavelet decomposition," IEEE Trans. on Geosciences and Remote Sensing, Vol.37, No.3, pp. 1204-1211, (1999).

[83]: N.H. Kaplan and I. Erer, "Bilateral pyramid based pansharpening of multispectral satellite images," IEEE, IGARSS, pp. 2376-2379, (2012).

[84]: P. Burt and E. Adelson, "The Laplacian pyramid as a compact image code," IEEE Trans. Commun., Vol. 31, No. 4, pp. 532-540, (1983).

[85]: P. Pradham, N.H. Younan and R.L. king, "Image fusion: Algorithms and applications," Academic Press, pp. 393-428, (2008).

[86]: J. Zeng, A. Sayedelahl, T. Gilmore, P. Frazier and M. Cho, "Assessing image fusion methods for unconstrained outdoor scenes," The US Army Robotics CTA Program., (2006).

[87]: M.G. Audicana, J.L Saleta, R.G Catalan and R. Garcia, "Fusion of multispectral and panchromatic images using improved IHS and PCA mergers based on wavelet decomposition," Geoscience and Remote Sensing, IEEE Transactions, Vol. 42, No. 6, pp. 1291-1299, (2004).

[88]: T. Ranchin and L. Wald, "Fusion of high spatial and spectral resolution images: The ARSIS concept and its implementation," Photogramm. Eng. Remote Sens. Vol. 66, (2000).

[89]: C. Ballester, V. Caselles, L. Igual, J. Verdera and B. Rougé, "A variational model for P+XS image fusion," Int. J. Comput. Vis., Vol. 69, pp. 43-58, (2006).

[90]: F. Fang, F. Li, C. Shen and G. Zhang, "A variational approach for pan-sharpening," IEEE Trans. Image Process., Vol. 22, pp. 2822-2834, (2013).

[91]: D. Fasbender, J. Radoux and P. Bogaert, "Bayesian data fusion for adaptable image pansharpening," IEEE Tran. Geosci. Remote Sens., Vol. 46, pp. 1847-1857, (2008).

[92]: P. Liu, L. Xiao, J. Zhang and B. Naz, "Spatial-Hessian-Feature-Guided variational model for pan-sharpening," IEEE Tran. Geosci. Remote Sens., Vol. 54, pp. 2235-2253, (2016).

[93]: N.D.A. Mascarenhas, G.J.F. Banon and A.L. Candeias, "Multispectral image data fusion under a Bayesian approach," Int. J. Remote Sens., Vol. 17, pp. 1457-1471, (1996).

[94]: F. Palsson, J.R. Sveinsson and M.O. Ulfarsson, "A New Pansharpening algorithm based on total variation," IEEE Geosci. Remote Sens. Lett., Vol. 11, pp. 318-322, (2014).

[95]: L. Zhang, H. Shen, W. Gong and H. Zhang, "Adjustable model-based fusion method for multispectral and panchromatic images," IEEE Trans. Syst. Man Cybern. Part B: Cybern, Vol. 42, pp. 1693-1704, (2012).

[96]: M. Guo, H. Zhang, J. Li, L. Zhang and H. Shen, "An online coupled dictionary learning approach for remote sensing image fusion," IEEE Journal of Selected Topics in Applied Earth Observations and Remote Sensing, Vol. 7, pp. 1284-1294, (2014).

[97]: C. Jiang, H. Zhang, H. Shen and L. Zhang, "A practical compressed sensing-based pansharpening method," IEEE Geosci. Remote Sens. Lett., Vol. 9, pp. 629-633, (2012).

[98]: X.X. Zhu and R. Bamler, "A sparse image fusion algorithm with application to pansharpening," IEEE Tran. Geosci. Remote Sens. Vol. 51, pp. 2827-2836, (2013).

[99]: X. Meng, H. Shen, L. Zhang, Q. Yuan and H. Li, "A unified framework for spatio-temporal-spectral fusion of remote sensing images," Proceedings of the IEEE International Geoscience and Remote Sensing Symposium, Milan, Italy, (2015).

[100]: Z. Li and H. Leung, "Fusion of multispectral and panchromatic images using a restoration-based method," IEEE Tran. Geosci. Remote Sens., Vol. 47, pp. 1482-1491, (2009).

[101]: Q. Wei, "Bayesian fusion of multi-band images: a powerful tool for super-resolution," Institut national polytechnique de Toulouse (INPT), (2015).

[102]: M. Vega, J. Mateos, R. Molina and A.K. Katsaggelos, "Super resolution of multispectral images using ℓ1 Image models and interband correlations," J. Signal Process. Systems, Vol. 65, pp. 509-523, (2011).

[103]: C. Chen, Y. Li, W. Liu and J. Huang, "Image fusion with local spectral consistency and dynamic gradient sparsity," Proceedings of the IEEE Conference on Computer Vision and Pattern Recognition (CVPR), Columbus, OH, USA, pp. 2760-2765, (2014).

[104]: M. Moeller, T. Wittman, A.L. Bertozzi and M. Burger, "A variational approach for sharpening high dimensional images," SIAM J. Imaging Sci., Vol. 5, pp. 150-178, (2012).

[105]: X. Meng, H. Shen, Q. Yuan, H. Li and L. Zhang, "An integrated fusion framework for joint information reconstruction and resolution enhancement," Proceedings of the ISPRS-International Archives of the Photogrammetry. Remote Sensing and Spatial Information Sciences, Wuhan, China, pp. 831-835, (2017).

[106]: M. Joshi and A. Jalobeanu, "MAP estimation for multiresolution fusion in remotely sensed images using an IGMRF prior model," IEEE Trans. Geosci. Remote Sens. Vol. 48, pp. 1245-1255, (2010).

[107]: R. Molina, M. Vega, J. Mateos and A.K. Katsaggelos, "Variational posterior distribution approximation in Bayesian super resolution reconstruction of multispectral images," Appl. Comput. Harmonic Anal., Vol. 24, pp. 251-267, (2008).

[108]: J. Duran, A. Buades, B. Coll and C. Sbert, "A nonlocal variational model for pansharpening image fusion," SIAM J. Imaging Sci., Vol. 7, pp. 761-796, (2014).

[109]: P. Liu, L. Xiao and T. Li, "A variational pan-sharpening method based on spatial fractional-order geometry and spectral-spatial low-rank priors," IEEE Trans. Geosci. Remote Sens., Vol. 56, pp. 1788-1802, (2018).

[110]: H. Shen, X. Li, Q. Cheng, C. Zeng, G. Yang, H. Li and L. Zhang, "Missing information reconstruction of remote sensing data: A technical review," IEEE Geosci. Remote

Sens. Mag., Vol. 3, pp. 61-85, (2015).

[111]: X.X. Zhu, C. Grohnfeldt and R. Bamler, "Exploiting joint sparsity for pansharpening: the J-Sparse FI algorithm," IEEE Trans. Geosci. Remote Sens., Vol. 54, pp. 2664-2681, (2016).

[112]: H. Shen, L. Zhang, B. Huang and P. Li, "A MAP approach for joint motion estimation, segmentation, and super resolution," IEEE Trans. Image Process., Vol. 16, pp. 479-490, (2007).

[113]: H. Shen, "Integrated fusion method for multiple temporal-spatial-spectral Images," Proceedings of the XXII Congress of International Society for Photogrammetry and Remote Sensing (ISPRS), Melbourne, Australia, pp. 2, (2012).

[114]: Q. Wei, N. Dobigeon and J.Y. Tourneret, "Fast fusion of multi-band images based on solving a Sylvester equation," IEEE Trans. Image Process., Vol. 24, pp. 4109-4121, (2015).

[115]: Z.M. Zhou, P.L. Yang, Y.X. Li, W. Yin and L. Jiang, "Joint IHS and variational methods for pan-sharpening of very high resolution imagery," IEEE, IGARSS, pp. 2597-2600, (2013).

[116]: M. Moeller, T. Wittman and A.L. Bertozzi, "A variational approach to hyperspectral image fusion," Proc. SPIE Conference on Algorithms and Technologies for Multispectral, Hyperspectral, and Ultraspectral Imagery XV, Orlando, Florida, (2009).

[117]: M.M. Khan, J. Chanussot, L. Condat and A. Montavert, "Indusion: Fusion of multispectral and panchromatic images using the induction scaling technique," IEEE Geosci. Remote Sens. Lett., Vol. 5, No. 1, pp. 98-102, (2008).

[118]: X. Meng, Y. Xiong, F. Shao, H. Shen, W. Sun, G. Yang, Q. Yuan, R. Fu and H. Zhang, "A large-scale benchmark data set for performance evaluation of pansharpening," IEEE Trans. Geosci. Rem. Sens., (2020).

[119]: H.R. Shahdoosti and H. Ghassemian, "Fusion of MS and PAN images preserving spectral quality," IEEE, Geoscience and Remote Sensing Letters.
http://ieeexplore.ieee.org/xpl/articleDetails.jsp?tp=&arnumber=6895274&queryText%3D.QT.preserving+spectral+quality.QT.

[120]: X. Meng, Q. Yuan and L. Zhang, "Pansharpening for cloud-contaminated very high-resolution remote sensing images," IEEE Trans. on Geosci. Remote Sens., Vol. 57, No. 5, pp. 2840-2854, (2018).

[121]: F. Pálsson, J. R. Sveinsson, J. A. Benediktsson and H. Aanæs, "Classification of pansharpened urban satellite images," IEEE Journal of Selected Topics in Applied Earth Observations and Remote Sensing, Vol. 5, No. 1, pp. 281- 297, (2012).

[122]: Q. Du, O. Gungor and J. Shan, "Performance evaluation for pan-sharpening techniques," Department of Electrical and Computer Engineering, Mississippi State University, No. 24, (2008).

[123]: A. Bovik and Z. Wang, "A universal image quality index," IEEE Signal Processing Letters, Vol. 9, No. 3, pp. 81-84, (2002).

[124]: L. Alparone, B. Aiazzi, S. Baronti, A. Garzelli and P. Nencini, "A global quality measurement of pan-sharpened multispectral imagery," IEEE Geosci. Remote Sens. Lett., Vol. 1, No. 4, pp. 313-317, (2004).

[125]: A. Goetz, W. Boardman and R. Yunas, "Discrimination among semi-arid landscape endmembers using the spectral angle mapper (SAM) algorithm," Proc. Summeries 3rd Annu. JPL Airborne Geosci. Workshop, pp. 147-149, (1992).

[126]: L. Wald, "Quality of high resolution synthesized images: is there a simple criterion?," Proc. Int. Conf. Fusion Earth Data, (2000).

[127]: C. Chang, "Spectral information divergence for hyperspectral image analysis," Proc. Geosci. Remote Sens. Symp., Vol. 1, pp. 509-511, (1999).

[128]: L. Alparone, B. Aiazzi, S. Baronti, A. Garzelli, F. Nencini and M. Selva, "Multispectral and panchromatic data fusion assessment without reference," Photogramm. Eng. Remote Sens., Vol. 74, No. 2, pp. 193-200, (2008).

[129]: Z. Zhou, S. Peng, B. Wang, Z. Hao and S. Chen, "An optimized approach for pansharpening very high resolution multispectral images," IEEE Geoscience and Remote Sensing Letters, Vol. 9, No. 4, pp. 735-739, (2012).

[130]: W. Huang, L. Xiao, Z. Wei, H. Liu, and S.Tang, "A new pan-sharpening method with deep neural networks," IEEE Geoscience and Remote Sensing Letters, Vol. 12, No. 5, pp. 1037- 1041, (2015).

[131]: L. Wald, "Some terms of reference in data fusion," IEEE Trans. Geosci. Remote Sens., Vol. 37, No. 3, pp. 1190-1193, (1999).

[132]: G. Piella, "A general framework for multiresolution image fusion: From pixels to regions," Inf. Fusion, Vol. 4, No. 4, pp. 259-280, (December 2003).

[133]: V. Tsagaris, V. Anastassopoulos and G.A. Lampropoulos, "Fusion of hyperspectral data using segmented PCT for color representation and classification," IEEE Transactions on Geoscience and Remote Sensing, Vol. 43, No. 10, pp. 2365-2375, (2005).

[134]: P.S. Huang and T. Te-Ming, "Target fusion-based approach for classifying high spatial resolution imagery," In Workshops "Advances in Techniques for Analysis of Remotely Sensed Data", 27-28 Oct., pp. 175-181, (2003).

[135]: J. Byeungwoo and D.A. Landgrebe, "Decision fusion approach for multitemporal classification," IEEE transactions on Geoscience and Remote Sensing, Digital Object Identifier 10.1109/36.763278, Vol. 37, No. 3, pp.1227-1233, (1999).

[136]: I. Couloignier, T. Ranchin, V.P. Valtonen and L. Wald, "Benefit of the future SPOT5 and of data fusion to urban mapping," International Journal of Remote Sensing, Vol. 19, No. 8, pp. 1519-1532 , (1998).

[137]: Q. Zhang and J. Wang, "Detection of buildings from Landsat-7 ETM+ and SPOT panchromatic data in Beijing, China," Proceedings of Geoscience and Remote Sensing Symposium, IGARSS'02, IEEE International, Digital Object Identifier 10.1109/IGARSS.2002.1026841, Vol. 5, pp. 2977-2979, (2002).

[138]: S.K. Sengupta, A.S. Lopez and D.N. Poland," Class-label statistics: a basis for fusing information from multispectral imagery with an application to unsupervised detection of human settlement," Proceedings of Geoscience and Remote Sensing Symposium, IGARSS'04, IEEE International, Digital Object Identifier 10.1109/IGARSS.2004.1368600, Vol. 2, pp. 1084-1087, (2004).

[139]: E. Ricchetti, "Application of optical high resolution satellite imagery for archaeological prospection over Hierapolis (Turkey)," Proceedings of Geoscience and Remote Sensing Symposium, IGARSS'04, IEEE International, Digital Object Identifier 10.1109/IGARSS.2004.1369976, Vol. 6, pp.3898-3901, (2004).

[140]: S.P. Constantinos, M.S. Pattichis and E. Micheli-Tzanakou, "Medical imaging fusion applications : an overview," Record of the Thirty-fifth conference on Signals, Systems and Computers, Pacific Grove, Californie, Vol. 2, pp. 1263-1267, (2001).

[141]: Y. Cornet, M. Binard and J.P. Donnay, "Intérêt de la fusion d'images à haute résolution spatiale pour la classification de l'occupation du sol en milieu urbain, " International Journal of Geomatics: Satellite imagery, European Journal of GID and Spatial Analysis, Lavoisier (Eds.), pp.417-439, (2004).

[142]: R. Redondo, F. Sroubek, S. Fisher and G. Cristobal, "Multifocus fusion with multisize windows," Applications of Digital Image Processing XXVIII, Andrew G. and Tescher (Eds.), Proc. SPIE, Vol. 5909, pp. 410-418, (2005).

[143]: H. Chen and P.K. Varshney, "A human perception inspired quality metric for image fusion based on regional information," Information Fusion, Digital Object Identifier 10.1016/j.inffus.2005.10.001, Elsevier (Eds.), (2005).

[144]: Y. Zheng, E.A. Essock, B.C. Hansen and E.M. Haun, "A new metric based on extended spatial frequency and its application to DWT based fusion algorithms," Information Fusion, Digital Object Identifier 10.1016/j.inffus.2005.04.003, Elsevier (Eds.), (2005).

[145]: C. Profanter, R. Prommegger, M. Gabriel, R. Moncayo, G. J. Wetscher, T. Lang and R. Bale, "Computed axial tomography-MIBI image fusion for preoperative localization in primary hyperparathyroidism," The American Journal of Surgery, Vol. 187, No. 3, pp. 383-387, (2004).